December 2020

Nozzle Clogging Prevention and Analysis in Cold Spray

Alden Foelsche

NOZZLE CLOGGING PREVENTION AND ANALYSIS IN COLD SPRAY

A Thesis Presented

by

ALDEN F. FOELSCHE

Submitted to the Graduate School of the
University of Massachusetts Amherst in partial fulfillment
of the requirements for the degree of

MASTER OF SCIENCE IN MECHANICAL ENGINEERING

September 2020

Mechanical and Industrial Engineering

NOZZLE CLOGGING PREVENTION AND ANALYSIS IN COLD SPRAY

A Thesis Presented

by

ALDEN F. FOELSCHE

Approved as to style and content by:

David P. Schmidt, Chair

Jonathan P. Rothstein, Member

Wen Chen, Member

Sundar Krishnamurty, Department Chair
Mechanical and Industrial Engineering

"I count all things to be loss in view of the surpassing value of knowing Christ Jesus my Lord"

- Philipians 3:8

ACKNOWLEDGMENTS

I am grateful to my parents for their love and support both during this thesis process and for my entire 25-year life. Their helpfulness and guidance is an immeasurable blessing to me. I am likewise thankful for the care and loving support of my uncle, whom I look up to in the same way I do my parents. I am also grateful for my Omi, who passed away my freshman year of college. She had a profound impact on and investment in my life. I would have liked for her to see me reach this point and see the man I've become. The nurture and encouragement of my parents, uncle, and Omi have been wind in my sails to get me where I am today, both academically and personally.

I have been so encouraged and helped by many dear friends throughout this process. They have picked me up and spurred me on through discouraging moments in research and many (too many...) late nights. From delivering free grab-and-go meals to my lab (several times per week!) to ironing my suit on defense day, I have been blessed in countless ways on countless occasions by wonderful friends.

My labmates (who are also my friends, but deserve their own acknowledgment) have been an instrumental part of this thesis, as well. I have so appreciated the selflessness of my coworkers in their willingness to drop their busy schedules to help me. Especially during my early months in the lab, this was incredibly helpful. Although we are not slow to distract each other and chat for hours, this ultimately makes for a more fun experience, even if it means staying up late or missing a deadline (sorry Professor...). Our lab is an enjoyable place to work because of the great people there. As an added plus, this lab is the only group of people I have ever met who appreciate

olive and pineapple on the *same* pizza. It can be hard enough to find people who like either of those toppings! These are rare, quality people.

A great thanks is due to my advisor, Professor Schmidt, for his investment in me these past two years. Not only has he been practically helpful with his experience in and knowledge of the field, he has also been a joy to work for. He is understanding, personally invested in my work, and has my best interest in mind. Because of his attitude, the lab is a place where serious work gets done while genuine fun is had. His stories are also some of the best, even if he tells them a fourth or fifth time without realizing (we never tell him). I am glad he sustained his hope in me even after I "appalled" him (his words) in my first lab meeting where I presented a negative value of heat transfer coefficient (we all start somewhere).

I am additionally thankful for the investment of my other two committee members, Professors Chen and Rothstein. Their enthusiasm for this project has been motivating and encouraging, and their input on this manuscript has served to greatly sharpen my arguments. They, along with Professor Schmidt, have been very patient with me during this process. I have genuinely believed that I would graduate now five times, and somehow it has yet to happen until now. Between adding content last-minute, breaking my hand, tearing my ACL, and tearing my meniscus, they have endured many anticlimactic setbacks (though I believe the injuries hurt me more than them).

Finally and ultimately, I am grateful to Jesus Christ for dying on the cross, taking the punishment upon Himself that I deserve for my sins, and in exchange giving me eternal life with Him by no work of my own. This fact is the central aspect of my life, and although I do not always act that way because I have faults, He died in the first place to forgive me for those. Jesus' death for my sake inspires me to live my life for Him as a grateful response. I am not perfect, and neither is this thesis, but I have sought to do quality hard work on this thesis for Jesus' sake.

I acknowledge the financial support of the NCMS under contract number 202028-141054.

ABSTRACT

NOZZLE CLOGGING PREVENTION AND ANALYSIS IN COLD SPRAY

SEPTEMBER 2020

ALDEN F. FOELSCHE

B.S., UNIVERSITY OF MASSACHUSETTS, AMHERST

M.S.M.E, UNIVERSITY OF MASSACHUSETTS AMHERST

Directed by: Professor David P. Schmidt

Cold spray is an additive manufacturing method in which powder particles are accelerated through a supersonic nozzle and impinged upon a nearby substrate, provided they reach their so-called critical velocity. True to its name, the cold spray process employs lower particle temperatures than other thermal spray processes while the particle velocities are comparably high. Because bonding occurs mostly in the solid state and at high speeds, cold spray deposits are distinguished for having low porosity and low residual stresses which nearly match those of the bulk material.

One complication with the cold spray process is the tendency for nozzles to clog when spraying (in general) low-melting-point or dense metal powders. Clogging occurs when particles collide with the inner nozzle wall and bond to it rather than bouncing off and continuing downstream towards the substrate. The particles accumulate and eventually plug the nozzle passage. Clogging is inconvenient because it interrupts the spraying process, making it impossible to complete a task. Furthermore, when particle buildup occurs inside the nozzle, the working cross-sectional

area decreases, which decreases the flow velocity and therefore the particle velocity, ultimately jeopardizing the particles' ability to reach critical velocity at the substrate.

In this work, computational fluid dynamics (CFD) is used to study various aspects of nozzle clogging. Nozzle cooling with supercritical CO_2 as the refrigerant is investigated as a means to prevent clogging. The effects of nozzle cooling on both the driving gas and the particles are addressed. Simplified pressure oscillations at the nozzle inlet are imposed to determine whether such oscillations, if present, can cause clogging. Subsequently, more realistic and complicated flow oscillations are introduced to isolate a potential root cause of clogging. Finally, several novel nozzle internal geometries are evaluated for their effectiveness at preventing clogging. A recommendation is provided for a nozzle to be tested experimentally because it might completely prevent clogging.

TABLE OF CONTENTS

LIST OF TABLES

LIST OF FIGURES

Figure **Page**

INTRODUCTION

Cold gas dynamic spraying (cold spray) is a metal deposition process with multiple industrial applications. It belongs to a wider family of thermal spray processes which use high-temperature gases to apply coatings to parts. The main difference between cold spray and other thermal spray processes is that cold spray takes place at relatively low temperatures and much higher particle velocities [15]. Because the particle bonding occurs mostly in the solid state, the material crystal structure is maintained, resulting in a deposit with low porosity [10] and low residual stresses [123] similar to the bulk material. Other thermal sprays largely rely on the rapid solidification of molten particles for bonding and therefore do not have the same advantages in terms of porosity and tensile properties. Cold spray deposits are hard, dense, and homogenous. The process is also multipurpose in that it can enhance mechanical properties [127], allow the joining of two dissimilar metals [14], repair damaged parts [55], and additively manufacture parts [145]. It can also offer a more sustainable solution compared to other methods both in terms of its environmental impact and its ability to refurbish expensive parts [136]. Because of these attributes, there is much interest in further developing cold spray for industry and manufacturing.

In the cold spray process, gas is accelerated (typically helium or nitrogen [88], but sometimes air [52]) through a converging-diverging de Laval nozzle which carries solid atomized powder. The powder material is often metal, as is the case in this study, though polymers [45], ceramics [1], and composites [150] can be deposited with cold spray as well. During the expansion of gas in the nozzle, particles are accelerated to high speed and are impinged upon a nearby substrate. Particles will bond to the substrate if they reach a certain critical velocity [115], and the bonded particles

accumulate to produce a deposit on the substrate. The whole process is illustrated in Figure 1, while an axisymmetric diagram of nozzle zone names is provided in Figure 2.

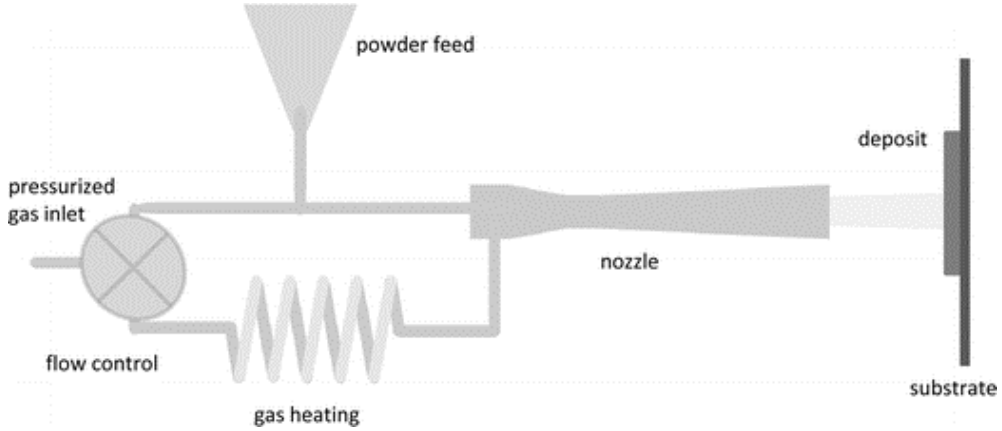

Figure 1: Overview of the Cold Spray Deposition Process [16]

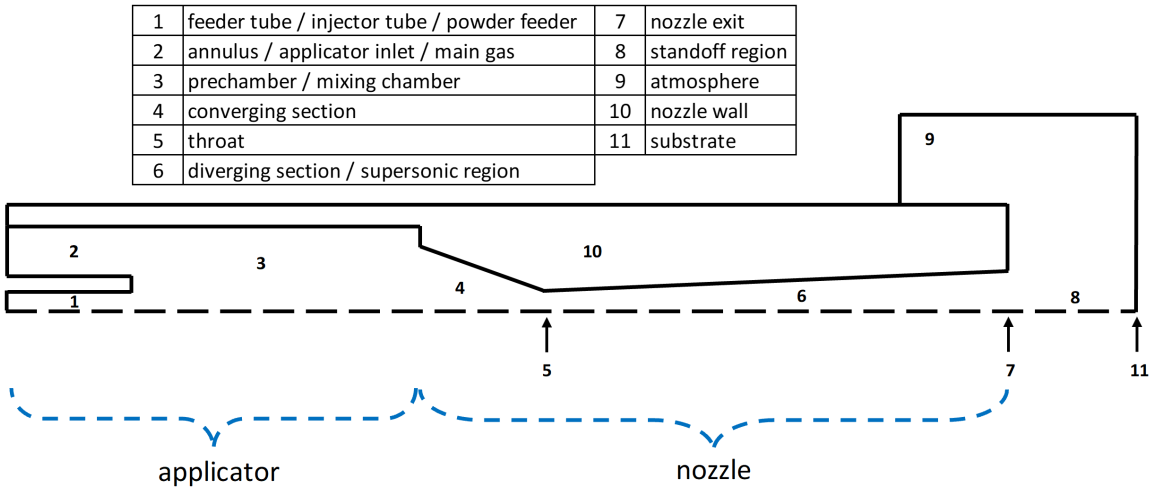

Figure 2: Nozzle Zone Names

One major issue with cold spray is nozzle clogging, which occurs when particles adhere to the inner nozzle wall rather than exiting the nozzle and adhering to the substrate [70]. The particles will accumulate on the wall (a phenomenon termed *fouling* in cold spray), effectively decreasing the inner diameter of the nozzle to the point that it clogs and cannot operate. Even as particles accumulate on the nozzle

wall before it completely clogs, the gas velocity is compromised because the working diameter has decreased, resulting in lower particle exit velocities, thus jeopardizing the particles' ability to bond to the substrate upon impact. The experiments in [81] show that cold spray nozzles may clog in just three minutes. In general, clogging occurs with dense powders and with low-melting-point powders. Specifically, aluminum [124], copper [94], nickel [109], stainless steel [113], Inconel [138], and titanium [109] are notorious clogging-prone materials. Clogging can occur prior to the nozzle in the injector tube as well [35], but the focus of this study is specific to nozzle clogging.

Clogging of cold spray nozzles is an expensive problem because they are usually made from specialized materials such as tool steels [63], alloys [63], plastics [86], carbides [109], and cermets [116]. The high cost of nozzles makes their frequent replacement impractical. Clogging is also troublesome because the operation window is drastically shortened, making it difficult to effectively spray a surface and finish a task. Nozzles can be cleaned and restored to proper specifications, but this requires inconvenient machining operations. Spraying a mix of clogging-prone powders with ceramic particles can keep the nozzle from clogging [51, 109], but it is not always favorable to risk the impingement of extraneous material on the substrate.

Wang et al. found that the two factors primarily responsible for clogging are a high-temperature nozzle wall and particle dispersion [132], and their conclusion is in harmony with other work. A copious amount of studies have concluded that increased substrate temperature better facilitates particle bonding in cold spray [134, 148, 99]. Since the hot applicator region transfers significant heat axially through the nozzle material [132], the substrate heating principle can be applied to the nozzle wall: the greater the nozzle wall temperature, the greater the particles' propensity for bonding to the nozzle wall will be, and the greater the propensity for particle-wall bonding, the greater the propensity for clogging.

Particle dispersion is the other primary culprit of clogging. Upon exiting the feeder tube and entering the prechamber, the particles disperse and occupy the entire prechamber volume [72]. This dispersion is likely promoted in multiple stages of the cold spray process. During their ten-foot journey from the powder feeder to the nozzle, the particles collide with the feeder tube wall a myriad of times, acquiring radial velocities before they even arrive at the nozzle. They carry those radial velocities into the prechamber, and their inertia prevents them from perfectly following the fluid streamlines, allowing for dispersion immediately upon entering the prechamber. Another factor contributing to dispersion in the prechamber is the shear produced by the cold gas from the powder feeder and the hot main gas from the applicator mixing at different velocities, which produces increased levels of turbulence in that region. This turbulence has potential to contribute to particle dispersion as well.

Furthermore, once the particles occupy the prechamber volume, they are bound to collide with the converging section of the nozzle just downstream, obtain significant radial velocities, and carry those radial velocities into the diverging section. Since there are also high levels of turbulence at the throat, there is an increased likelihood that particles will be scattered away from the centerline as they enter the supersonic region [72, 146]. Nozzle clogging occurs in the diverging section because it is in that region that particles reach critical velocity [70, 109]. When they collide with the wall at such speeds, they bond, accumulate, and eventually clog.

Although particle temperature is known to affect bonding in cold spray [105], several studies have indicated that particle temperature does not play the dominant role, both in cases of substrate heating [29] and specifically nozzle clogging [70]. Because it is not a primary factor for clogging, particle temperature will not be discussed at length in this study.

To better comprehend the clogging problem and to suggest methods of mitigating it, four computational fluid dynamics (CFD) efforts have been embarked upon in this

work, separated by chapter. To outline broadly, the first chapter addresses the first primary cause of clogging in cold spray (the high-temperature nozzle wall), while the last three chapters address the second primary cause (particle dispersion). In the first chapter, a summary of new nozzle cooling experiments is provided with simulations describing the effects that cooling has on the flow and ultimately on the particles. The second chapter presents simplified simulations of pressure fluctuations in the feeder tube which serve to inquire whether such flow oscillations, if present, would cause clogging. In light of the conclusion from chapter two that pressure oscillations can cause clogging, the third chapter is dedicated to implementing a more realistic and specific oscillating mass flow condition to determine whether the flow oscillations from the metering wheel are large enough to cause the clogging observed in experiments. Chapters two and three are based on specific clogging experiments [109]. The fourth chapter describes novel nozzle geometries and determines how effective they are at preventing clogging. A recommendation is provided for a nozzle geometry to be experimentally tested because it might completely prevent clogging. The final chapter summarizes the findings from chapters one through four and gives recommendations for future studies. ANSYS Fluent version 19.1 was used for all simulations in this work.

CHAPTER 1

NOZZLE COOLING WITH SUPERCRITICAL CO_2

1.1 Motive and Background

Because the high-temperature nozzle wall is a primary cause of clogging in cold spray [132], this study has sought to cool the nozzle wall to suppress clogging. Nozzle cooling has been implemented in many past works for this purpose. Wang et al. successfully prevented the clogging of aluminum powder by putting a home-made water cooling device on the nozzle [132]. Huang et al., in their study on the relationship between particle velocity and particle-substrate adhesion strength, used water cooling to prevent their copper particles from clogging [39]. Lehtonen et al. likewise relied on water cooling to avoid nozzle clogging and carry out their study [57], as did Singh et al. [108], Wong et al. [138], and others [125, 67]. Because of its effectiveness, water cooling of cold spray nozzles has become standard practice both in academia and industry [41].

The *ColdSpray PCS-1000* is a cold spray water cooling device [67] created by Plasma Giken with advertised capability to spray aluminum, copper and copper alloys, nickel and nickel alloys (including Inconel), stainless steel, and titanium [92], which are all clogging-prone powder materials [109]. The *ColdSpray PCS-1000* has made ground-breaking progress in clogging prevention, especially in its proven ability to deposit Inconel; first with a narrow particle size distribution [67] and later with a broader one [138], obtaining identical velocity and porosity results in both studies. Conventional water cooling methods have been unreliable at preventing clogging with Inconel.

As is common of industrial cold spray powder feeders [95], Plasma Giken's cooling device can accept a powder feed rate up to 500 g/min [92], which is large compared to those typically implemented in cold spray processes, providing users with the liberty to choose a preferable rate. The *ColdSpray PCS-1000* is rated to 1000 ℃ and 5 MPa inlet conditions [93], which covers most (but not all) relevant cold spray conditions.

Despite the successes of the *ColdSpray PCS-1000*, more progress must be made before the clogging issue is fully resolved. In their technical report, Vo et al. used the *ColdSpray PCS-1000* while spraying copper powder, and experienced clogging at 800 ℃ [125]. Upon lowering the applicator temperature from 800 ℃ to 600 ℃, the clogging ceased. Their report concludes: "Clogging is a general issue that limits the number of powders available for practical use in cold spray". Additionally, some cold spray processes employ a 6 MPa inlet pressure [100], which exceeds the allowable operating range of the *ColdSpray PCS-1000*.

The motive behind using supercritical CO_2 as a means of nozzle cooling stems from the limitations associated with using water. It is well-known that water has a freezing temperature of 273 K, which puts a lower-bound on its cooling capabilities. CO_2, on the other hand, is famous for being quite cold upon flashing and forming dry ice. Flashing occurs when the supercritical fluid experiences a sudden pressure drop below its critical point, causing a phase change from supercritical fluid to both solid and gas. The phase change to distinct gas causes the CO_2 to absorb energy from its surroundings, but the primary reason CO_2 becomes so cold when flashing is because it has a uniquely high Joule–Thomson coefficient [128]. The Joule–Thomson coefficient of a fluid determines how much its temperature changes when passing through a small orifice (or throttling valve). Because the Joule–Thomson coefficient for CO_2 is so high, it experiences a large temperature drop upon flashing, which is advantageous for cooling.

In-house lab measurements of flashing CO_2 recorded temperatures of 203 K - well below the coldest operating temperature of water. As a refrigerant, CO_2 presents major improvements, showing promise for expanding spray capabilities previously unattainable. Unlike the *ColdSpray PCS-1000*, the CO_2 cooling collar used in this study does not have limitations on allowable inlet conditions since it simply slides over the outer diameter of the nozzle without otherwise affecting the process. Of course, it does not necessarily follow that because the collar can be used with a 6 MPa inlet that it will eradicate clogging at that condition, but the present cooling jacket can at least be used at that condition. In addition to the thermal benefits, CO_2 is environmentally benign, non-hazardous, and inexpensive [73], which motivates its regular use in the food and beverage industry for refrigeration [13].

Another improvement that CO_2 cooling may provide is an ability to use nitrogen driving gas rather than helium for clogging-prone particles with high critical velocities. It is well-known in the field of cold spray that helium can achieve higher velocities than nitrogen can, and helium's advantage is due to its larger specific heat ratio and specific gas constant [88]. Helium is extremely expensive compared to nitrogen though, so the capability of using nitrogen instead is desirable. Although it is possible to reach higher particle velocities by increasing inlet temperature [6], there are drawbacks to this technique. As applicator temperature increases, the nozzle wall gets hotter, promoting clogging. Helium is often used because it enables clogging-prone powders to be sprayed at lower temperatures and reach the same velocity [140]. With CO_2 cooling, however, these low applicator temperatures may not be necessary. The cooling may be so effective that even high-temperature nitrogen cannot bring the nozzle wall to clogging-prone temperatures. The theory has not been tested, but if CO_2 does enable a switch to nitrogen, it will reduce costs appreciably. A limitation of this potential improvement is the spraying of low-melting-point metals like aluminum, which cannot be cold sprayed in the first place if exposed to gas temper-

atures above its melting point. For such metals, helium would still be required to reach high velocities.

The primary goals of the present cooling device are twofold: to make more powders sprayable without clogging and to allow more conditions for them to be sprayed at.

1.2 Experiments

1.2.1 Experimental Setup

The experiments in this study incorporated a novel nozzle cooling jacket that fits around the nozzle's outer diameter (see Figure 4), employing flashing CO_2 for cooling. The jacket was 3-D printed out of Inconel (which has a low ductile to brittle transition temperature) to avoid brittle material from fracturing and shattering with high-pressure and low-temperature CO_2. There are several stages for the CO_2 to undergo in this cooling process. It begins as a liquid in a pressurized tank and is transported through a siphon into a chiller. From there, it flows through a high-pressure pump, ensuring the fluid is supercritical. The CO_2 is constricted through a small capillary tube until it reaches the cooling jacket chamber (which envelopes the nozzle), where the volume increases, pressure drops, and the CO_2 flashes. Figure 3 shows a diagram of the cooling process as a whole, while Figure 5 presents an illustration of CO_2 flashing inside the collar and onto the nozzle.

The chiller used in this study was a Cool Clean® *LC CO_2 Liquid Condensing System* and the pump was a Cool Clean ® *LB-40 Liquid CO_2 Booster System.* The specific design features of the cooling jacket are not presented in this work but will be published elsewhere.

A *VRC Gen III Cold Spray System* was used to conduct these cooling experiments. Three powder materials were used in this study: two stainless steel powders (Praxair 17-4PH and FE-101) and a high-purity nickel (Praxair Ni-914-3). The 17-4PH and nickel powders were sieved to a minimum of 16 microns to avoid using fines (small

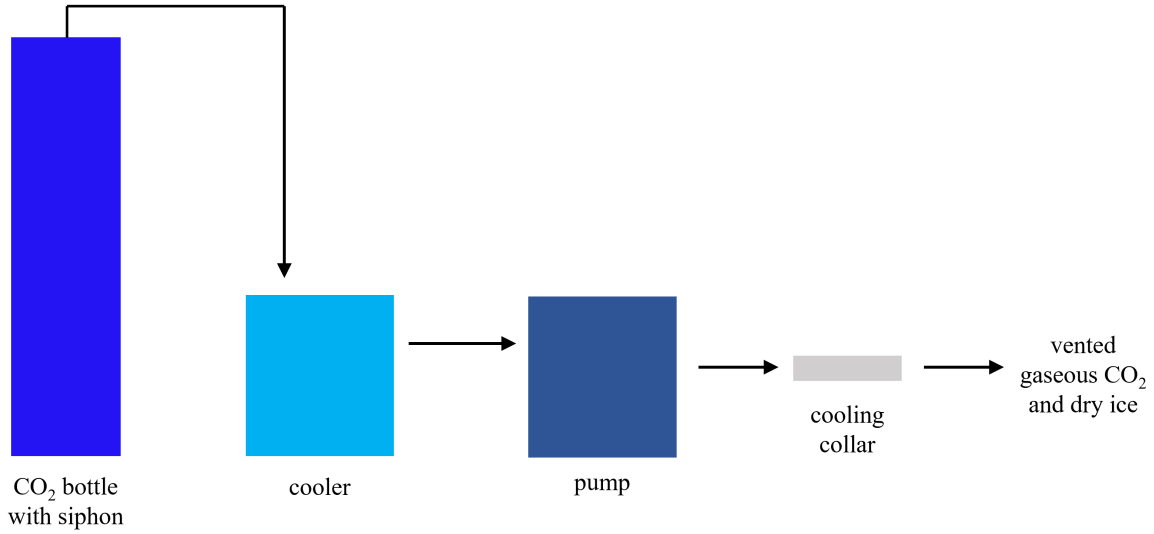

Figure 3: Overview of Cooling System

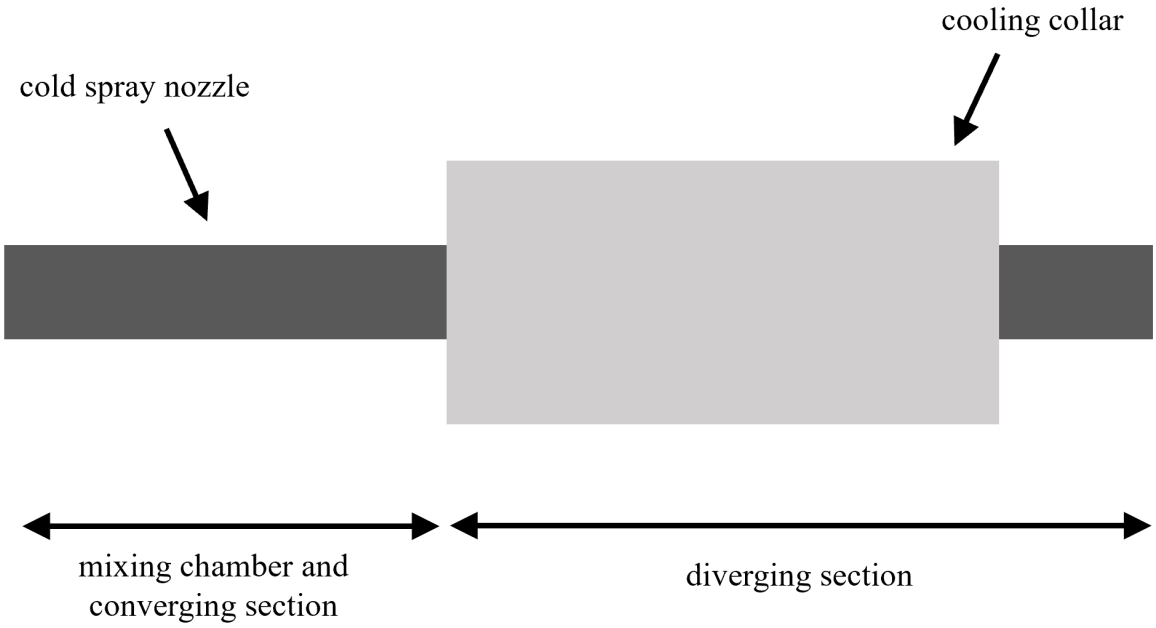

Figure 4: Illustration of Cooling Collar on Nozzle

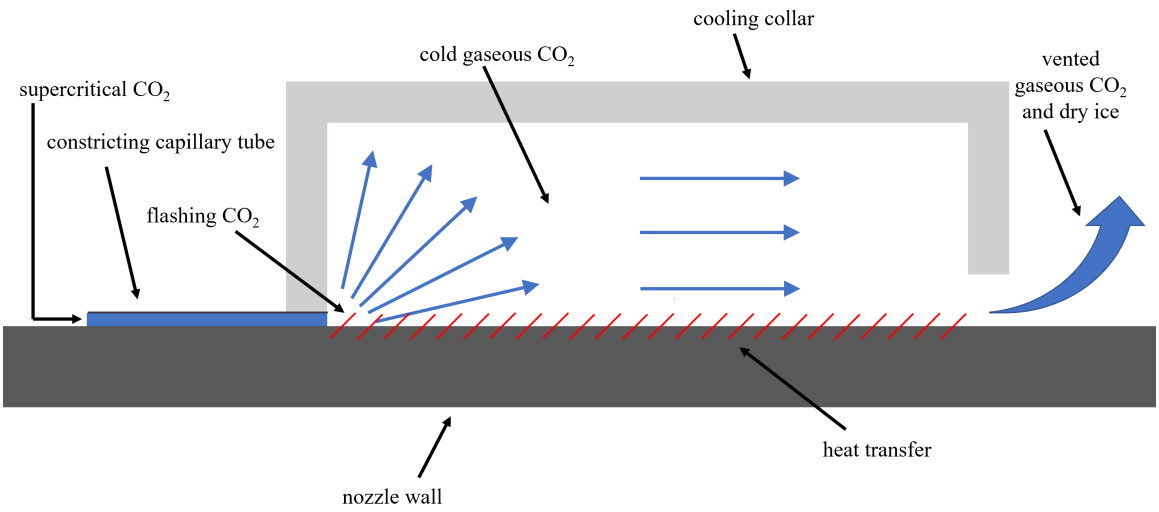

Figure 5: Illustration of Flashing CO_2 Inside Cooling Collar

particles), which are known to cause clogging [94], while the FE-101 was sprayed first without sieving and later after being sieved to a minimum diameter of 22 microns and a maximum of 46.

A common nozzle geometry made of tungsten-carbide was used, the dimensions of which are provided in Figure 6, and helium was used as the driving gas. An applicator condition of 600 °C and 3 MPa was used for the 17-4PH and nickel powders, while multiple applicator temperatures were used to spray the FE-101. The applicator pressure was 3 MPa for all experiments in this study. The feeder tube gas volumetric flow rate was 120 standard liters per minute (SLPM) and was measured at room temperature (293 K).

1.2.2 Experimental Results

The nickel and stainless steel powders sprayed in this study are known to clog at these conditions without cooling, and the results are summarized in Table 1. Without cooling, the nickel powder clogged in the diverging section near the throat while the stainless steel clogged at the nozzle exit. The results in Table 1 prove, at the very least, that CO_2 cooling can successfully deposit the same material that water cooling can

Table 1: Cooling Results with Nickel (Praxair Ni-914-3) and Stainless Steel (Praxair 17-4PH) Powders

Powder Material	Cooling Method	Observable Clogging
Ni-914-3	water	no
Ni-914-3	CO_2	no
17-4PH	water	no
17-4PH	CO_2	no

Table 2: Cooling Results with Stainless Steel (Praxair FE-101) Powder

Applicator Temperature	Cooling Method	Sieved	Observable Clogging
350	CO_2	no	yes
500	CO_2	no	yes
350	water	no	yes
500	water	no	yes
350	water	yes	no
500	water	yes	no
600	water	yes	yes

without clogging. A goal for future experiments is to demonstrate a superior ability to mitigate clogging with CO_2, but a preliminary study needed to be completed first.

The FE-101 results in Table 2 serve to demonstrate some limitations of nozzle cooling with both CO_2 and water. In past works, FE-101 powder was found to clog when helium applicator temperatures exceeded 350 °C and with particle diameters ranging from 15 to 45 microns [2]. In the present study, when the powder was not sieved, it always clogged regardless of inlet conditions and cooling material, including at 350 °C and 3 MPa, which is a condition known to be acceptable when the minimum particle diameter is 15 microns [2]. At a condition where cooling is not necessary when fines are sieved out, clogging occurred with fines present even when cooling was applied.

Upon sieving to a minimum particle diameter of 22 microns and a maximum of 46, clogging ceased with the water cooler until the applicator temperature reached

600 °C, at which point fouling resumed. There is an applicator temperature limit at which water cooling cannot prevent clogging, which is a similar result to conclusions found in other works [125]. At present, an experiment with sieved FE-101 powder has yet to be conducted with the CO_2 cooler.

It is already well-known that small particles and high applicator temperatures promote clogging, but the conclusion that fines promote clogging even with nozzle cooling breaks new ground. Evidently, cooling cannot entirely mitigate the clogging effect of fines, even with CO_2. Table 2 shows that cooling is effective for FE-101 particles larger than 22 microns, but there is a limiting diameter below 22 microns at which cooling cannot prevent clogging. A valuable future study could involve identifying this limiting diameter, but the limit would probably be unique for each powder material and thus be inconvenient to obtain.

The most crucial future study is to test more powders and inlet conditions with the CO_2 cooler, especially those for which water cooling fails to prevent clogging. Although it may expand spray condition possibilities for certain powders, cooling alone cannot prevent clogging for all materials of all particle sizes, especially fines. If clogging is to be completely eradicated, other methods of clogging prevention must be incorporated as well. Such methods are presented in chapter four. Regardless, CO_2 cooling shows promise for better suppressing clogging, and thus it is worth investigating further.

1.3 Modeling

1.3.1 Purpose of Computational Work

The primary purpose of the CFD in this work is to evaluate whether particle velocity or temperature are substantially altered by cooling the nozzle. Concern has been raised both in literature [151] and in technical discussions that the particles may

be so affected that the deposit is compromised, and this computational effort seeks to address those concerns.

1.3.2 Modeling Methodology

1.3.2.1 Boundary Conditions

A 2-D axisymmetric model was used for all simulations in this chapter. The nozzle geometry was modeled according to those used in the experiments, and an axisymmetric schematic of its dimensions is provided in Figure 6. The interior walls of the nozzle were given the no-slip condition and were thermally coupled to the fluid flow. The outlets were set to atmospheric conditions: zero gauge pressure and 293 K. There was no heat transfer computed between the fluid and the feeder tube wall, and likewise for the substrate, since those heat transfer effects are not the focus of this study. Nozzle cooling was modeled by applying a temperature boundary condition on the exterior nozzle wall of 203 K, which was the in-lab measurement of that wall upon flashing CO_2 without any driving gas flowing through. Although methods exist for modeling heat transfer effects with flashing CO_2 [12], a fixed temperature boundary makes the simulations appreciably simpler. Plus, the nozzle is almost certainly warmer than 203 K while operating due to high driving gas temperatures, which ensures cooling effects are not understated in the present models.

For simulations where the nozzle was not cooled, the outer wall (represented by a blue line in Figure 6, dimension O) was set to adiabatic. Throughout this study, the *adiabatic* case refers to the simulation with an adiabatic outer nozzle wall, while the *cooled* case refers to the simulation with a cooled outer wall.

In the experiments, the feeder tube volumetric flow rate was set to 120 SLPM and the main gas was measured at roughly room temperature (293 K). Because Fluent requires a mass flow rate as input rather than a volumetric flow rate, the volumetric flow rate was converted into a mass flow rate by using equations 1-3. First, the

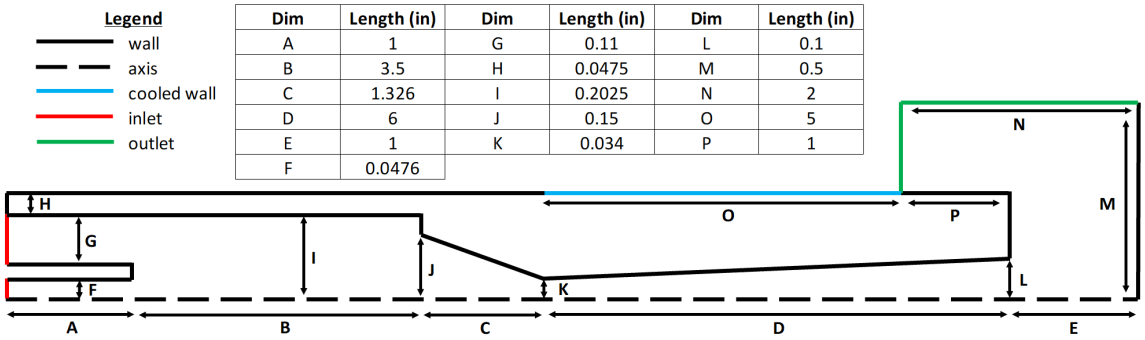

Dim	Length (in)	Dim	Length (in)	Dim	Length (in)
A	1	G	0.11	L	0.1
B	3.5	H	0.0475	M	0.5
C	1.326	I	0.2025	N	2
D	6	J	0.15	O	5
E	1	K	0.034	P	1
F	0.0476				

Figure 6: Nozzle Geometry (with Wall)

volumetric flow rate in SLPM was corrected for pressure, providing a flow rate in liters per minute (LPM):

$$\dot{V}_{LPM} = \dot{V}_{SLPM} \frac{T_f}{T_{room}} \frac{14.696}{P_{f,psi}} \tag{1}$$

Next, the helium density at the feeder tube inlet was obtained with the ideal gas law:

$$\rho_f = \frac{M \times P_f}{R \times T_f} \tag{2}$$

Finally, the mass flow rate was computed:

$$\dot{m} = \dot{V}_{LPM} \times \rho_f = 0.33296 \; g/s \tag{3}$$

The annulus (dimension G in Figure 6) was held at constant temperature and pressure throughout the experiments, but in this computational work it was the subject of a parameter study; the temperatures being 673 K and 873 K and the pressures being 3 MPa and 4 MPa. The feeder tube inlet (dimension F in Figure 6) was held at a constant 0.33296 g/s and 293 K.

The boundary between the solid nozzle wall and the atmosphere (dimension P in Figure 6) was thermally coupled in this study, despite conventional practice in cold spray being to set this boundary as heat-insulated [147]. It was desirable to allow heat

transfer at dimension P because the gas flow exiting the domain passing by the nozzle tip has a convective cooling effect, even if only slight. Since the aim of this study is to ascertain cooling effects, the cooling effects at the nozzle tip were computed.

1.3.2.2 Mesh Description

A mesh dependence study with a large range of mesh sizes was conducted, and although it was preferable to use a finer (larger) mesh, especially in the supersonic region, it was not computationally feasible due to the number of simulations involved in this project. In particular, when cell layers are added near the fluid-wall interface, the wall time required for convergence was considerably increased. The mesh finally implemented in this study consisted of 186,860 quadrilateral cells, and its specifications based on zone name are provided in Table 3.

Six thin cell layers were applied to each side of the fluid-wall boundary in an effort to resolve the flow features near the wall and the solid wall temperature at the boundary. The wall yplus values ranged from 0.0004 near the nozzle exit and 0.0225 at the throat, which are well within recommended values for computing heat transfer in supersonic converging-diverging nozzles [152].

Table 3: Mesh Specifications Based on Zone Name for Cooling Simulations

Zone	Cell Size (mm)
inlets	0.2
prechamber	0.2
converging	0.2
diverging	0.05
standoff	0.1
atmosphere	0.4
nozzle	0.4

1.3.2.3 Gas Phase Modeling

Since the flow is supersonic and compressible, the density-based implicit solver was required. All simulations were converged to first-order accuracy. The helium density was set to vary according to the ideal gas law, while a temperature dependent thermal conductivity and viscosity were implemented according to the correlation equations in Kreith and Manglik's textbook [53]. The thermal conductivity formula is presented in equation 4 and the viscosity formula is presented in equation 5:

$$k = \left[88.89 + \left(93.04 \times 10^{-2}\right)T + \left(-1.79 \times 10^{-4}\right)T^2 + \left(3.09 \times 10^{-8}\right)T^3\right] 4.186 \times 10^{-4} \tag{4}$$

$$\mu = \left[54.16 + \left(50.14 \times 10^{-2}\right)T + \left(-89.47 \times 10^{-6}\right)T^2\right] 10^{-7} \tag{5}$$

where the units of k are W/m-K and the units of μ are kg/m-s.

Figure 7 depicts how, according to several sources [53, 89, 91, 122, 135], the thermal conductivity and viscosity vary across the relevant temperature range of this cold spray operation. Kreith and Manglik's correlation equations [53] for viscosity and thermal conductivity strongly agree with Petersen's viscosity equation [91] and Vargaftik and Yakush's thermal conductivity equation [122]. Three renditions of the Sutherland Law are depicted, some showing better agreement than others. The Sutherland Law is a gas viscosity approximation, resulting from a kinetic theory, that uses an idealized intermolecular force potential [117]. The formula is:

$$\mu = \mu_0 \left(\frac{T}{T_0}\right)^{3/2} \frac{T_0 + S}{T + S} \tag{6}$$

where μ_0 is a reference value for viscosity, T_0 is a reference value for temperature, and S is an effective temperature, also called the *Sutherland constant*. Each gas

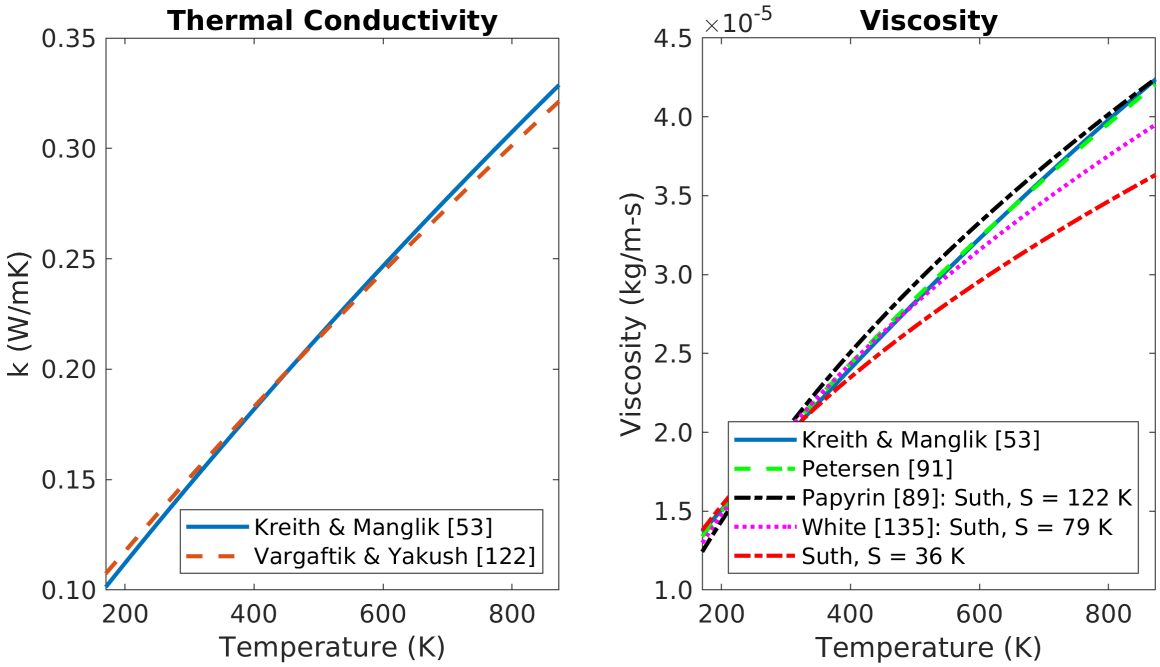

Figure 7: Temperature-Dependent Helium Gas Properties

has its own unique Sutherland constant. Most cold spray studies assume a constant gas viscosity, but when the viscosity's temperature dependence is accounted for, the Sutherland Law is almost always the method used [147]. Despite the Sutherland Law being incorporated with some regularity, the literature to date lacks unanimity as to the value of S for helium. In his textbook on viscous flow, White provides a value of $S = 79\ K$ [135], while Papyrin et al. provide a value of $S = 122\ K$ in their book on the cold spray process [89]. Both results are plotted in Figure 7. Papyrin's Sutherland constant seems most justified since it results in a viscosity closer to those produced by Petersen and Krieth and Manklik, whereas White's Sutherland constant produces a viscosity that deviates from Petersen and Krieth and Manklik's. Of course, Petersen and Krieth and Manglik are not necessarily correct because they agree, but in light of the inconsistent Sutherland constants between Papyrin and White, and the excellent agreement between Petersen and Kreith and Manglik, Kreith and Manglik's correlation equations were used in these simulations. Plus, the Sutherland Law is an

approximation for all gases, whereas Petersen and Kreith and Manglik's equations are specific to helium. There is a simplified version of the Sutherland Law used in some cold spray studies [58, 83] that uses two coefficients instead of three (the three-coefficient version is given in equation 6), but it is seldom used for helium and thus it will not be expounded upon in this study.

To exemplify the repercussions of selecting an improper Sutherland constant, a third Sutherland curve with $S = 36\ K$ was included in Figure 7. Since White's constant is 43 below Papyrin's, this exemplifying constant was set to 43 below White's. Admittedly, the curves in Figure 7 representing $S = 122,\ 79,$ and $36\ K$ are somewhat close, and certainly describe viscous effects better than a constant viscosity assumption does. The difference is still noticeable though, and could result in inaccuracies especially in simulations predicting cooling effects where the boundary layer temperatures differ drastically between the *cooled* and *adiabatic* cases.

Because an improper Sutherland constant can have potentially significant consequences, future cold spray studies should be more careful to include the constants they used. Several cold spray studies that incorporate the Sutherland Law do not include the Sutherland constant they used, or even whether they used the two or three-coefficient version of the Sutherland's Law [4, 32], which leaves room for uncertainty with helium. The Sutherland constant for nitrogen is more consistent throughout the literature, with Sutherland himself [117] providing a value of $S_{N_2} = 109\ K$ and White providing $107\ K$ [135].

The k-ϵ realizable turbulence model was used to predict the turbulence effects in this chapter. After comparing the results of several turbulence models with this nozzle geometry, the k-ϵ realizable model was implemented because it produced a peak in turbulence at the throat, which is physically likely according to Lupoi and O'Neill [72] and Yin et al. [146]. Furthermore, when Zhalehrajabi et al. evaluated the ability of three different turbulence models to predict heat transfer inside a supersonic

converging-diverging nozzle, they found the k-ϵ model outperformed the k-ω and k-ω SST models [152]. They did not evaluate the k-ϵ realizable model specifically, but the k-ϵ and k-ϵ realizable models at least have similar forms with transport equations for k (turbulent kinetic energy) and ϵ (turbulent dissipation rate) [26]. Plus, the k-ϵ realizable turbulence model has been used in many cold spray studies [147]. Admittedly, the turbulence was not fully resolved in the supersonic region because a sufficiently fine mesh could not be afforded. Standard wall functions were used at the nozzle wall boundary.

1.3.2.4 Discrete Phase Modeling

The Discrete Phase Model (DPM) with Lagrangian particle tracking was required to obtain the individual particle trajectories [137]. Neglecting all body and surface forces other than drag, the particle equation of motion reduces to:

$$\frac{du_p}{dt} = F_D\left(u_f - u_p\right) \tag{7}$$

Gravitational effects were neglected in this study because cold spray nozzles do not have a standard orientation relative to the direction of gravity; nozzles are often fixed at an angle relative to the substrate [108] or even hand-held [24], rendering gravity's inclusion futile. It should be noted though that in reality, gravity has some effect on the particles [153].

The drag force in Fluent's DPM [26] is provided in equation 8:

$$F_D = \frac{18\mu}{\rho_p d_p^2}\,\frac{C_D Re}{24} \tag{8}$$

The high-Mach-number drag law, created by Clift et al. [18], was used to calculate the coefficient of drag for the spherical particles because it properly corrects for particle Mach numbers greater than 0.4 and particle Reynolds numbers greater

than 20 [26]. The high-Mach number drag law defines the drag coefficient with the following equation:

$$C_D = \frac{24}{Re_p}\left(1 + 0.15Re_p^{0.687}\right) + \frac{0.42}{1 + 4.25 \times 10^4 Re_p^{-1.16}} \tag{9}$$

Particles were tracked stochastically using the Discrete Random Walk (DRW) model, which incorporates instantaneous turbulent velocity fluctuations on the particle trajectories via stochastic methods [26]. The particles were one-way coupled to the fluid in this chapter, not necessarily because that assumption is realistic, but because it is unlikely that the magnitude of particle cooling depends on two-way coupling effects.

Since the particles are assumed to maintain uniform temperature throughout their volume [26], the convective heat transfer at the particle surface is governed by the equation:

$$m_p c_p \frac{dT_p}{dt} = hA_p(T_\infty - T_p) \tag{10}$$

The heat transfer coefficient and Nusselt number were computed with the correlation of Ranz and Marshall [97, 98], provided in equation 11. Liao and Lucas show that Ranz and Marshall's correlation accurately predicts heat transfer rates on solid spheres at high Reynolds numbers [65], affirming the Ranz and Marshall correlation is valid for cold spray conditions.

$$Nu = \frac{hd_p}{k_\infty} = 2.0 + 0.6Re_d^{1/2}Pr^{1/3} \tag{11}$$

Cold spray particles remain entirely in the solid state and chemically inert during their journey through the nozzle [106]. Although combustion and chemical reactions with cold-spray-sized metal particles are possible [27], these phenomena occur when there are oxides present on the particle surface, which the cold spray particle atomization process intentionally minimizes [15].

In each simulation of this chapter, 5,000 particles were injected into the domain at room temperature with zero initial velocity and diameters distributed uniformly randomly from 5 to 100 microns. This diameter range was not implemented to accurately replicate the diameter distribution in the experiments, but rather to make conclusions about particle behavior based on diameter. To model a particle injection, particles were randomly generated inside the entire feeder tube volume with a preference away from the axis by a factor of the square root of radial position. This preference ensured a uniform particle location density as if the particles occupied a 3-D space, which accounted for the 2-D axisymmetric assumption. Particles in these simulations replicated the stainless steel Praxair 17-4PH powder, with an assigned density of 7800 kg/m^3 and specific heat capacity of 460 J/kg-K [75].

1.3.3 Modeling Results

1.3.3.1 Contours

Contours of the experimental condition, with a 3 MPa and 873 K annulus condition, are provided in Figure 8. The cooled results are provided on top, contrasted by the adiabatic results which mirror them underneath. The most significant difference between the adiabatic and cooled cases is in the solid nozzle wall, which is observed to cool radially from the outer wall to the fluid-wall interface. In the inlet and prechamber regions, there are no noticeable differences between the adiabatic and cooled nozzles, but the wall temperature begins to differ between the cases at the converging section. Although cooling only begins at the throat (see Figure 6), the conductive heat transfer occurs lengthwise in addition to radially, cooling the converging wall section as well.

The boundary layer is noticeably warmer than its cold surroundings due to viscous heating. The high temperature in the solid nozzle tip (near the exit) is caused by viscous heating too. The nozzle tip is hotter than the atmosphere, which reveals

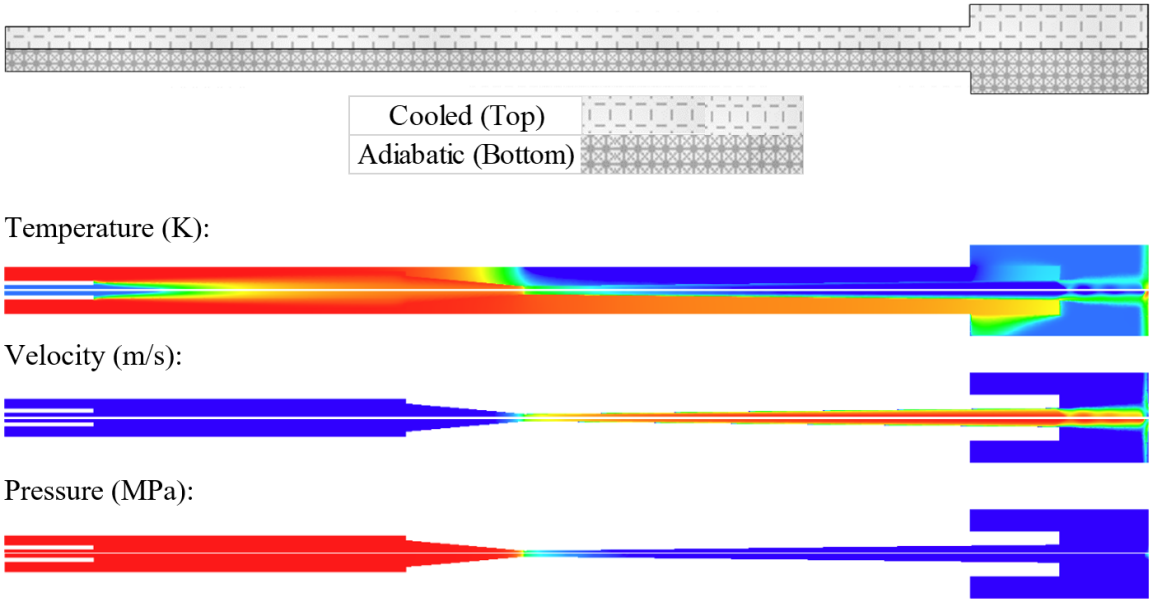

Legend:

Temperature (K):		Velocity (m/s):		Guage Pressure (MPa):	
	870		2550		3.0
	750		2190		2.6
	650		1800		2.1
	550		1450		1.7
	450		1100		1.3
	350		750		0.9
	250		350		0.4
	170		0		0.0

Figure 8: Contours of Experimental Condition, Cooled and Adiabatic

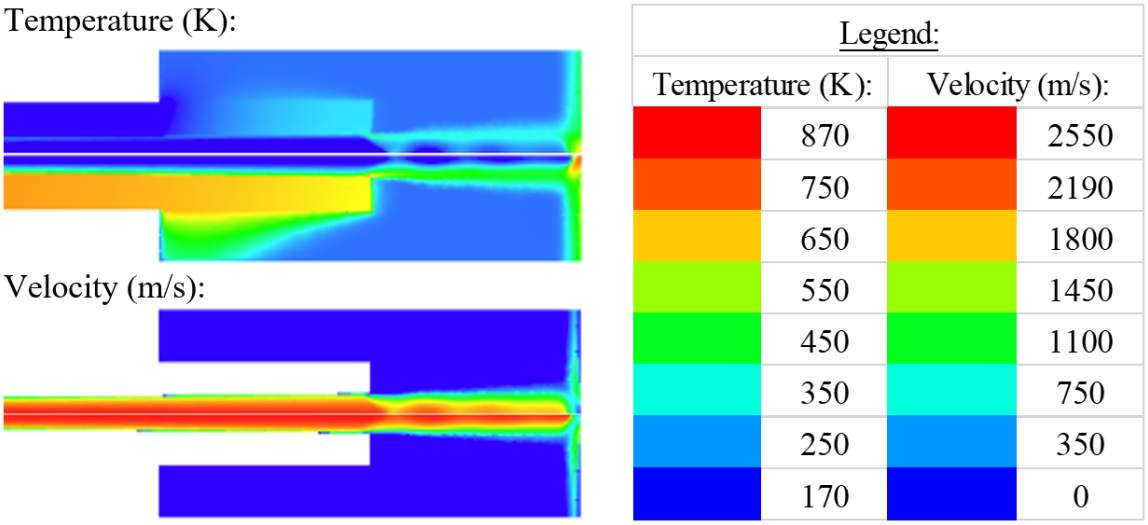

Figure 9: Magnified Contours of Nozzle Tip and Standoff Region, Cooled and Adiabatic

that the tip heats the atmosphere, rather the other way around. Evidently, the hot boundary layer acts as an insulator on the nozzle tip. Further confirming this hypothesis is the boundary layer temperature being nearly equal to the tip temperature, which suggests that the boundary layer transmits heat efficiently to the nozzle tip which, in turn, transmits heat (less efficiently) into the atmosphere. In the next design iteration of the CO_2 cooling collar, the cooling will span the entire length of the diverging section (including dimension P of Figure 6) in order to cool as much of the clogging-prone region as possible.

As expected, the pressure starts high at the inlet and sharply decreases at the throat, exiting at low pressure after expanding. The gas velocity is observed to change in proportion to the temperature, the significant differences between the cooled and adiabatic velocity contours being in the standoff region, which Figure 9 magnifies. In the standoff region, the velocity fluctuates in both cases due to Mach diamonds, but the velocity is consistently higher in the adiabatic case.

1.3.3.2 Nozzle Wall Properties

To gauge the effectiveness of the cooler at reducing wall temperature, the inner nozzle wall temperature is provided in Figure 10 for the inlet condition in the experiments (3 MPa and 873 K). In addition to the simulations based on the experimental setup, another simulation was run with a cooled condition (outer wall boundary condition of 203 K) on both dimension O and dimension P (see Figure 6), rather than only on dimension O. In Figure 10, the *cooled short* case is that which is cooled only on dimension O (representing the actual cooler length), and the *cooled long* case is cooled on both dimensions O and P. This additional simulation was conducted to ascertain how the nozzle would behave if it were cooled along its entire length.

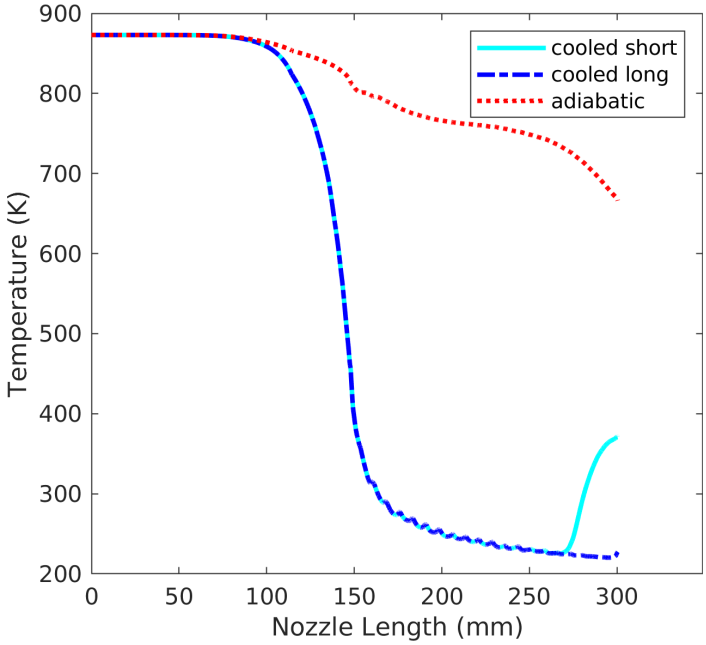

Figure 10: Inner Wall Temperature vs Nozzle Length

Figure 10 clearly shows a maximum wall temperature in the inlet and prechamber region for all cases, which is due to the high applicator temperature. These wall temperature profiles are in excellent agreement with those of Wang et al. [132]. They are not in agreement, however, with those of Li et al., who found a maximum temperature at the throat in their study on temperature distribution in the substrate

and nozzle wall (without cooling) [63]. The nozzle geometry in Li et al.'s study is quite different from that of the present study in that it lacks a prechamber - the feeder tube is located inside their converging section. This cannot explain the difference in wall temperature profiles though, because Wang et al. produced the same temperature profile as that of this study with a very similar nozzle geometry to Li et al.

The cause of this discrepancy could be due to an insufficient mesh in Li et al.'s study. They used several meshes depending on substrate location and shape, which ranged in grid number from 36,660 to 111,140. Wang et al., on the other hand, mention that their study required 240,200 to achieve a grid-independent solution. Both studies used similar nozzle geometries, yet Li et al.'s largest mesh was still less than half the size of Wang et al.'s. Moreover, while Wang et al. only meshed the driving gas domain, nozzle wall, water coolant domain, and a small atmospheric region, Li et al. also meshed the substrate and a massive atmospheric region. If Wang et al. required 240,200 to reach a grid-independent solution, Li et al. likely needed a larger (or at least equal) mesh size to resolve thermal features in more regions (namely the substrate). Additionally, since Li et al.'s mesh size only depended on the substrate size and location, their 36,660 cell mesh is actually more representative of their mesh quality in the nozzle region than their 111,140 cell mesh is because the extra cells were dedicated to the substrate, not the nozzle wall. Li et al.'s nozzle mesh was only 15% of the size of Wang et al.'s, so if they disagree, Wang et al.'s mesh is more likely to produce accurate results.

In the present work, a mesh dependence study was conducted and, although all the flow features in the diverging section are not completely resolved, Figure 10 demonstrates that the temperature at the nozzle wall is almost completely resolved, so there is good reason to trust the nozzle wall temperature profiles in the present study.

According to Figure 10, the cooling jacket makes a roughly 500 K difference in wall temperature - a remarkable cooling effect. It is important to notice from this figure the repercussions of using a cooling jacket that does not extend the full length of the diverging section: viscous heating increases the uncooled nozzle tip by nearly 200 K, possibly promoting clogging in that warm region. It is especially important that the nozzle tip is cooled when spraying powders prone to foul towards the exit, like the steel powders in the present study and the nickel powder in Luo et al.'s study [70]. It is likewise necessary that a cooling jacket begins cooling at the throat, as the present design does. If the jacket begins earlier than the throat, energy will be removed from the hot applicator gas at the detriment of particle velocity downstream. If the jacket begins too far downstream from the throat, certain particles may begin clogging between the throat and the cooler due to the exposed high-temperature region. The cooling collar should begin precisely at the nozzle throat and end precisely at the nozzle exit.

1.3.3.3 Centerline Flow Properties

Although the experiments were conducted at inlet conditions of 3 MPa and 873 K, four different sets of inlet conditions were evaluated in this CFD project to understand how nozzle cooling affects a variety of cold spray scenarios, since a long term goal of this project is to apply a cooling jacket to any combination of cold spray nozzle, powder, and inlet condition. These particular conditions (3 MPa, 4 MPa, and 673 K, 873 K) were selected for a parameter study because they are common inlet conditions in cold spray. For each of the four inlet combinations, both a cooled and adiabatic nozzle were simulated so that the particles from the cooled nozzle could be compared to identical particles from the adiabatic nozzle.

Figure 11 compares the cooled and adiabatic centerline velocities for the four different inlet conditions. In both the cooled and adiabatic nozzles, higher inlet

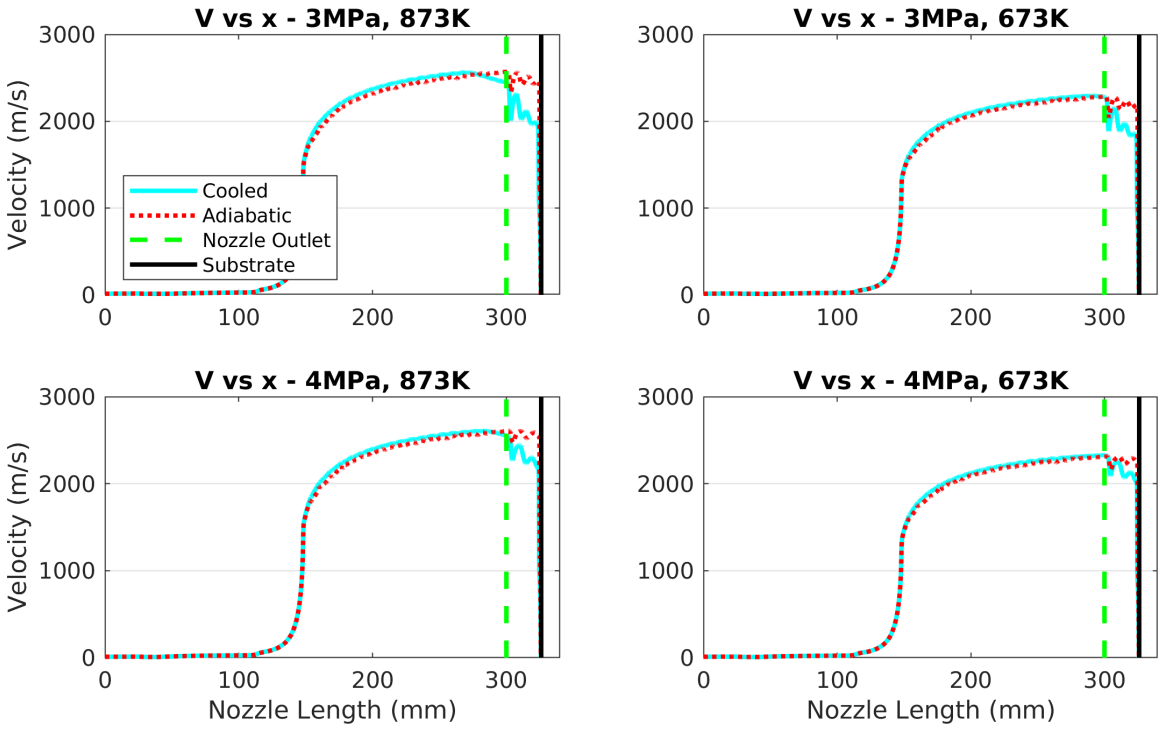

Figure 11: Centerline Velocity vs Nozzle Length – Annulus Parameter Study

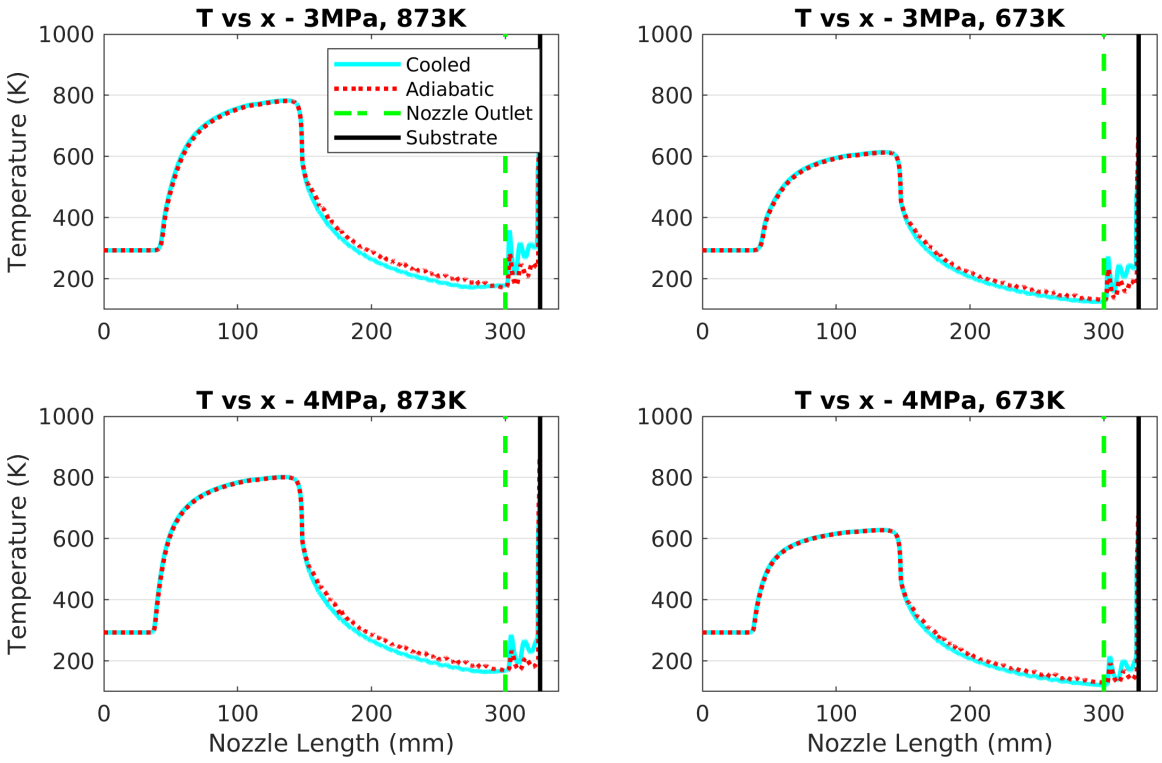

Figure 12: Centerline Temperature vs Nozzle Length – Annulus Parameter Study

temperatures result in higher gas velocities, which agrees with the findings of Yin et al. [144]. For the most part, there is close agreement between the two nozzles, an exception being in the standoff region and nearby, where the cooled nozzle's velocity is observed to drop below that of the adiabatic nozzle's. In the standoff region, Mach diamonds are observed with both the cooled and adiabatic nozzles, but the gas from the cooled nozzle is slower for all inlet conditions. This standoff region behavior is consistent with Figure 9. The behavior observed in Figure 12 is explained by the cold feeder tube gas mixing with that of the hot annulus. Since the feeder tube is located at the centerline, the centerline temperature will be equal to that of the feeder tube until the feeder tube terminates and the cold gas is met by the hot stream of annulus gas, where mixing begins. As mixing continues, the centerline temperature will continue to increase until the throat, after which point the temperature decreases in proportion to the velocity. These centerline temperature profiles indicate that the prechamber in the present study allows for ample mixing, which agrees with the findings of Tang et al. [119].

Interestingly, and counter to the results in Wang et al.'s study, Figure 11 shows that the centerline velocity in the cooled nozzle is faster than the adiabatic nozzle velocity. This counterintuitive phenomenon is explained by Anderson [5]: when heat is added to supersonic compressible flow, velocity decreases, and when heat is removed, velocity increases. Granted, this phenomenon is demonstrated by Anderson for one-dimensional flow while the present flow is two-dimensional, but the general principle still holds even if there are other factors at play.

As far as the disagreement with Wang et al. [132], who find the centerline flow velocity in the adiabatic nozzle to be faster throughout the entire diverging section, a few explanations are possible. First of all, they used air as their driving gas, while the present study uses helium. The thermal conductivity of helium is 10 times that of air, which makes the gas in the present study more susceptible to heat transfer effects

while the air in Wang et al.'s is more resilient to temperature changes. Furthermore, because helium is much less dense than air, its Mach number in the nozzle will be larger air, which renders the helium in this study still more susceptible to Anderson's compressible flow effects than air. Another important difference is that this study used a substantially different nozzle geometry than Wang et al., which directly affects the flow profiles of the two solutions. Also, the CO_2 cooler brings the inner nozzle wall down to a temperature of 225 K, whereas Wang et al. only brought their nozzle temperature to around 325 K. It is to be expected that Wang et al. would experience less cooling effects when they cooled their nozzle less than the nozzle in the present study. A criticism of Wang et al.'s work is that they assumed constant viscous and thermal properties for their driving gas, which are less accurate than temperature dependent-properties. Regardless, there are enough differences between this study and Wang et al.'s that both answers are plausible. There is good reason to trust the results in the present work, especially because specific temperature-dependent viscosity and thermal conductivity equations for helium were incorporated.

There is a peculiar velocity drop *inside* the cooled nozzle near the exit for the inlet condition of 3 MPa, 873 K, and a similar (but less aggressive) velocity drop is found at the 4 MPa, 873 K condition. This cannot be due to shocks or overexpansion, because the changes would be far more abrupt. The existing studies on the effects of nozzle cooling in cold spray have incorporated either nitrogen [34] or air [132] as a driving gas, which may explain why this issue was not identified prior to this study.

Figures 13 and 14 are included to ascertain whether the velocity drop observed in Figure 11 is caused by the cooling collar leaving the nozzle tip uncooled, or if it is due to more general cooling phenomena. As Figures 13 and 14 demonstrate, the cooled short and cooled long cases produce nearly perfectly matching velocity profiles, including in the standoff region, which indicates the velocity drop is independent of the span of cooling.

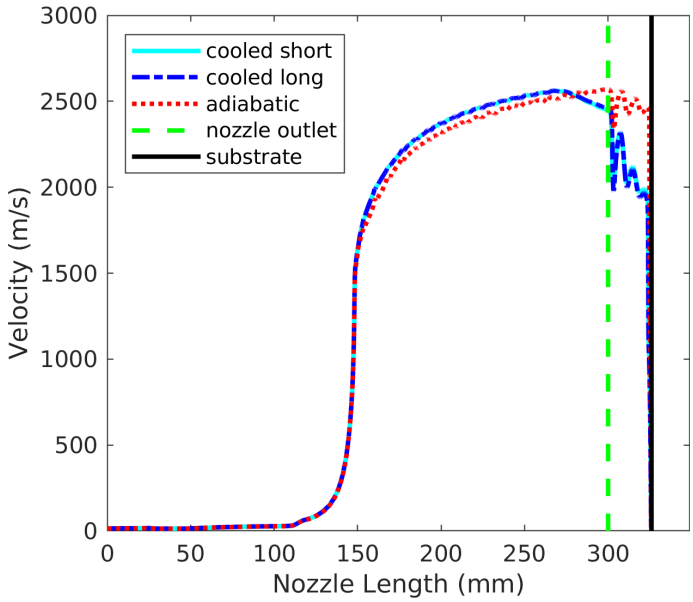

Figure 13: Centerline Velocity vs Nozzle Length – Experimental Annulus Condition

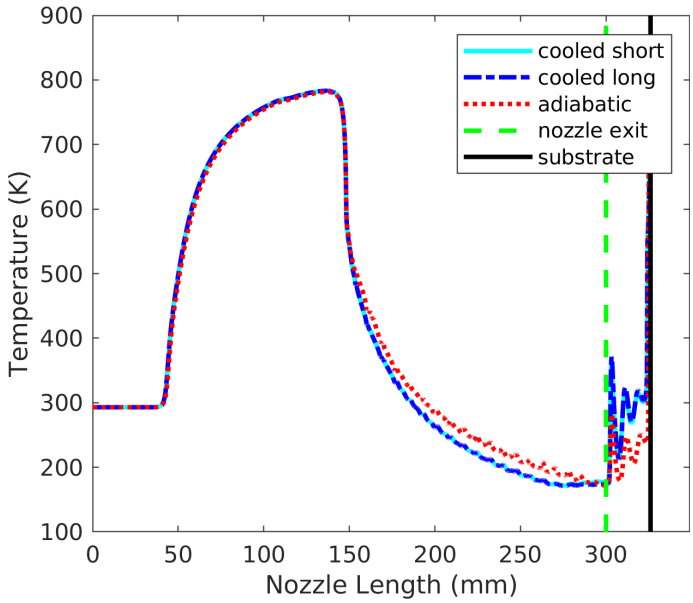

Figure 14: Centerline Temperature vs Nozzle Length – Experimental Annulus Condition

If the cooling span were the cause of the velocity drop, the centerline properties would differ between the cooled short and cooled long cases. Unfortunately, Wang et al. did not provide their velocity profiles in the standoff region. It would have

been valuable to compare these results to theirs. Meyer and Lupoi's CFD work presented a comparable but appreciably less severe velocity drop in the same region of the diverging section using nitrogen as the driving gas [78]. Although their inlet conditions were similar to those in the present study (3 MPa, 350°C), they make no mention of cooling their nozzle. Meyer and Lupoi did not provide an explanation for why the gas velocity behaved this way, but the reasons for the velocity drop observed in the present study are considered in the *Bulk Flow Properties* section.

Since there is a difference in standoff region velocity profiles between the cooled and adiabatic cases, it is worth noting that in some studies, an additional force term was included in the particle equation of motion to account for particle deceleration due to the adverse pressure gradient caused by the bow shock near the substrate [102]. A future study could incorporate this term, but it seems unlikely that such a small loss in velocity would result in a significant particle velocity detriment. Most cold spray studies do not incorporate this extra pressure gradient surface force term [147].

1.3.3.4 Bulk Flow Properties

Existing studies on cold spray nozzle cooling have largely determined that the flow is not significantly compromised by cooling, but have also largely neglected to properly investigate the bulk flow characteristics. Wang et al. exclusively relied on centerline flow properties to inform their conclusion that gas flow was unaffected by cooling [132]. Although the centerline properties are valuable in determining whether or not cooling impairs the flow field, it is insufficient to make that determination with centerline characteristics alone. After all, the particles do not adhere to the nozzle centerline but disperse, being exposed to gas flow characteristics both near and far from the centerline. The bulk flow properties must be accounted for to fully comprehend how cooling affects the driving gas, and consequently the particles.

Fukanuma and Huang, in their nozzle cooling study, did investigate the flow properties along the inner radius of their cold spray nozzle [34]. They concluded that because their temperature and velocity profiles were only slightly different along the radius between their cooled and adiabatic cases, that ultimately "there was no considerable effect on gas velocity [due to cooling]". The current study presents similar radial flow data to Fukanuma and Huang. Additionally provided are results of mass-weighted-averaged velocities and temperatures at various slices in the diverging section, which are unanticipated and informative. All bulk flow results are from the cases with inlets of 3 MPa and 873 K, matching the experiments.

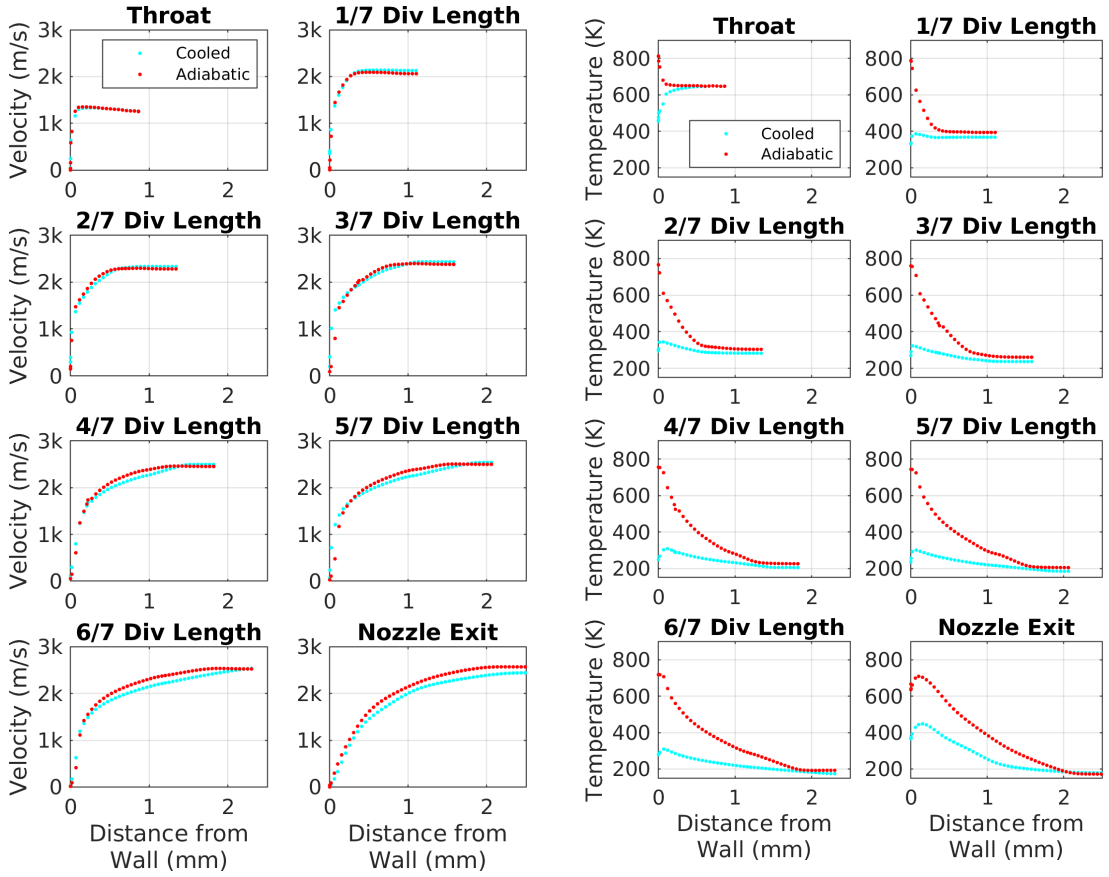

a) Velocity vs Distance from Wall

b) Temperature vs Distance from Wall

Figure 15: Flow Properties from Nozzle Wall to Nozzle Centerline at Various Slices of the Diverging Section

Figure 15 displays how flow properties vary from the nozzle wall to the centerline at several slices in the diverging section, with velocity in Figure 15a and temperature in Figure 15b. The effects are most evident in Figure 15b, where the fluid temperature is highly affected by the temperature of the nozzle wall nearby. As distance from the wall increases at a given slice in the diverging section, the adiabatic and cooled temperatures become more similar. From Figure 15b, it is observed that cooling influences more than just the boundary layer, and also that cooling effects manifest farther toward the centerline as nozzle length increases.

The difference in velocity profiles in Figure 15a is more subtle, but informative nonetheless. The velocities at the throat through 3/7 diverging length are fairly similar. In slices 4/7 to 6/7, cooling causes a velocity drop from the wall to nearly the centerline, though the velocities at the centerline are still equal. At the nozzle exit, however, even the centerline velocity is compromised. These velocity differences along the radius are consistent with the velocity drop in Figure 13, because the centerline velocity does not drop in Figure 13 until after 6/7 of the diverging length. Leading up to the nozzle exit, Figure13 depicts the same decrease in velocity that Figure 15b shows at the nozzle exit.

Using the flow information both along the centerline (Figure 13) and across the radius (Figure 15), it is observed that the flow is less affected by cooling closer to the centerline. Farther along the nozzle length, however, the flow velocity is increasingly affected until the exit, where even the centerline velocity is compromised slightly.

Figures 16 and 17 are the last piece of the puzzle, and they present the mass-weighted-average of velocity and temperature (respectively) at the same slices in the diverging section presented in Figure 15. From Figure 16, it is observed that the bulk fluid loses 200 m/s due to cooling, which is about a 10% loss. The bulk temperature is even more affected. Figure 17 shows that the bulk temperature drops from 350 K to 225 K, a roughly 35% loss. It seems that the energy loss due to CO_2 cooling

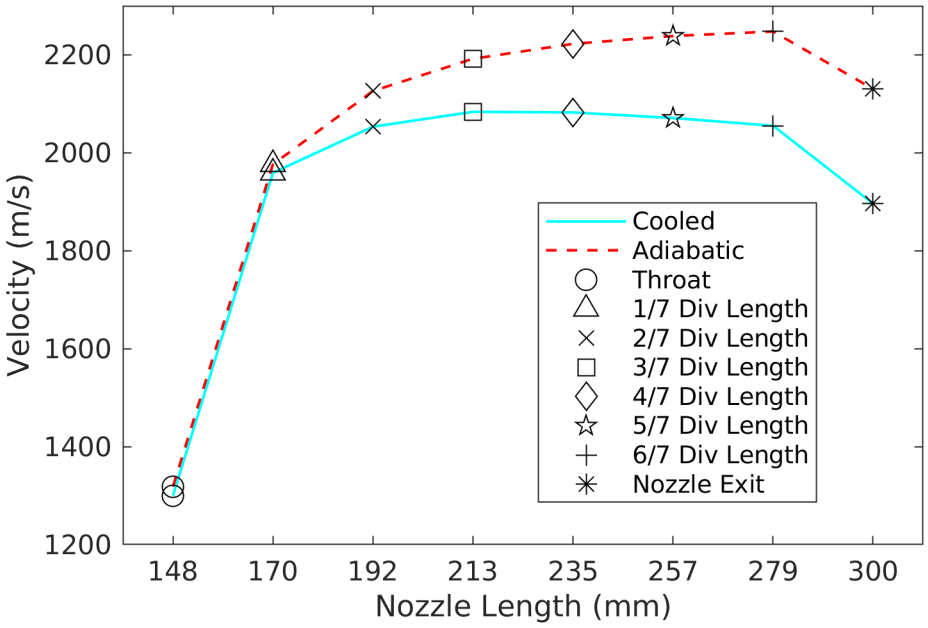

Figure 16: Mass-Weighted Average Velocity at Several Slices in Diverging Section

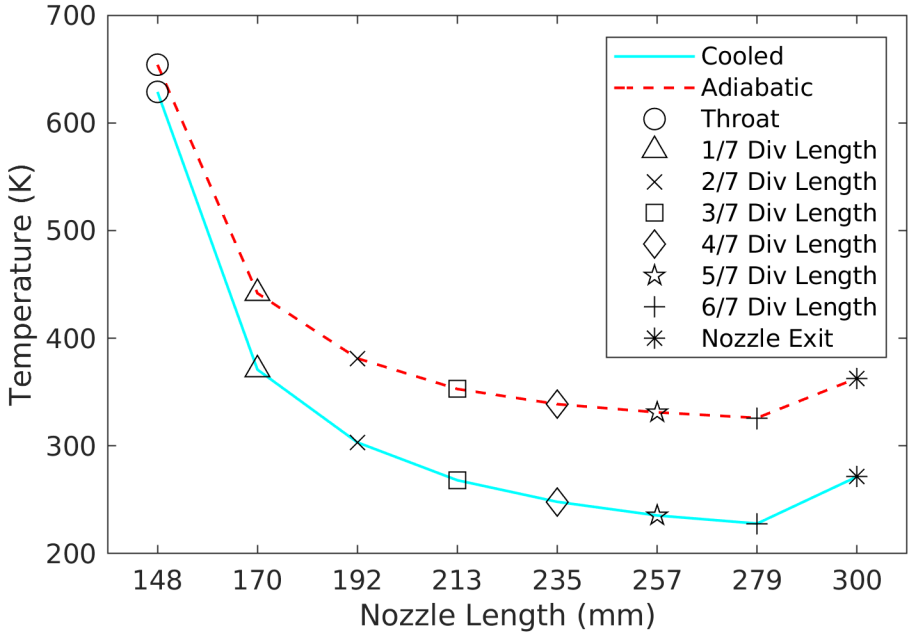

Figure 17: Mass-Weighted Average Temperature at Several Slices in Diverging Section

is so significant that it dominates the compressibility effects otherwise responsible for increased velocity. Even as early as 2/7 diverging length, significant losses are observed. Figure 15 shows that, at locations closer to the throat, these losses occur away from the centerline, but farther along the nozzle length the effects extend farther towards the centerline until the entire cross-section is affected, culminating in a 200 m/s average loss at the nozzle exit.

In light of most literature to date arguing that cooling is not detrimental to the flow [34, 132], these losses due to cooling are larger than expected. The ultimate factor to consider, however, is how the particles are affected by these losses in the driving gas.

1.3.3.5 Particle Behavior

Particle data were collected at the outlet of the nozzle and the substrate so that predictions could be made about particle temperature and velocity upon exit and impact. These data were collected for each of the four inlet conditions considered in the parameter study. The cooled nozzles into which particles were injected were only cooled on dimension O (cooled short), in accordance with the setup of the experiments. Previous studies, although they did not involve nozzle cooling, agree with the general trends in Figure 18 regarding both particle velocity [59, 60, 62, 119] and temperature [62].

It is clear from Figure 18 that the particles coming out of the cooled and adiabatic nozzles have no significant differences in either their temperature or velocity, which shows major promise for cooling as a broadly viable method for clogging prevention. Despite the bulk flow being compromised, the particle data indicate that those flow losses are inconsequential to the particles.

For the smallest particles (5 microns), the particle temperature is *slightly* higher in the cooled case because the gas is hotter in the cooled nozzle's standoff region

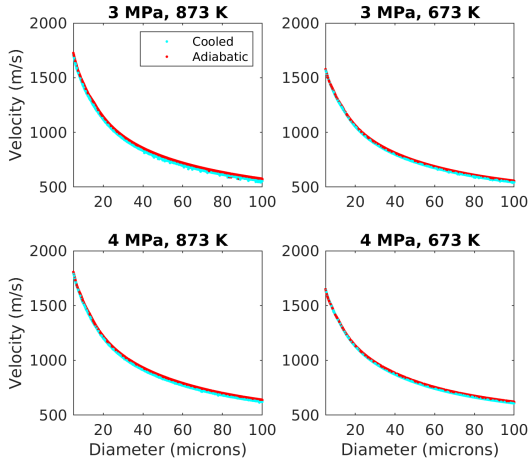

a) Velocity at Nozzle Exit

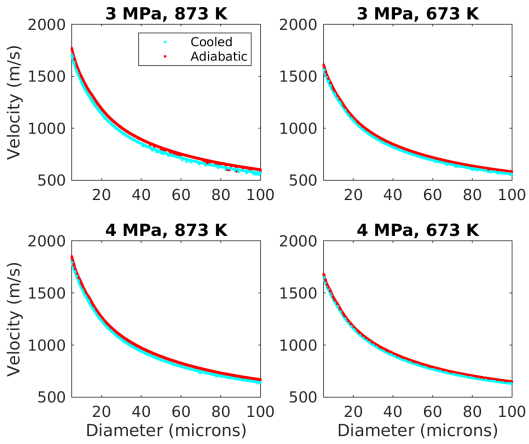

b) Velocity at Substrate

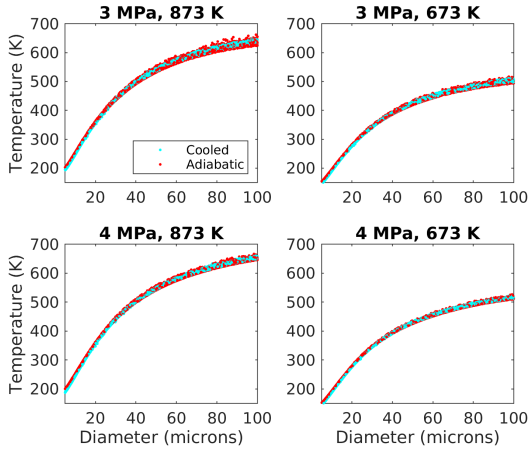

c) Temperature at Nozzle Exit

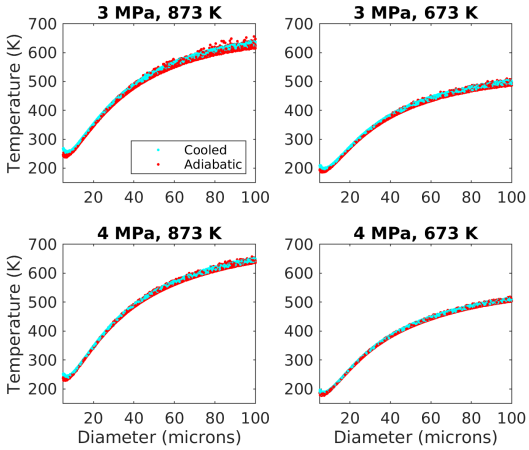

d) Temperature at Substrate

Figure 18: Particle Velocity and Temperature vs Diameter at Nozzle Exit and Substrate

(see Figure 14), but the difference is insignificant. Plus, the concern with nozzle cooling is that particle cooling may occur, but the only particles that are affected experience heating rather than cooling, which can only serve to facilitate adhesion at the temperature range these small particles reach the substrate at. The results in this study indicate that particles are not maligned by nozzle cooling. Experimental confirmation is necessary to prove these particles' resilience, but the models show much promise.

1.4 Conclusion

The present model predicts that neither particle temperature nor velocity is compromised by cooling the nozzle with flashing CO_2, despite the bulk driving gas flow being somewhat compromised. In future work, experiments should be conducted to validate the claim that particles are unaffected by cooling.

A nozzle cooling collar that extends the entire length of the diverging section would probably improve the system's capacity to prevent clogging near the nozzle exit, especially when spraying powders prone to foul in that area, because the nozzle tip temperature increases significantly when left uncooled due to viscous heating inside the boundary layer. It should be noted that the additional span of cooling would likely compromise the flow slightly more than it already is, but since the particles are not significantly affected in the present setup, it is unlikely that one additional inch of cooling at the nozzle tip would cause dramatic changes in particle behavior.

It should also be mentioned that the current cooling device vents the gaseous and solid CO_2 axially, although it would be most advantageous to vent it radially. When the CO_2 is vented axially towards the substrate, the substrate becomes cooled and particle-substrate bonding is jeopardized. The dry ice can damage the substrate, too. When vented axially towards the inlets, the nozzle is cooled unnecessarily in the wrong direction and energy is removed from the hot driving gas at the expense of gas and particle velocity. When the CO_2 is vented radially away from the nozzle and substrate, none of these problems ensue.

CHAPTER 2

SIMULATIONS OF PRESSURE OSCILLATIONS IN FEEDER TUBE

2.1 Motive and Background

This chapter seeks to ascertain a root cause of particle dispersion as a means to better understand the problem of clogging in cold spray. Particle dispersion has been studied in several past works. Lupoi and O'Neill found that, upon exiting the feeder tube, the powder disperses and begins to traverse the entire nozzle volume [72]. Yin et al. built upon the finding of Lupoi and O'Neill by discovering that particles disperse more as feeder tube pressure increases, but only when the feeder tube pressure exceeds that of the applicator [146]. Interestingly, they found when the feeder tube and applicator pressures are equal, particle dispersion is minimal. With a transparent nozzle of square cross-section, Meyer et al. provided the first quantitative measurement of particulate flow inside a cold spray nozzle, and affirmed that dispersion occurs immediately following the injection point [77]. Contrary to Yin et al., they found that dispersion occurs even with equal inlet pressures. Meyer et al. made a distinction between dispersion upstream of the throat and dispersion downstream of the throat, which neither of the aforementioned studies did. They determined that, as inlet pressures increase, particles disperse more upstream of the throat yet focus more downstream of the throat; when inlet pressures decrease, the opposite trend occurs [77]. This fascinating disharmony between Yin et al. and Meyer et al. may be due to the major differences between their nozzle geometries or the fact that Yin et al. conducted their study with high-pressure cold spray while Meyer et al. conducted theirs with low-pressure cold spray.

Despite some disunity, overarching themes can be gleaned. First of all, dispersion begins at the feeder tube exit. Even if it is true that dispersion cannot occur with inlets of equal pressure, it is practically unlikely that both inlets will have perfectly equal pressure during an experiment. It has been found that there are pulsations in the feeder tube during the cold spray process [114], which certainly causes pressure differences between the inlets. Therefore, it can be safely asserted that dispersion occurs to some extent in all cold spray operations and that the dispersion begins at the feeder tube exit.

Second, dispersion is influenced by the magnitude of inlet pressure. Whether it is exacerbated or reduced by increasing inlet pressure seems to depend on nozzle geometry, whether the process occurs in the high or low-pressure regime, or a combination of both factors. Since the present study consists of a high-pressure nozzle with a circular cross-section, it is markedly more similar to the studies of Lupoi and O'Neill [72] and Yin et al. [146] than that of Meyer et al. [77]. Thus in the present study, particles will probably disperse as they did in the studies of Lupoi and O'Neill and Yin et al., with dispersion occurring throughout the whole nozzle [72, 146] and increasing as feeder tube pressure increases [146].

Besides flow conditions at the inlets, the physical features of the feeder tube affect particle dispersion as well. The farther upstream the feeder tube exit is from the throat, dispersion increases. Meyer et al. compared the particle tracks resulting from three injection positions; the injection point farthest from the throat dispersed particles most, while the injection point closest to the throat dispersed particles least [77]. Those results are in complete agreement with the discussions and explanations provided in related studies [72, 112]. Sometimes particles are injected in the supersonic region to minimize dispersion even more, but the drawback of that method is particles are not entrained in the fluid streamline as long, and thus their ability to reach critical velocity is jeopardized [72, 112]. Another disadvantage to injecting par-

ticles in the supersonic region is that they do not undergo as much heating since the particles bypass the hot prechamber, which otherwise would have favorably heated them. Without particle heating giving rise to particle softening, impingement on the substrate is further threatened [112]. In general, particles injected in the supersonic region are slower and colder than those injected upstream [49].

Despite these complications, copper (a clogging-prone material) can be deposited by means of a diverging section injection [85]. Other clogging-prone powders, however, like titanium and stainless steel, demand more severe bonding conditions and consequently cannot be deposited with such a method [112]. In particular, the critical velocity of copper is considerably lower than those of titanium and steel [104]. Alternative methods are therefore necessary for depositing clogging-prone powders like titanium and steel.

An excessive feeder tube inner diameter promotes clogging too. Lupoi and O'Neill's work strongly suggests that smaller injector tubes produce narrower particle beams while larger ones facilitate greater dispersion [72]. Ozdemir and Widener confirmed with their CFD simulations that a large feeder tube provokes particle dispersion and therefore clogging [87]. This observation can be realized by considering a particle with (theoretically) zero radial velocity and a large radial position. Since the feeder tube is large, a particle can have a large radial position, which prepares it to miss the throat and collide with the converging wall even if its motion is exclusively axial. Upon colliding, the particle will rebound with significant radial velocity into the supersonic region, at risk of bonding with the diverging wall since it travels at critical velocity there. A smaller feeder tube would inhibit a (theoretical) particle with exclusively axial velocity from dispersing because the particle would not collide with the walls; it would travel unhindered through the nozzle. Of course, a particle with zero radial velocity is an idealized condition, and there are more phenomena at play than simply

feeder tube size, but it is significant that feeder tube inner diameter plays a role in particle dispersion.

Relatedly, Ozdemir and Widener studied the effects of feeder tube misalignment with the centerline and found that it causes particles to disperse in the direction that the misalignment manifests. Their results confirmed those of a previous study likewise incorporating a feeder tube misalignment [44]. When particles are directed by the feeder tube towards the nozzle wall, they are more inclined to collide with it and maintain radial velocities into the diverging section.

The nozzle's inner cross-sectional shape also determines how much particles will disperse. Tabbara et al.'s simulations show that an elliptical internal cross-section causes particle dispersion, especially along the ellipse's minor axis [118]. They found too that circular and square cross-sections produce more focused particle beams than an elliptical one. Meyer et al. used a nozzle with rectangular cross-section [77], while Lupoi and O'Neill [72] and Yin et al. [146] both used nozzles with circular cross-sections. The present study is based on a nozzle with circular cross-section as well, which is advantageous for minimizing dispersion.

Further related to nozzle geometry are the nozzle dimensions. Lupoi and O'Neill [72] compared the particle dispersion in four nozzle configurations, two of which incorporated the same inlet pressure, injector exit location, and injector inner diameter. The features that varied between those two configurations were throat diameter, annulus diameter, exit diameter, converging length, diverging length, and standoff distance. Indeed, the level of dispersion differed between the configurations, but it is difficult to isolate which of these dimensions played the largest role in dispersing the particles. At the very least, it must be recognized that some nozzle dimensions (or combinations of dimensions) provoke particles to disperse more than others.

Examining beyond nozzle geometry, there are still more factors that contribute to particle dispersion. Particle size and mass play a role, but there is fascinating

Table 4: References Describing Particle Size/Mass-Dependent Dispersion

Author	Which Particles Disperse Most?	Particle Diam (μm)	Feeder Tube Temp (K)
Wang et al. [132]	small	5-50	873
Tabbara et al. [118]	small	5-30	N/A
Samareh and Dolatabadi [102]	small	5-60	N/A
Zahiri et al. [151]	small	8-80	N/A
Meyer et al. [77]	lighter	10-60	N/A
Lupoi and O'Neill [72]	large	10-32	293
Foelsche (present study)	generally small, but large outliers	5-100	673

Author	Feeder Tube Pres (MPa)	Annulus Temp (K)	Annulus Pres (MPa)
Wang et al. [132]	2.5	873	2.5
Tabbara et al. [118]	N/A	298	2.9-3.0
Samareh and Dolatabadi [102]	N/A	773	0.62
Zahiri et al. [151]	N/A	823-1073	1.4-3.0
Meyer et al. [77]	N/A	293	0.34-0.90
Lupoi and O'Neill [72]	3.4	293	3.0
Foelsche (present study)	4.0	673	4.0

disagreement as to whether smaller particles disperse more than larger ones or vice versa. Table 4 summarizes the studies which make claims about the topic. Apart from the present study, Lupoi and O'Neill [72] are the only group concluding that large particles disperse most. It is highly unlikely that their result is an anomaly related to nozzle geometry because they obtained the same result for all four of their geometric configurations. Neither are their results dependent on injection location because two of their configurations incorporated subsonic injections while their other two incorporated supersonic injections.

It is challenging to diagnose why such a disagreement is found between these studies, but there are some plausible explanations. The studies that analyzed dispersion solely with modeling were Wang et al. [132], Tabbara et al. [118], Samareh and Dolatabadi [102], Zahiri et al. [151] and Faizan-Ur-Rab et al. [25] (whose respective works are part of the same study), and the present work. The two studies that com-

pared their results with experiments were Meyer et al. [77] and Lupoi and O'Neill [72]. Meyer et al. found from their experiments that lighter materials disperse more than those that are more dense.

For the purposes of the present study, Meyer et al.'s conclusion should be distinguished from the others because they did not comment on which particle sizes disperse more when all particles are the same material. It is necessary in the present study to distinguish between particle size and density because if lighter materials disperse more than heavier ones, it does not necessarily follow that small particles disperse more than large ones of the same material. Nevertheless, their results are relevant and included in Table 4.

Meyer and Lupoi did comment explicitly on particle size and compared the predicted particle footprint from their models to their experimentally deposited track width on the substrate. Both their models and experiments indicated that, although their footprint was a certain size, the bulk of the particles were much more focused within a narrower range.

Understanding that most particles fall within a narrower range may be the key to understanding the apparent disagreement between the studies provided in Table 4. The present study finds that when particles are injected with exclusively axial velocity, the small particles do generally disperse slightly more than the large ones. There are, however, several outlier particles, all of which are large, located much farther away from the centerline than the farthest small particles. These highly dispersed large particles are the minority, but it may reconcile Lupoi and O'Neill's results to all the others. Faizan-Ur-Rab et al.'s results contribute to this theory, indicating that large particles may be most prone to being outliers in terms of having large radial positions. Faizan-Ur-Rab et al. likewise determine that the bulk of small particles focus more than that of medium particles, and that the bulk of medium particles focus more than that of large particles.

In the present study, when particles are injected from the feeder tube with angled trajectories, the smallest particles are found to be much more focused than the larger ones, with dispersion increasing as particle size increases. This is probably due to large particles colliding at steep angles with the feeder tube and nozzle wall, and the fluid being incapable of coercing them fully axially due to their large inertia. The smallest particles are more influenced by the flow and are thus more prone to move axially rather than radially.

It is noteworthy that four of the studies summarized in Table 4 neglect to incorporate and describe a feeder tube wall in their models. Those studies, with "N/A" under their feeder tube properties, either injected particles via an artificial surface in the nozzle [118], a projected surface on the nozzle wall [102], a simple injection point [25, 151], or did not describe and present how the particles were injected and how they interacted with the feeder tube in their models [77]. It is unclear whether Meyer et al. [77] incorporated the feeder tube wall in their models.

Including the present study, Table 4 describes three studies that do incorporate a feeder tube wall in their models. Of those three studies, Wang et al. is the only work that concludes small particles disperse more than large ones. Since the present study finds that large highly dispersed particles only make up 0.072% of the total injected number of particles, it could be that Wang et al. do not inject enough particles in their simulations to obtain these outliers. They do not mention how many particles were injected in their simulations. It could be that the incorporation of a feeder tube wall in CFD models (which is evidently atypical of dispersion studies in cold spray) allows large particles to collide with that wall far enough upstream that those few large particles obtain significant radial velocities and maintain them throughout their trajectories. Ozdemir and Widener fully account for a feeder tube wall in their particle dispersion study, but they do not comment on which particle sizes are most prone to disperse [87].

All the modeling studies that do not fully account for a feeder tube wall determine that large particles disperse less than small ones. This may be because those large particles are not colliding with the feeder tube in their models, and therefore never obtain significant radial velocities. As an attempt to glean common ground, it seems generally true that small particles disperse more than large ones, but large outlier particles occasionally disperse more than the small ones. With the information available though, it is difficult to clearly discern the reason for the disagreement without overanalyzing.

Nonspherical powder morphologies can cause increased dispersion since the lift force is greater for irregularly shaped particles than it is for spherical ones [68]. The fact that irregularly shaped particles are faster is well-attested in cold spray [76, 139]. For that reason, it is especially detrimental to employ nonspherical clogging-prone powders because they will not only greatly disperse due to high lift forces, but they will also disperse at unconventionally high velocities, increasing the likelihood that they will impact the nozzle wall at speeds sufficient for bonding. In numerical studies on particle tracks in cold spray, the particles are almost always assumed to be spherical [26, 72, 146], which is the assumption in the present work as well. Otherwise, the surface forces on the particle become quite complex [20]. Bhattacharya et al. suggest that typical cold spray particle sizes (5-100 microns) are quite susceptible to lift forces [9]. Numerical studies may be underpredicting particle dispersion in cases with irregular powder morphologies by modeling particles as perfect spheres.

Additionally, the driving gas material can facilitate dispersion. Tabbara et al. found that helium disperses particles more than nitrogen does, which they attributed to higher levels of turbulence in the helium flow, induced by higher velocity gradients [118]. This is an unfortunate finding in terms of clogging prevention because helium is often used with clogging-prone powders instead of nitrogen so that critical velocity can be reached without making the nozzle and particles too hot. The fact that helium,

the driving gas often required for spraying clogging-prone powders, tends to disperse particles more means that helium-driven particles have an increased likelihood of contacting the nozzle wall. Ideally, clogging-prone powders should avoid contacting the nozzle wall because of their inclination to bond upon impact. The inconvenience is worth noting, but nitrogen is incapable of spraying many clogging-prone powders in the first place, so helium is nonetheless the superior driving gas.

Also related to the driving gas is turbulence, which is often considered a major reason for dispersion in cold spray. Lupoi and O'Neill [72] and Yin et al. [146] both found local peaks in turbulence kinetic energy (TKE) at the throat, and concluded that the turbulence in that region contributes to dispersion as particles enter the diverging section. Their TKE results are provided in Figure 19.

The TKE from Yin et al.'s nozzle (presented in Figure 19b) is higher than that of Lupoi and O'Neill's nozzle (presented in Figure 19a) by roughly a factor of 20. One explanation for such a significant disagreement is the temperature difference between the inlets of both studies. Yin et al.'s annulus inlet was set to 873 K while their feeder

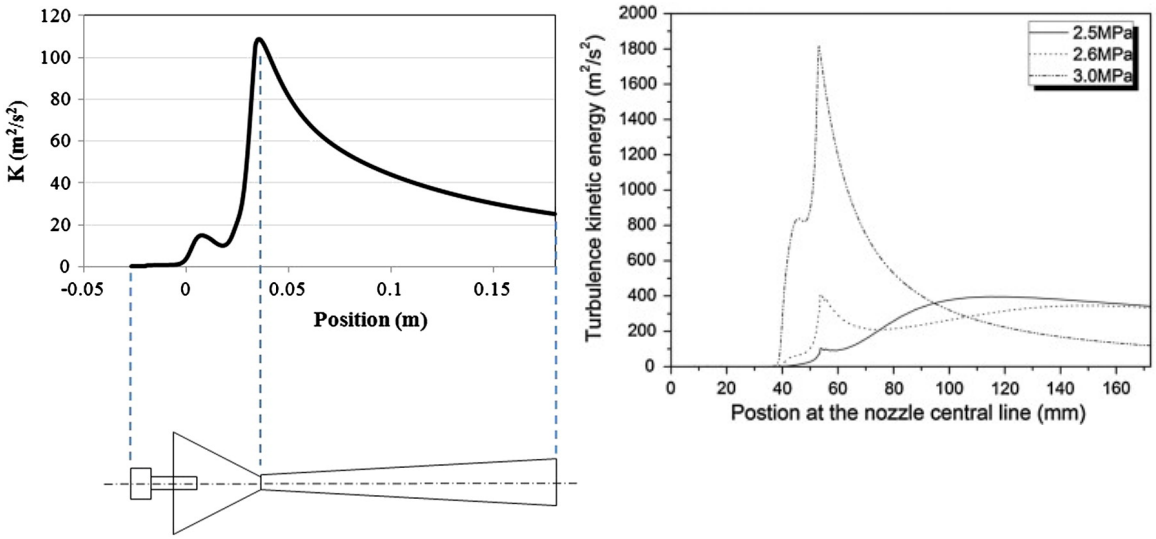

a) TKE form Lupoi and O'Neill [72]

b) TKE from Yin et al. [146]

Figure 19: Turbulent Kinetic Energy vs. Nozzle Length from Two Sources

tube inlet was 298 K. Lupoi and O'Neill, on the other hand, modeled both inlets at room temperature. Because high gas temperatures result in higher flow velocities, Yin et al. are bound to obtain more TKE because there is a large difference in flow velocity between their inlets. When the two gas streams merge, their velocity difference produces increased shear levels and therefore increased turbulence.

Yin et al. pointed out that, in particular, the turbulence inside the prechamber, converging section, and at the throat has a major impact on particle trajectories because the particles have yet to build much momentum, and consequently their trajectories are easily manipulated before their major momentum increase in the supersonic region. Turbulence in the supersonic region, though it may be high in some configurations, does not contribute so much to dispersion because the particle trajectories are less thwarted due to their high momentum. Computationally, turbulent dispersion is accounted for by amending particle tracks via stochastic methods [43]. For comparison, Lupoi and O'Neill conducted a simulation where they did not account for turbulence in the formulation of their particle tracks, and found that particle beam width was reduced by 42%. Their comparison indicates that turbulence greatly influences particle dispersion.

There is, however, some work both in and out of the field of cold spray arguing that turbulence plays a negligible role in particle dispersion. Meyer et al. claim, in their cold spray study using metal particles of similar sizes as those aforementioned, that particles are not primarily affected by turbulent fluctuations due to high inertia [77]. They cite a more general study on particle motion in turbulent jets (with glass particles of diameter 37-255 microns) by Hardalupas et al. [36], who concluded similarly.

It should be acknowledged, however, that those findings by Hardalupas et al. were general conclusions, and that their smaller particles actually were found to be influenced non-negligibly by turbulence. It was their larger particles that were un-

responsive to turbulent fluctuations. Considering the hypothesis that smaller particles are generally dispersed more than large ones in cold spray, Hardalupas et al.'s size-specific conclusions seem to align with the discussions found in most cold spray literature claiming turbulence to have a significant effect on dispersion: the smaller particles are dispersed more due (partially) to turbulence while the larger ones are dispersed less because they are less affected by turbulence.

Meyer et al. determine that dispersion occurs largely because of particles rebounding after collisions (among other factors), and that particle inertia is too great for them to respond to turbulent fluctuations. Their work is a great contribution because they thoroughly investigate many factors responsible for dispersion, but it seems they underplay the role of turbulence, especially in light of Lupoi and O'Neill's CFD results producing a 42% reduced particle beam width when turbulence was unaccounted for.

Admittedly, there is no way to experimentally validate Lupoi and O'Neill's comparative simulations, because turbulence cannot be withdrawn from a cold spray nozzle. Even so, turbulence models are regularly validated against experiments [151], giving them some level of credibility. Of course, it does not follow that because turbulence models are validated experimentally that they perfectly model the effects of turbulent fluctuations on particle trajectories, but it does follow that the findings from Lupoi and O'Neill's turbulence study can be accepted with some generality: turbulence causes particle dispersion.

Inlet pressures, feeder tube location and size and misalignment, nozzle geometry and cross-sectional shape, particle size and mass, powder morphology, driving gas material, and turbulent fluctuations are all known to play a role in dispersing particles. The present chapter hypothesizes yet another root cause of dispersion and clogging in cold spray nozzles: flow oscillations in the feeder tube. Pulsations in the particle jet inside the particle injector have been identified by Sova et al. [114] and were considered to be the cause of clogging in their experiments. The claim that such

pulsations lead to clogging was not investigated, but such an investigation is carried out in this study. This CFD work is based on specific cold spray experiments by Siopis et al. that report nozzle clogging [109], but the present models could not predict sufficient dispersion for clogging without imposing flow oscillations in the feeder tube.

The present study seeks to determine whether flow oscillations in the feeder tube, if present, can cause clogging. Several CFD simulations were conducted to isolate the effects of imposed transient pressure fluctuations on particle dispersion and bonding.

Upon cutting open their nozzle, Siopis et al. identified specific clogging regions in the diverging section, which depended on how much the powders were sieved. Their clogging regions are illustrated in Figure 20.

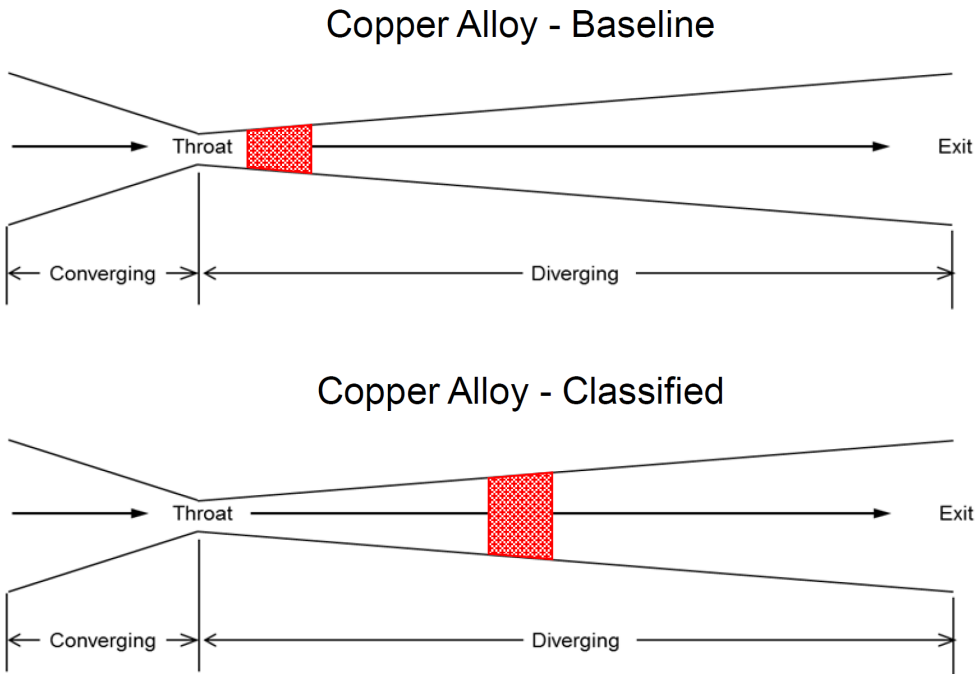

Figure 20: Location of Clog Found in Nozzles from Experiments [109]
Top: Clogging Location with Powder as Received.
Bottom: Clogging Location with Powder Classified to Remove Fines.

2.2 Modeling Methodology

2.2.1 Boundary Conditions

As was the case in the first chapter, a 2-D axisymmetric assumption was used for these simulations. Only the flow domain was solved in this chapter, the dimensions of which are presented in Figure 21. All the walls depicted in Figure 21 were given the no-slip condition. These walls were set to reflect particles in the event of a particle-wall collision, the only exception being at the substrate wall, which was set to terminate the particle trajectory in the event of a collision. Particle trajectories were also terminated upon contacting the outlet, depicted in green in Figure 21. The inlets, depicted in red, were set to reflect particles so that instances of backflow would not cause the particles to leave the domain.

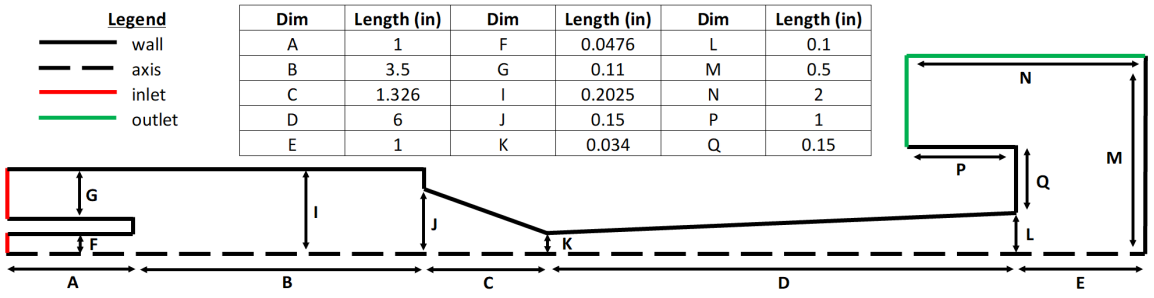

Dim	Length (in)	Dim	Length (in)	Dim	Length (in)
A	1	F	0.0476	L	0.1
B	3.5	G	0.11	M	0.5
C	1.326	I	0.2025	N	2
D	6	J	0.15	P	1
E	1	K	0.034	Q	0.15

Figure 21: Nozzle Geometry (Flow Domain)

To test the hypothesis that transient feeder tube fluctuations are a cause of particle dispersion, three types of simulations were run. First, a completely steady-state calculation was performed. Second, a transient calculation was performed, but with constant inflow boundary conditions. Finally, nine transient calculations were performed with a time-varying pressure at the feeder tube inlet with three different pressure wave amplitudes and three wave frequencies to isolate the respective effects that wave amplitude and frequency have on particle dispersion and bonding.

Boundary conditions at the inlets were fixed at a pressure of 4 MPa for the steady-state simulation along with the transient case with constant inflow conditions. All

simulations were solved with 673 K inlets. These inlet conditions are consistent with those of Siopis et al.'s experiments. To simulate the nine different pressure fluctuations in the feeder tube inlet, the inlet total pressure was changed to a custom user-defined function (UDF), which imposed a pressure that varied sinusoidally with time according to the equation 12:

$$P = P_{ave} + P_{amplitude} sin(2\pi\omega t) \tag{12}$$

In equation 12, the average pressure P_{avg} was maintained at 4 MPa. Three values for $P_{amplitude}$ were modeled, along with three values for ω. The amplitudes ($P_{amplitude}$) considered were 50 kPa, 25 kPa, and 10 kPa, and the frequencies (ω) considered were 25 Hz, 50 Hz, and 100 Hz. These amplitudes and frequencies were not experimentally measured, rather, they were selected to give a sufficient range that conclusions could be made about the respective effects of frequency and amplitude on particle dispersion. The pressure outlet, depicted in green in Figure 21, was set to atmospheric conditions (zero gauge pressure and 300 K).

2.2.2 Mesh Description

A mesh dependence study was conducted by solving a steady-state solution with several meshes ranging from 2,500 to 135,000 cells and comparing the differences in flow properties. It was found that the meshes containing 51,000 cells or more did

Table 5: Mesh Specifications Based on Zone Name for Pressure Oscillation Simulations

Zone	Cell Size (mm)
inlets	0.2
prechamber	0.2
converging	0.2
diverging	0.1
standoff	0.4
atmosphere	0.4

not produce substantially different results, so the mesh of 51,000 cells was used. Five layers of relatively thin elements were incorporated near the wall, with most wall yplus values falling inside the range of 5 to 70, the maximum occurring at the throat. The specific details of the mesh based on zone name are provided in Table 5.

2.2.3 Gas Phase Modeling

The density-based implicit solver was used with the first-order upwind spatial discretization scheme because the flow is supersonic, and a sufficient level of convergence was desired. As was the case in Siopis et al.'s experiments [109], the fluid used in these simulations was helium, and its density varied with the ideal gas law. The helium viscosity and thermal conductivity were kept constant in this study.

Several turbulence models were tried and considered with the present mesh by solving a steady-state solution with them. After comparison, the k-ϵ realizable turbulence model with standard wall functions was deemed most appropriate because it provided the most physically likely results for axial TKE with a peak in the throat, similar to Lupoi and O'Neill [72] and Yin et al. [146].

2.2.4 Discrete Phase Modeling

As was the case in the previous chapter, the Discrete Phase Model with Lagrangian one-way coupling was used to track the particles and the Discrete Random Walk model was incorporated to stochastically account for turbulent fluctuations. The particles were one-way coupled to the fluid such that particle motion was affected by the fluid motion, but not vice versa.

There is disagreement amongst cold spray studies as to whether particles interact with the fluid or each other in such a way that their trajectories and velocities are affected. Though not unanimously, it is widely assumed in cold spray studies that, if the volume fraction of particles to driving gas is less than 10%, two-way coupling effects are negligible [106]. Taylor et al. argued that, when high powder feed rates

are used, the reason for poor deposits is not because of flow saturation with particles, but rather from excessive particle bombardment on the substrate [120].

Alternatively, Samareh et al. concluded that two-way coupling effects significantly influence particle motion [103], even at the same powder feed rates as Taylor et al. Lupoi [71] and Meyer et al.'s [79] results suggest that two-way coupling effects caused noteworthy differences in particle behavior, which motivated another study by Meyer et al. [77] in which they argue that both fluid-particle and particle-particle interactions affect the velocities of both the driving gas and the particles. They also asserted that particle dispersion is aggravated by particle-particle collisions.

It can be complicated to determine when two-way and four-way coupling ought to be accounted for [126], and even if Meyer et al. [77] are correct in claiming that both fluid-particle and particle-particle collisions influence flow velocity, particle velocity, and particle dispersion, it would be unreasonable to incorporate such effects in the present study. Since the experiments by Siopis et al. [109] used a powder feed rate of 14 g/min, in order to properly model the number of particles per pass of the feed holes in the metering wheel, roughly 600 particles should be injected per injection (see section 3.2.4 for the rationale behind this claim). Because particle-wall bonding is such a low-probability event, it is insufficient to only model 600 particles per injection because it gives too small a sample size to collect meaningful particle behavior data unless the simulation wall time is impractically long. In each of the nine oscillatory simulations in the present study, ten injections spanned across 0.04 seconds, consisting of 50,000 particles each, providing 500,000 total particles injected per simulation. If the particles and fluid were two-way coupled in the present models, the effect of particles on the fluid would be dramatically overpredicted because there are 83 times more particles in each injection than there were in the experiments. It is vain to simultaneously account for two-way coupling and a large sample size of particles because the two-way coupling effects will be exaggerated beyond what

is realistic. The steady-state model incorporated only one injection with 500,000 particles so that clear comparisons based on equal total sample size could be made between the particles of all simulations in this chapter. The governing equations for particle motion and heat transfer are the same in this chapter as they were in the previous one, those being equations 7 - 10.

To predict clogging with these CFD models, bonding must be predicted. An approximation for critical velocity is provided by Schmidt et al. [104] and simplified by Siopis et al. [109], which is implemented in this study for the sake of predicting particle-wall bonding in the nozzle. If a particle impacts the wall at a velocity greater than or equal to its critical velocity, it will adhere, but if it collides at a subcritical velocity, it will reflect and continue on its trajectory. The critical velocity equation is provided in equation 13:

$$v_{crit} = \sqrt{\frac{4F_1\sigma_{TS}\left(1 - \frac{T_i}{T_m}\right)}{\rho} + F_2 c_p\left(T_m - T_i\right)} \tag{13}$$

where F_1 and F_2 are emperical factors (1.2 and 0.3, respectively).

The critical velocity ratio is defined in Schmidt et al.'s work as the particle impact velocity divided by the particle critical velocity:

$$CVR = \frac{v_{impact}}{v_{crit}} \tag{14}$$

A CVR ≥ 1 means that the particle impact velocity is greater than or equal to the critical velocity required for bonding, and indicates that the particle bonds to the wall. In theory, the v_{impact} term in equation 14 should be the component of velocity normal to the wall, which is assumed to be smooth in these models. When the normal component of v_{impact} was used in the present models, however, no bonding was predicted. Bonding was successfully predicted when the magnitude of v_{impact} was used for the bonding criteria.

Realistically, on the length scale of one particle diameter, the nozzle wall is probably rough, which may justify using the impact velocity magnitude rather than its unit normal. Because of wall roughness, it seems likely that most collisions are not occurring at shallow angles, but rather at angles closer to 90°. It was therefore assumed in this study that any collision with the wall was a head-on collision regardless of trajectory, and therefore the velocity magnitude was used for the v_{impact} term.

Even if the impact angle is significantly shallower than 90°, Nardi et al. [82] point out that such impact angles can produce higher bond strength deposits than those produced at 90°, so using the magnitude of velocity rather than the normal component may more accurately model a bond occurring at a steep angle. If a particle collided with the nozzle wall at subcritical velocity, the normal and tangential coefficients of restitution used to calculate its rebound velocity were 0.8 and 0.7, respectively.

It should be noted that the numerous phenomena at play during particle-wall interactions (bonding and rebounding) inside the nozzle are not fully known, and the employment of several simplifying assumptions is inevitable when modeling such interactions. Future work should be dedicated to studying impact phenomena, wettability, and tribochemistry between the particles and the nozzle wall.

To gather information about the particle-wall collisions inside the nozzle, a UDF was implemented as a custom boundary condition on all nozzle walls except the feeder tube, namely, the prechamber wall, the "step" between the prechamber and converging wall, the converging wall, and the diverging wall. This UDF recorded the axial position, particle diameter, and bonding CVR of each particle-wall collision. The data from this UDF were used to determine which particles bonded or rebounded, with what diameter, and at what location in the nozzle. Particles that collided with a CVR ≥ 1 were terminated and no longer tracked.

In their experiments, Siopis et al. sprayed a copper-nickel alloy (38% wt Ni + 62% wt Cu) with diameters that ranged between roughly 5-45 microns [109]. The powder

material was modeled with a density of 8940 kg/m^3 and a specific heat capacity of 380 J/kg-K. In each injection in this chapter, particles were generated uniformly randomly with diameters between 5 and 50 microns so that conclusions could be made about bonding based on diameter, rather than to be realistic.

Like in chapter one, each injection was modeled by generating particles randomly to fill the whole feeder tube volume. This was achieved by increasing the likelihood for particles to generate away from the centerline by a factor of the square root of radial position. Since the 2-D axisymmetric assumption was used, the particle location density needed to be uniform as if the particles occupied a 3-D space. Particles were injected at room temperature (300 K) with zero initial velocity in the feeder tube.

2.3 Results

2.3.1 Steady-State Model

Contours of the helium gas flow were obtained from the steady-state model to comprehend the flow characteristics inside the nozzle, which are presented in Figure 22. As expected, the velocity near the inlet is low while the temperature and pressure are high. The velocity increases towards the throat and continues to increase supersonically until the outlet, after which point the flow decelerates to zero at the substrate. Small Mach diamonds are observed just outside of the nozzle exit, and a bow shock is observed just upstream of the substrate because the supersonic compressible flow is decelerating to subsonic velocity. Once the fluid contacts the substrate, it disperses radially into the atmosphere at low velocity. In the diverging section within the boundary layer, a lower velocity is observed which is due to the no-slip condition on the nozzle wall.

Not surprisingly, the pressure starts high and smoothly decreases as the flow moves from the inlets to the outlet, while the temperature decreases in proportion

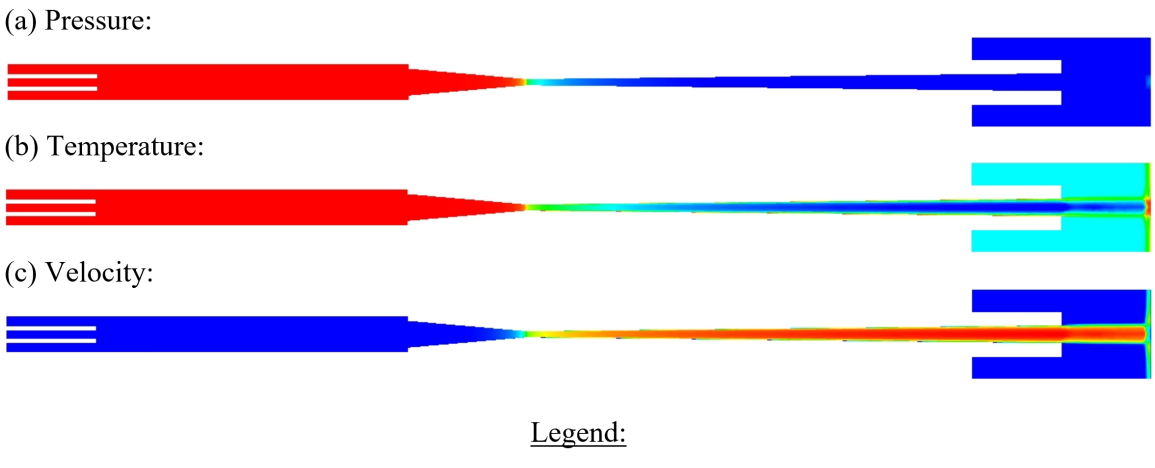

Figure 22: Steady-State Contours

to the increase in velocity. The temperature in the boundary layer is relatively high compared to that of the bulk fluid because of viscous heating in that region.

The particle pathlines for the steady-state solution are provided in Figure 23, where particles are observed to start at a low velocity and build momentum throughout the length of the nozzle. The particle beam width increases in the prechamber until some particles collide with the converging wall and begin their supersonic journey down the diverging section. The beam width narrows at the throat because all the particles must squeeze through that small orifice, and continues to be narrow in the diverging section until the particles reach the substrate.

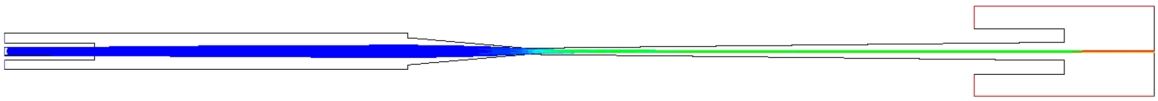

Figure 23: Steady-State Particle Pathlines - Low to High Velocity (Blue to Red). Range from 0 to 1700 m/s.

The particle-wall collisions from this steady-state solution are presented in Figure 24, where it is observed that all collisions in the nozzle occur prior to the throat and

at CVRs below one (indicative of no bonding). The particles have been grouped by size in this figure to show the consistent behavior that smaller particles attain higher velocities. This phenomenon occurs because, as the particles build momentum down the nozzle, their velocities increase according to their mass. Since it is known that the present configuration clogs in the diverging section (see Figure 20), it is determined that the steady-state model does not properly account for all the physics responsible for particle dispersion in the diverging section because it predicts no clogging while the experiments do result in clogging.

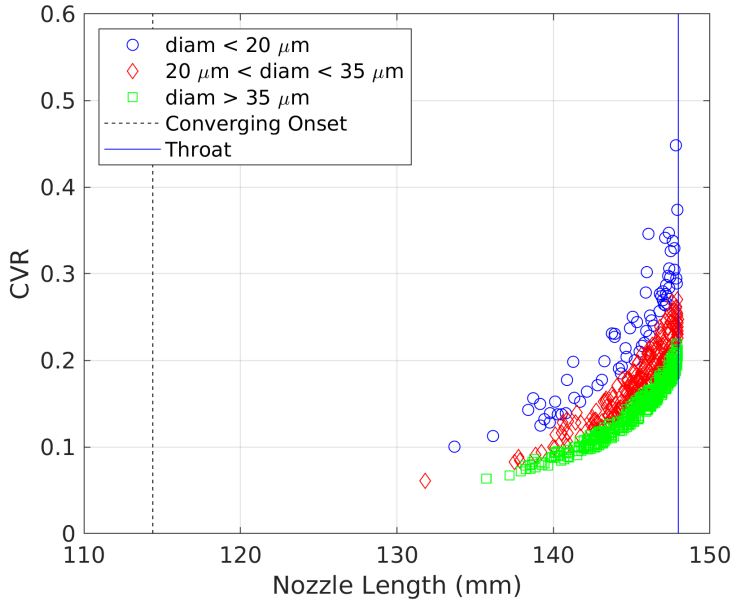

Figure 24: Steady-State Particle-Wall Collisions

Figure 25a shows the axial TKE in the nozzle modeled in this study, where a peak at the throat similar to the results in Figure 19 is observed. Figure 25b shows how the TKE varies radially in the nozzle and confirms a maximum value at the throat. There is much more turbulence near the wall than on the centerline, and several orders of magnitude more in the throat at the wall than in the throat on the centerline. This means that, when particles collide with the wall in the converging section near the throat, in situations like Figure 24 describes, they experience extreme turbulence that

can send them towards the wall in the diverging section, where clogging occurs. It also means that as particles begin to disperse radially, they enter areas with more and more turbulence, continually giving them a greater chance of being pushed toward the wall.

The high values of turbulence in the steady-state solution both at the throat and near the walls, however, do not seem to be the primary cause of particle dispersion because, as Figure 24 demonstrates, there are zero particle-wall collisions downstream of the throat in this model. Although large values of turbulence at the throat contribute to dispersion, there is apparently more physics to be accounted for than the steady-state model provides if the full effect of dispersion is to be observed.

The peak in Figure 25a is smaller than both TKE peaks in Figure 19. Because this study incorporates inlets of equal temperature and pressure, the peak is much lower in this study than it is for Yin et al. (see Figure 19b), who modeled different temperature inlets. Since both the present study and that of Lupoi and O'Neill incorporated inlets of equal temperatures, the TKE values are similar (see Figure 19a). A possible explanation for the TKE peak in the present study being slightly lower than that of Lupoi and O'Neill could be that the nozzle geometry in the present

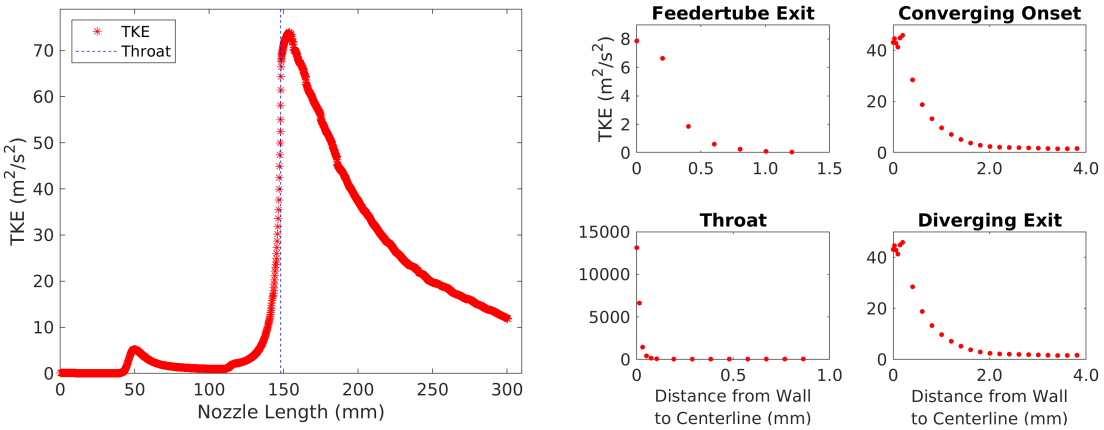

a) Turbulent Kinetic Energy vs Nozzle Length

b) Radial TKE at Four Locations

Figure 25: Turbulent Kinetic Energy in Nozzle - Axial and Radial

study has a long prechamber, whereas the geometry in Lupoi and O'Neill's study does not have a prechamber at all. Their injection takes place in the converging section. A long prechamber may minimize turbulence near the throat because the flow has more time to stabilize after the mixing of the two inlet gas streams. Without a prechamber, the two gas streams are still not fully mixed by the time they arrive at the throat, which may cause higher levels of turbulence.

Turbulence being accounted for, there are several other features in the present configuration that are also known factors for dispersion and clogging. The injection point is relatively far upstream from the throat, giving the particles ample time to spread apart. Furthermore, as seen in Figure 21, the injector tube is wider than the throat, which sets particles up to collide with the converging wall. Concerning particle size, regardless of whether small or large particles tend to disperse more, the present study injects a wide range of particle sizes, so the dispersing-prone sizes are certainly employed, whatever they are. Helium is the driving gas in the present study, and although it disperses particles more than nitrogen does, helium is required to spray many clogging-prone powder materials, so using helium is unavoidable.

One characteristic of the present model that may have contributed to underpredicting dispersion is the assumption of spherical particles. The powder morphology was not photographed, so it is uncertain if the experiments employed irregular particle shapes that would be particularly prone to disperse into the nozzle wall. Even if the powder morphology was nonspherical though, it is unlikely that this assumption alone would cause such a major underprediction of dispersion, because other numerical studies employ the same assumption and do predict dispersion and clogging [87].

There are also features in the present configuration that favorably minimize dispersion. Particles are less prone to disperse when the feeder tube and annulus employ equal pressures, which is the case in this study. This may explain why the steady-state model underpredicts dispersion compared to experiments, because it incorpo-

rates perfectly equal inlet pressures, whereas an experiment would have pulsations in the feeder tube [114]. Regarding nozzle geometry, the feeder tube is properly aligned in the present model, and there is no reason to believe that it was situated otherwise in the experiments. The circular cross-section of the present nozzle is favorable for minimizing dispersion compared to other shapes, too. Although these features discourage dispersion, according to Siopis et al.'s experiments, clogging still occurs in the present configuration. All features of the present configuration considered, dispersion is insufficiently predicted with the steady-state model.

2.3.2 Transient Model with Constant Pressure in Feeder Tube

In this second simulation, the first-order implicit transient formulation was used with constant pressure inlets set to 4 MPa. This simulation was conducted to determine whether the physics responsible for particle dispersion is present in a transient model while maintaining constant inflow conditions.

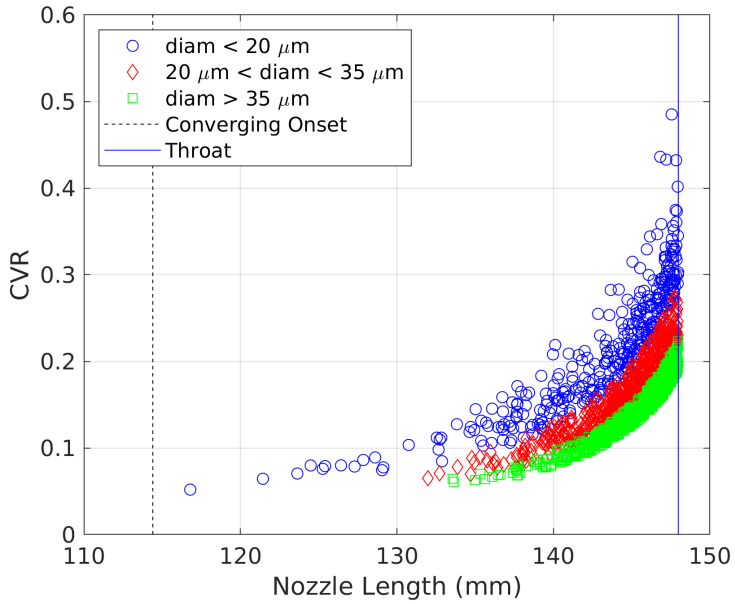

Figure 26: Transient Particle-Wall Collisions at Constant Inflow

Once the solution progressed sufficiently that the initial transient noise subsided and the inlet pressure settled to 4 MPa, the 500,000 particles were injected incremen-

tally in groups of 50,000 to simulate a stream of particles entering the injector tube. Figure 26 shows the resulting particle-wall collisions, and the results are similar to those of the steady-state simulation – collisions exclusively occur prior to the nozzle throat and at CVRs less than one. It is thus concluded that a transient simulation with constant inlet pressures cannot predict the realistic particle dispersion that leads to clogging in the diverging section, and that transient simulations with fluctuating inlet pressures should be investigated.

2.3.3 Transient Model with Pressure Fluctuations in Feeder Tube

Pressure fluctuations were simulated by applying the pressure UDF to the feeder tube inlet boundary. In the nine transient simulations with pressure oscillations, 500,000 particles were injected into the domain incrementally in ten groups of 50,000. These ten injections were evenly spread out in time across the pressure wave, as shown in Figure 27. In each simulation, two injections occurred at the lowest point on the pressure wave while two injections occurred at the highest point. This was done so that the results would be representative of particles traveling on all parts of the pressure wave. The injection points were adjusted depending on the frequency of the oscillations so that all injections were conducted in like fashion according to the frequency of the pressure oscillation in the feeder tube.

Although the total pressure in the nozzle was governed by the UDF that generated a sine curve (see equation 12), it is observed that the sections of the curve below P_{avg} have kinks once per period, which is contrary to a perfect sine curve. This inconsistency is due to backflow in the feeder tube during the time that the feeder tube pressure drops below that of the annulus. The annulus inlet is held at a constant 4 MPa during these simulations, so when the feeder tube pressure drops below that of the annulus, the flow is directed into the feeder tube from the annulus. This backflow imposes on the sinusoidal boundary and manifests in a suppressed sine curve during

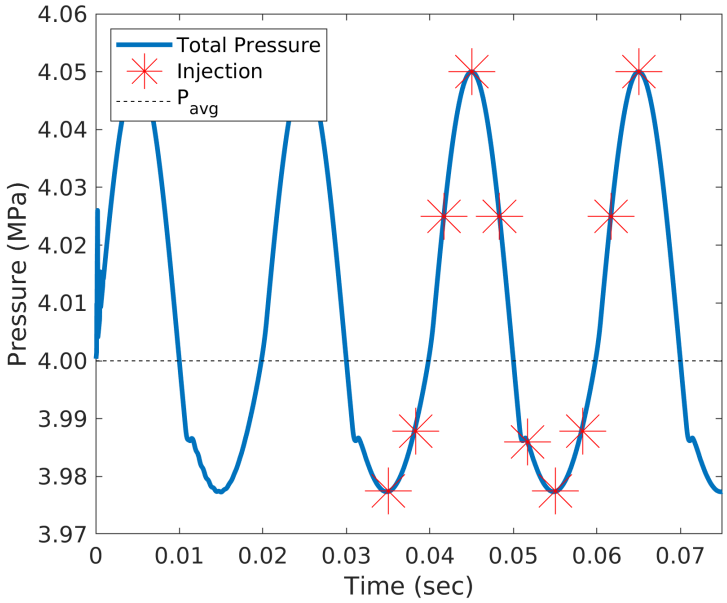

Figure 27: Feeder Tube Inlet Total Pressure vs Flow Time with Injection Locations

the times that pressure drops below 4 MPa. Even though there is a kink in the curve, the pressure still oscillates clearly and sufficiently to determine the effect that the oscillations have on particle dispersion.

Particles were injected only once the transient noise subsided and the pressure stabilized to its intended condition. Small oscillations can be seen on the lower part of the curve at 0.015 seconds, which is why injections did not begin until 0.035 seconds when the pressure became settled.

The resulting particle-wall collisions from the nine transient simulations with oscillating pressures are summarized in Figures 28 and 29. In all these models, bonding is successfully predicted in the diverging section, which suggests that the physics responsible for dispersion in the diverging section is accounted for when transient flow fluctuations are imposed. Like the prior two models (steady-state and transient with constant inflow), the smaller particles collide with faster velocities than the larger ones, but these transient models predict more collisions in the converging section than the prior two. A clear trend observed from Figures 28 and 29 is that as pres-

sure wave amplitude increases, the number of particles that bond increases. More particles are dispersed in the diverging section when the pressure wave amplitude is larger. There is no clear trend between pressure wave frequency and bonding.

The result of higher pressure amplitudes promoting dispersion agrees with Yin et al.'s finding that, when feeder tube pressures exceed those of the annulus, particle dispersion is increased [146]. A possibly related trend was found by Fukumoto et al. [29], who determined that larger inlet pressures resulted in higher deposition efficiencies – in the case of the present study, the deposition efficiency refers to that of the particles on the nozzle wall.

Although particles of all sizes are shown to bond in this study, Figure 28 demonstrates that the largest particles, with diameters ranging from 35 to 50 microns, all have CVRs close to one. This indicates that those particles are on the cusp of bonding, and that copper-nickel alloy particles with diameters slightly larger than 50 microns would not bond to the nozzle wall at all in a repeat experiment. The disadvantage to using such larger particles, however, is that although they would not bond to the nozzle, they also may not bond to the substrate if they cannot reach critical velocity.

It should be noted that the largest pressure wave amplitude (50 kPa) is only about 1% of the operating inlet pressure (4 MPa) and that a fluctuation of such a small magnitude still caused a significant amount of clogging. The results in Figure 28 show that very small oscillations in the feeder tube can cause a severe amount of clogging.

The oscillatory models successfully predict clogging, but the inlet boundary conditions are inconsistent between Siopis et al.'s experiments and the models in this work. In cold spray experiments, the feeder tube is set to a certain volumetric flow rate while the annulus is set to a certain temperature and pressure. The temperature difference between the feeder tube and the annulus is known to cause mixing and turbulence because high levels of shear arise from the two flows with different

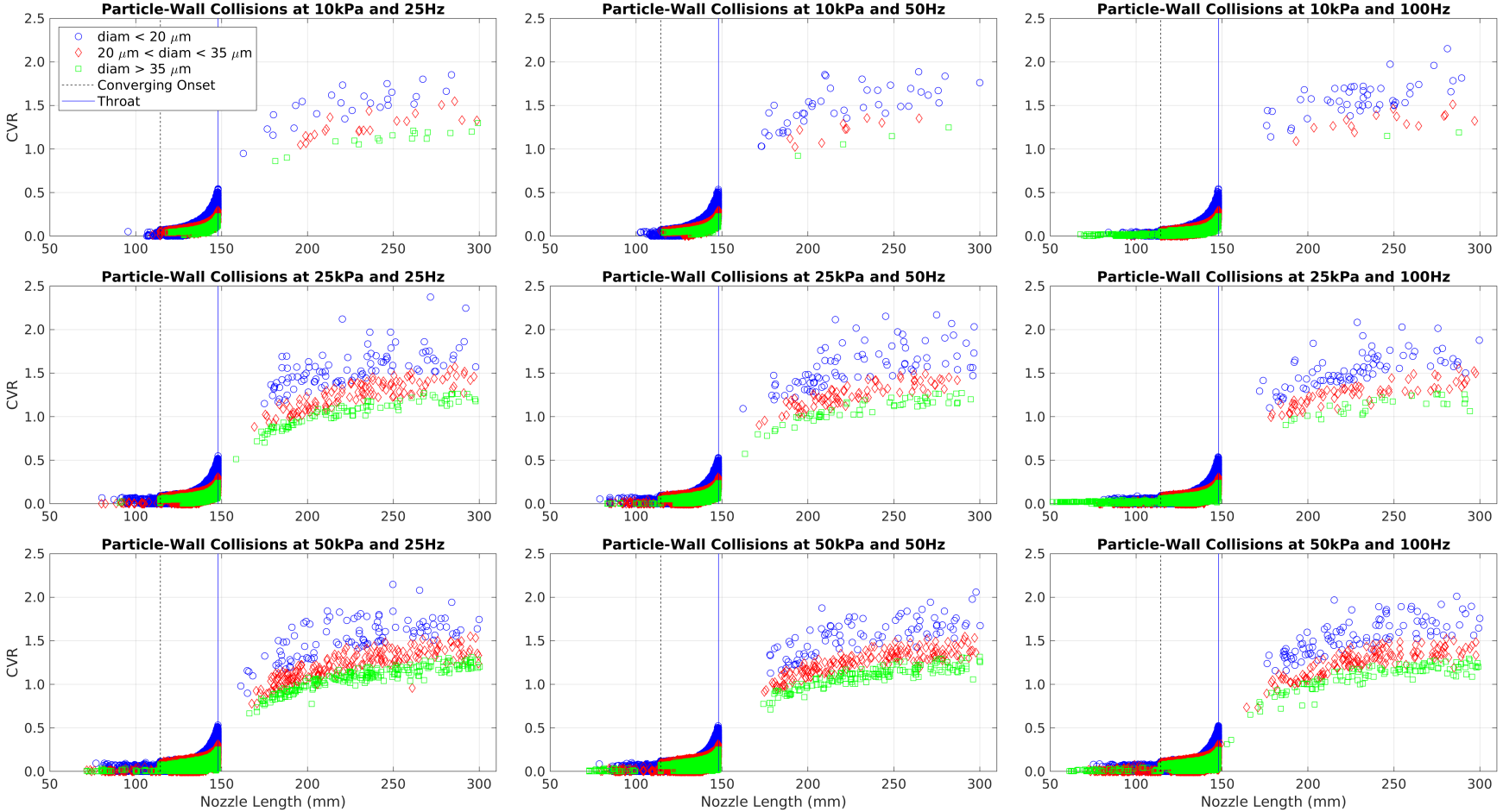

Figure 28: CVR vs Nozzle Length of Particle-Wall Collisions for Nine Oscillating Pressures

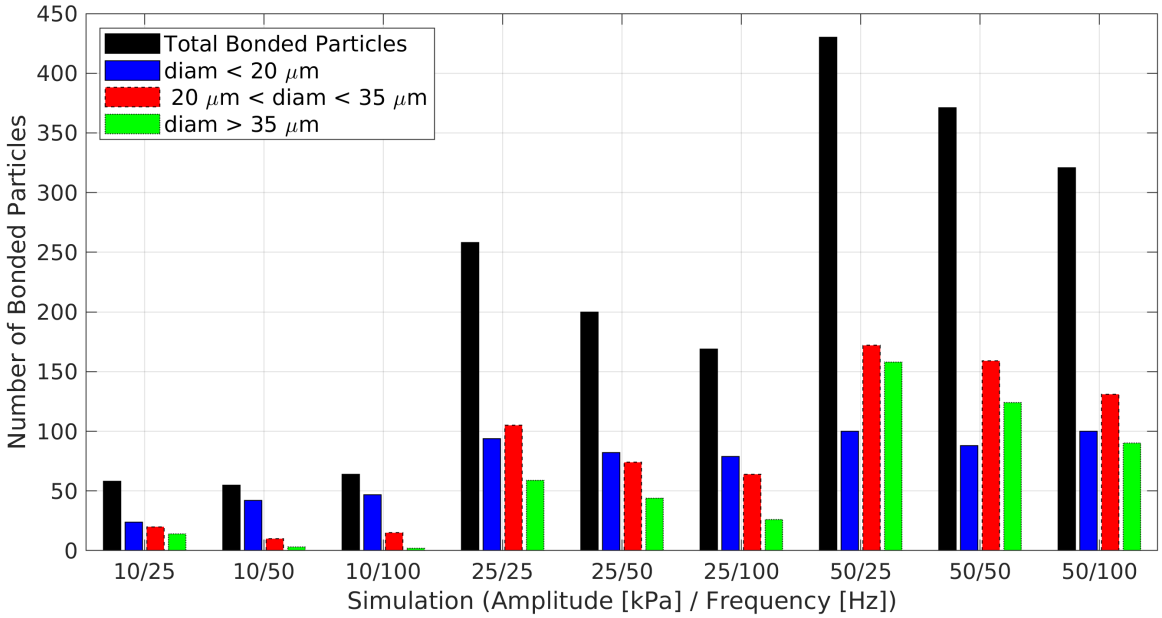

Figure 29: Bonded Particles from Nine Oscillatory Simulations

velocities merging. The resulting turbulence can cause increased dispersion among the particles.

The reason the inlet temperatures were both set to 673 K in this work is because it was already known that the mixing of the hot and cold gases causes dispersion. If the inlets were simulated at their realistic temperature conditions, the particle dispersion data would be the result of both mixing and feeder tube oscillations. The primary goal of this work is to determine the effect that feeder tube oscillations alone have on particle dispersion, and thus it was desirable to set both inlets to the same temperature to isolate oscillation effects.

Since the feeder tube is set to a certain flow rate in experiments, the oscillations that manifest are actually flow rate oscillations, not pressure oscillations. Although the total pressure oscillates with the flow rate, it is the oscillating flow rate which causes the pressure to oscillate, not the other way around. As was previously mentioned, the oscillatory pressure in this work results in backflow, which is not realistic in cold spray. An oscillatory flow rate does not result in backflow because, even when

the flow rate is at a minimum, the flow still moves forward, just slower. The assumption of equal inlet temperatures was a necessary means of confirming the hypothesis that flow oscillations alone, if present, can cause dispersion sufficient for clogging in a cold spray nozzle.

The inconsistency between boundary conditions in the experiments and these models may be the reason for the models overpredicting the expanse of clogging. In the results from Siopis et al., clogging was found in a narrow region of the diverging section (see Figure 20). The present simulations, however, predict collisions that lead to clogging along nearly the whole length of the diverging section (see Figure 28). It could be that the overprediction is due to the imposed oscillations being too large - after all, these fluctuations were not measured but rather were arbitrarily employed for the general purpose of determining how pressure wave amplitude and frequency affect dispersion. The selected values may too large to be realistic. Chapter three is dedicated to incorporating more realistic and specific flow rate fluctuations along with a realistic temperature difference between the inlets.

Another factor that may be responsible for the overprediction in the clogging expanse is the lack of local temperature effects included in calculating the critical velocity. As was previously discussed, increasing substrate temperature increases deposition efficiency [29, 99, 134, 148]. The higher wall temperature increases the energy available for bonding and thus reduces the required particle kinetic energy for bonding. Conversely, lower surface temperatures are detrimental to bonding, which means that in areas where the nozzle is cooler, particles are less likely to bond. This is the motivation behind nozzle cooling, which has proven to successfully prevent clogging in many otherwise clogging-prone situations [81, 132].

Since the tungsten-carbide nozzle inner wall gets slightly cooler down the length of the nozzle (see the adiabatic curve in Figure 10), it may be that the particles cannot bond as effectively farther downstream in the diverging section. If a parameter like

that of the critical velocity in Schmidt et al.'s work [104] were used that accounted for substrate temperature, the simulations may yield results that better align with those of experiments. It is unknown to what extent the results would change if the wall temperature were accounted for, but that is one possible reason for the overprediction. Unless the numerous phenomena at play during particle-wall interactions are further studied in future works, it will be difficult to predict clogging more accurately.

Figure 20 shows that the clogging location is greatly influenced by particle size in experiments. It is clear from Figure 28 that smaller particles reach critical velocity before larger ones, which means smaller particles bond before larger ones. When the small particles begin accumulating early in the nozzle, particles of all sizes begin accumulating onto those. The simulations in this work do not account for particle accumulation effects in the nozzle, but this may have a significant impact during experiments, which may be another reason for the overprediction in the modeled clogging expanse. This hypothesis is reinforced by comparing the difference between Figures 20a and 20b. When the fine particles are injected along with large ones, the fines drive the location of clogging closer to the throat, but when the fines are sieved out and only larger particles are injected, the clogging location is driven farther down the nozzle. Figure 28 also indicates that larger particles cause clogging farther down the nozzle while smaller ones begin to clog closer to the throat. To harmonize the results of Figures 20 and 28, the location of clogging seems to depend on where the smallest particles begin to bond. Small particles do not necessarily bond more than others (see Figure 29), but because they bond first, they drive the clogging upstream.

It is worth mentioning that although this was not the case in the experiments by Siopis et al. [109], some materials foul throughout the entire diverging section, not only in a small expanse [70]. If a cold spray scenario with nozzle and feedstock materials known to clog throughout the entire diverging section were modeled with

the methods of the present study, the model may predict the clogging expanse more accurately.

Discrepancies aside, the transient simulations with pressure oscillations successfully predict particle-wall collisions and bonding in the diverging section of the nozzle whereas the simulations with constant inflow conditions did not. With this finding, a possible root cause of particle dispersion and therefore clogging has been identified, which satisfies the primary goal of this work. Despite flow fluctuations being capable of causing clogging, it does not follow that all clogging scenarios are caused by such oscillations. These oscillations may not even exist in all cold spray processes. The chief conclusion of this chapter is that, if flow fluctuations in the feeder tube exist, they can promote dispersion such that clogging is provoked.

2.4 Conclusion

CFD simulations were performed to identify a potential root cause of particle dispersion and therefore nozzle clogging in cold spray. The models were based on specific experiments [109]. A steady-state model was initially investigated, which failed to predict the particle-wall collisions that those experiments reported downstream of the throat. This motivated a transient investigation of particle behavior with inlet conditions held at constant temperature and pressure, which also failed to predict collisions in the diverging section. Finally, nine transient simulations were conducted with pressure oscillations in the feeder tube at three wave amplitudes and three wave frequencies, all of which successfully predicted bonding in the diverging section. It is therefore concluded that pressure oscillations in the feeder tube, if present, can cause particle dispersion sufficient for clogging.

The pressure waves disperse the particles in proportion to the wave amplitude; larger wave amplitudes result in larger amounts of bonding in the diverging section.

There does not seem to be any correlation between the pressure oscillation frequency and the degree of clogging.

The maximum pressure oscillation amplitude was only 1% greater than the average pressure, and the models still predicted substantial amounts of clogging. To extend these conclusions, oscillations in the feeder tube can be due to vibrations, fluid-structure interactions, or other factors still not identified – oscillations are not just limited to pulsations in the feeder gas flow. In whatever form, oscillations in the feeder tube region, even if they are very small, are detrimental in that they can promote the onset of clogging aggressively. Future work could be dedicated to identifying and limiting such oscillations in the feeder tube region to alleviate nozzle clogging in cold spray.

CHAPTER 3

SIMULATIONS OF MASS FLOW OSCILLATIONS IN FEEDER TUBE

3.1 Motive and Background

Since chapter two has established that flow oscillations, if present, can cause particle dispersion and clogging, this study seeks to determine whether the rotating metering wheel that feeds powder into the injector tube causes flow fluctuations large enough to cause dispersion and clogging in cold spray nozzles. As was previously mentioned, clogging was identified by Sova et al. and attributed to observed pulsations in the feeder tube [114]. They determined: "Even the minimal possible powder feeding rates $\sim$0.05 cm^3/min were too high, leading to pulsations of the particle jet and being provoked a rapid mechanical clogging of the nozzle by the particles."

There are several potential causes for oscillations in the feeder tube, but the phenomenon investigated in the present study has particular relevance. The rotating metering wheel, to some extent, necessarily produces pulsations in the particle-laden gas stream as the feed holes pass by and the rotating plate cyclically obstructs and releases the flow into the feeder tube. Whether those cyclic oscillations from the rotating perforated plate are sufficiently large to cause dispersion and clogging is the subject of the present study.

Several CFD simulations based on Siopis et al.'s experiments [109] were conducted in the present work to model the transient effects of the rotating perforated plate on the powder stream characteristics. For context, a CAD drawing of the metering wheel used in Siopis et al.'s experiments [109] is provided in Figure 30.

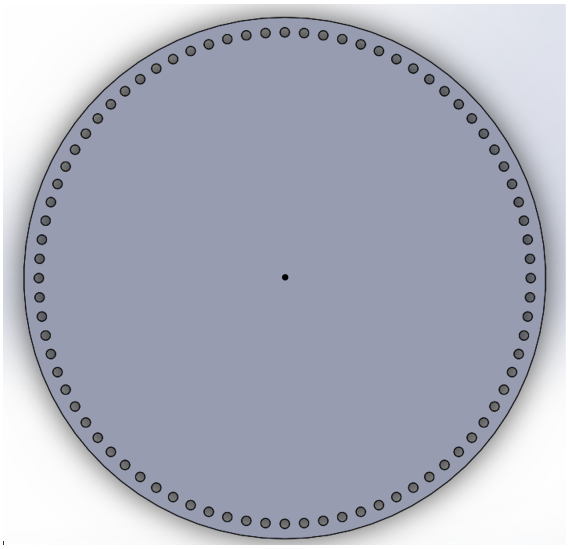

Figure 30: CAD Drawing of Metering Wheel

3.2 Modeling Methodology

3.2.1 Boundary Conditions

The feeder tube length is the only difference between the modeled geometry in the present study and that of chapter two. The entire length of the tube from the powder feeder to the injection point was ten feet in the experiments [109], and although there were some curves in the tube, the last four inches were kept perfectly straight. The four-inch straight section was accounted for in the model. Figure 31 provides the nozzle geometry used in this chapter.

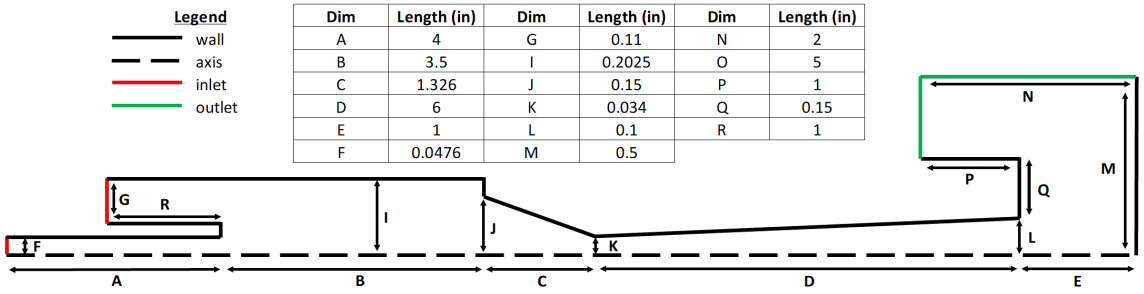

Dim	Length (in)	Dim	Length (in)	Dim	Length (in)
A	4	G	0.11	N	2
B	3.5	I	0.2025	O	5
C	1.326	J	0.15	P	1
D	6	K	0.034	Q	0.15
E	1	L	0.1	R	1
F	0.0476	M	0.5		

Figure 31: Nozzle Geometry - Long Feeder Tube (Flow Domain)

Certain nozzle wall boundaries were furnished with the same UDF from chapter two that recorded particle impact CVR and the location at which the collision occurred; in particular, they were those of the annulus, the prechamber, the "step" between the prechamber and converging section, the converging section, and the diverging section. The governing equations in that UDF are provided in equations 13 and 14. The particle rebound velocity was computed using normal and tangential coefficients of restitution of unity.

The boundary conditions in the present model are consistent with those of Siopis et al.'s experiments. The annulus temperature and pressure were 673 K and 4 MPa while the atmospheric outlet conditions were set to zero gauge pressure and 293 K. The feeder tube inlet was set to 120 SLPM in the experiments, so using equations 1 - 3, the volumetric flow rate was converted to a mass flow rate boundary condition of 0.33296 g/s. Fluent does not accept a volumetric flow rate as a boundary condition, but it does accept a mass flow rate. The feeder tube gas was experimentally measured at roughly room temperature, which was incorporated in the model as well (293 K).

Equations 15 - 24 were used to compute both the timing of the rotating perforated plate and the helium mass flow rate during the period the feeder tube is aligned with the feed holes. Firstly, the linear velocity of the metering wheel is described by equation 15:

$$v_{mw} = \omega_{mw} \times \ r_{mw} \tag{15}$$

where ω_{mw} is the metering wheel rotational velocity and r_{mw} is its radius measured from the center of the plate to the center of a feed hole (not to the outer edge of the metering wheel). The measurement to the center of a feed hole is relevant because it represents the position of the feeder tube with respect to the disk's center.

In this study, a cycle is defined as the time it takes for the perforated plate to first allow gas to pass through the feed hole and then prevent the gas from passing as

the feed hole proceeds beyond the injector. The cycle ends just before the next feed hole arrives at the injector. There are 80 cycles per revolution of the metering wheel because there are 80 feed holes in it. Equation 16 provides the arclength of one cycle:

$$L_{cyc} = \frac{C}{n_{fh}} \tag{16}$$

where n_{fh} represents the number of feed holes in the metering wheel and C is the circumference of the circle passing through the center of each feed hole. The circumference C is given by:

$$C = 2\pi r_{mw} \tag{17}$$

With the arclength of one cycle obtained, the elapsed time of one cycle is given by equation 18:

$$t_{cyc} = \frac{L_{cyc}}{v_{mw}} \tag{18}$$

To find the portion of L_{cyc} falling inside the diameter of one feed hole, which represents the distance the feed hole travels while allowing gas to flow through, equation 19 is employed:

$$L_{open} = \frac{\theta}{360}\, C \tag{19}$$

where the angle θ (measured from the metering wheel center in degrees) represents the angle proportional to the arclength L_{open}. The angle θ is calculated with equation 20. The variables in equation 20 are displayed in Figure 32 for context.

$$\theta = 2arctan\left(\frac{D_{fh}}{2r_{mw}}\right) \tag{20}$$

where D_{fh} is the feed hole diameter (74 thousandths of an inch).

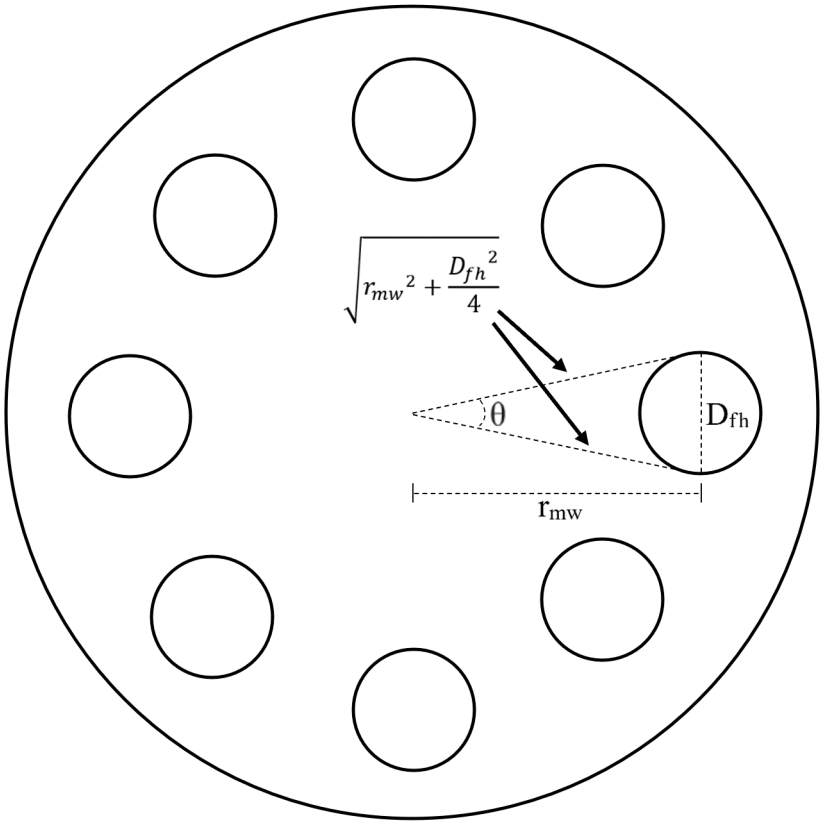

Figure 32: Variables Related to Computing θ
For conceptual visualization only.
Drawing not to scale and displays unrealistically low number of feed holes.

The amount of time that passes when the gas flow can pass through the feed hole is given by equation 21:

$$t_{open} = \frac{L_{open}}{v_{mw}} \tag{21}$$

and the duration of time that the flow is obstructed by the plate is given by equation 22:

$$t_{closed} = t_{cyc} - t_{open} \tag{22}$$

The terms t_{open} and t_{closed} were used in the present simulations to model at what times in the cycle the helium gas was allowed to flow and at what times it was prevented.

As calculated in equations 1 - 3, the average mass flow rate ($\dot{m}_{ave}$) is 0.33296 g/s, but because the mass flow rate fluctuates, the instantaneous mass flow rate is not

constant with respect to time. During t_{closed} the mass flow rate is zero (modeled at 0.0001 g/s), but during t_{open} the mass flow rate is larger than $\dot{m}_{ave}$. During t_{closed} the gas builds up while being blocked by the plate, and the accumulated gas is then released during t_{open}. The total mass of helium that passes through the feed hole during one cycle is given by equation 23:

$$m_{helium,cyc} = \dot{m}_{ave} \times \ t_{cyc} \tag{23}$$

Since all the helium mass passes through the feed hole only during t_{open}, the mass flow rate during t_{open} can be described by equation 24:

$$\dot{m}_{open} = \frac{m_{helium,cyc}}{t_{open}} \tag{24}$$

and the ratio of $\dot{m}_{open}$ to $\dot{m}_{ave}$ (which is also the ratio of t_{cyc} to t_{open}) is given by equation 25:

$$R_{open/closed} = \frac{\dot{m}_{open}}{\dot{m}_{ave}} = \frac{t_{cyc}}{t_{open}} \tag{25}$$

Since the distance from the center of the metering wheel to the center of the feed holes (r_{mw}) is 1003 thousandths of an inch, $R_{open/closed}$ is 2.08967. The rotational velocity of the metering wheel was set to 4 RPM in the experiments (in RPM, the rotational velocity of the metering wheel is given by $\omega_{mw,rpm}$), but in this numerical study three different rotational velocities were considered (2, 4, and 8 RPM) to evaluate the effects that varying $\omega_{mw,rpm}$ has on particle dispersion and clogging. These three angular velocities constitute the typical range of $\omega_{mw,rpm}$ used in cold spray.

The different rotational velocities of the metering wheel do not affect $R_{open/closed}$, but they do affect the values of t_{cyc} and t_{open}. The time durations t_{cyc} and t_{open} decrease as $\omega_{mw,rpm}$ increases. Table 6 provides the values of t_{cyc} and t_{open} at the three rotational velocities considered in this study.

Table 6: Feed Hole Timing Parameters at Three Rotational Velocities

$\omega_{mw,rpm}$ (RPM)	2	4	8
t_{cyc} (sec)	0.03927	0.01963	0.00982
t_{open} (sec)	0.01879	0.00940	0.00470

3.2.2 Mesh Description

After creating several meshes of various sizes and running steady-state simulations with them, the meshes with 75,398 cells or greater did not produce significantly different results from one another. The mesh with 75,398 cells was therefore selected for this study to obtain accurate results and conserve computation time. Three layers of thin cells were applied near the wall boundaries to resolve the boundary layer effects. The wall yplus values ranged from 0.25 to 4.5, the maximum being at the throat. The specific details of the mesh based on zone name are provided in Table 7.

Table 7: Mesh Specifications Based on Zone Name for Oscillatory Mass Flow Simulations

Zone	Cell Size (mm)
inlets	0.2
prechamber	0.2
converging	0.2
diverging	0.08
standoff	0.08
atmosphere	0.4

3.2.3 Gas Phase Modeling

As was the case in the previous chapters, the density-based implicit solver was used to converge these solutions to first-order accuracy. The helium density varied according to the ideal gas law while the thermal conductivity and viscosity varied with respect to temperature according to equations 4 and 5.

The k-ϵ realizable turbulence model with standard wall functions was used to predict the turbulent fluctuations in the flow. Since this chapter is a continuation of the previous one and the k-ϵ realizable model was deemed most appropriate for that chapter, it seemed appropriate to use that model for this chapter as well.

3.2.4 Discrete Phase Modeling

Although it may be desirable to account for two-way coupling between the fluid and the particles to capture realistic particle dispersion effects, a realistic number of particles needs to be injected in the model so that realistic effects ensue. Therefore, the sample size of particles passing through a single feed hole (representing one injection, or one cycle) must be obtained.

Equation 26 provides the method of calculating the particulate mass passing through the feed hole in one cycle:

$$m_{p,cyc} = \dot{m}_p \, \frac{1}{\omega_{mw,rpm}} \, \frac{1}{n_{fh}} = 0.0437 \text{ g/cyc} \tag{26}$$

where $\dot{m}_p$ is the powder feed rate (14 g/min) used in the experiments.

The volume of an individual particle is given by equation 27:

$$V_{p,i} = \frac{4}{3}\pi \left(\frac{D_p}{2} \right)^3 \tag{27}$$

while the total volume of a sample size of particles is provided in equation 28:

$$V_{n_p} = \sum_{i=1}^{i=n_p} V_{p,i} \tag{28}$$

where n_p is the particle sample size.

An assumption made in equations 28 - 32 is that all particle diameters are perfectly evenly spaced apart between 5 and 100 microns. In Siopis et al.'s experiments, the

particle size distribution was roughly Gaussian. In the present models, the particles were randomly distributed with equal likelihood between 5 and 100 microns so that conclusions could be made about particle behavior based on diameter, rather than to be realistic. The assumption made in equations 28 - 32 of perfectly evenly spaced diameters is similar to the size distribution in the models and was applied to simplify the calculations.

Equation 29 gives the total mass of a particle sample size:

$$m_{n_p} = \rho_p \times V_{n_p} \tag{29}$$

Figure 33 serves to determine the number of particles in each injection. The known particulate mass passing through the metering wheel per cycle ($m_{p,cyc}$) is represented by the solid blue line. The dotted red line is a plot of equation 29 showing how the total particulate mass of a sample (m_{n_p}) increases with sample size (n_p). As sample size increases, so does the total mass of the sample. Since the volume of a sample (V_{n_p}) increases as sample size increases (see equation 28), the sample mass must likewise increase (see equation 29).

A simple numerical method was employed to find at what sample size the calculated mass (m_{n_p}) is closest to the known mass ($m_{p,cyc}$). The residual between m_{n_p} and $m_{p,cyc}$ was computed for each sample size with equation 30:

$$r_{n_p} = |m_{p,cyc} - m_{n_p}| \tag{30}$$

As equation 31 indicates, the smallest residual occurs at a sample size of 591 particles:

$$\min(r_{n_p}) = r_{n_p=591} = 4.5892\text{e -}11 \tag{31}$$

In summary, the calculated particulate mass based on sample size (m_{n_p}) for one cycle is nearly equal to the known particulate mass in one cycle ($m_{p,cyc}$) when the

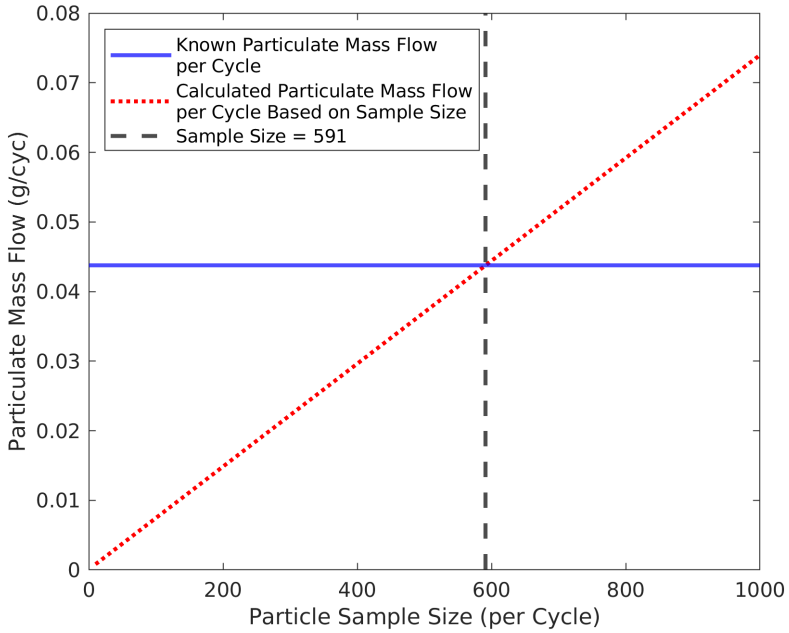

Figure 33: Particulate Mass Flow per Cycle

particle sample size is 591:

$$m_{n_p=591} \approx m_{p,cyc} = 0.0437 \text{ g/cyc} \tag{32}$$

It is therefore concluded that each injection ought to consist of roughly 600 particles if two-way coupling is to be realistically accounted for. Because particle-wall bonding is such a low-probability event in these models, 600 particles per injection are too few to obtain particle-wall collision results in a practical amount of wall-time. In order to predict significant bonding, the models in chapter two required ten injections of 50,000 particles each, providing a total sample size of 500,000. A similar sample size is required for the present chapter, as well. Incorporating two-way coupling with 50,000 particles per injection is a futile effort because the sample size in the models would be 83 times that of the experiments (roughly 600 particles). If two-way coupling were computed with 83 times the realistic number of particles present, the effects would be dramatically exaggerated. For this reason, one-way coupling between

the particles and the fluid was employed in the models. Besides, the ratio of particle mass flow rate to fluid mass flow rate is 0.049 while the ratio of particle volumetric flow rate to fluid volumetric flow rate is 6.87e-6. The mass and volume ratios of particles to fluid are both low, which further justifies the assumption of one-way coupling. The same governing equations for particle motion and heat transfer used in chapters one and two were also implemented in this chapter (equations 7 - 10).

The first injection occurred at flow time equal to t_{cyc} to give the flow enough time to become established and to allow the initial transient noise to subside before injecting. Each subsequent injection occurred at an increment of t_{cyc} until the last injection, which occurred at $10t_{cyc}$.

The same copper-nickel alloy particle material from chapter two was employed in this study to replicate the experiments of Siopis et al., with a density of 8940 kg/m^3 and a specific heat capacity of 380 J/kg-K. To compensate for the two-dimensional nature of the model, particles were generated with greater likelihood away from the centerline by a factor of the square root of radial position. This compensation spawns particles in a 2-D space as if they were occupying a 3-D space with uniform position density. Several sets of simulations were run in this study, some employing particles with zero initial velocity, some incorporating an initial velocity of 25 m/s (which is the feeder tube flow velocity), and some with initial trajectory angles. All particles were injected at room temperature (293 K).

3.3 Results

3.3.1 Steady-State Model

Three different injections were simulated with a steady-state model. The first injection consisted of particles with zero initial velocity, the second incorporated an axial initial particle velocity of 25 m/s, and the third employed particles with a 25 m/s initial velocity and randomly assigned initial trajectory angles ($\alpha_{p,0}$, measured

from the centerline) between zero and 10°. Ten degrees was selected as the maximum initial trajectory angle because it seemed unlikely that particles could obtain a much steeper angle during their journey through the feeder tube. Comparing the steady-state results of these three injections helps ascertain how the initial conditions of the particles affect dispersion without transient pulsations in the feeder tube. The steady-state results also provide a base case to compare with the transient results. Since chapter two demonstrated that transient models with constant inflow conditions produce similar particle collision results as steady-state models, any differences in particle behavior between the steady-state and transient models in this chapter can be attributed to the feeder tube oscillations in the transient models.

Figure 34 presents the steady-state particle-wall collision data for the three different injections. The first two injections, with $\alpha_{p,0} = 0°$, resulted in zero collisions with CVRs greater than one, indicative of no bonding (Figure 34a and 34b). Furthermore, there are zero collisions predicted in the diverging section with the first two injections. The injection with initial particle trajectory angles ranging between 0 and 10°, however, resulted in many collisions in the diverging section, some of which resulted in bonding (Figure 34c). Figure 34 shows that the initial trajectory angle plays a greater role in clogging than particle initial velocity.

These initial trajectory angles cannot be the entire cause of clogging though, because in the experiments, the smallest particles determined the location of clogging (see Figure 20), whereas in Figure 34c, the smallest particles are not predicted to bond at all. The steady-state solution with initial particle trajectory angles may successfully predict *some* clogging, but it does not predict *all* the bonding known to occur in experiments, particularly with the smallest particles.

When employing initial trajectory angles, large particles will disperse more because of their high inertia. They will not be easily coerced by the axial flow direction and thus will continue traveling radially as well as axially, in contrast to the small

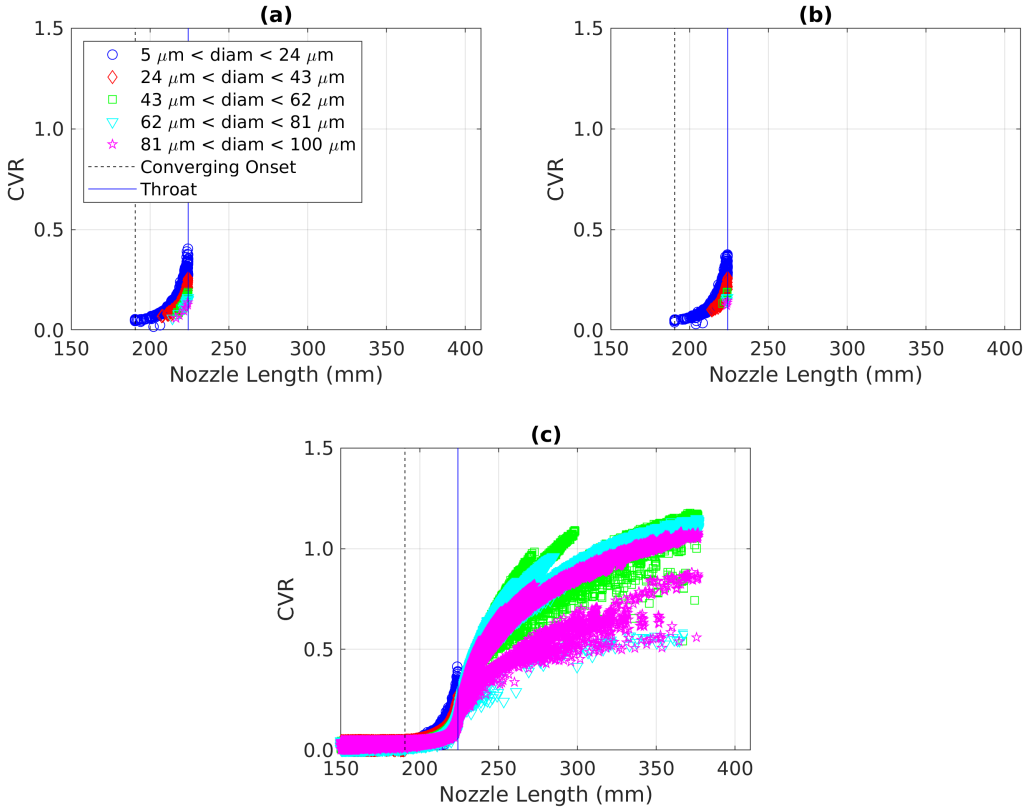

Figure 34: CVR vs Nozzle Length - Steady-State
(a) $v_{p,0} = 0$ m/s, $\alpha_{p,0} = 0°$
(b) $v_{p,0} = 25$ m/s, $\alpha_{p,0} = 0°$
(c) $v_{p,0} = 25$ m/s, $\alpha_{p,0} = 0$-$10°$

particles (with low inertia) which are heavily influenced by the flow momentum and thus travel more axially.

Despite the steady-state model predicting some clogging with angled initial trajectories, there is still more physics responsible for clogging than what this model provides because it does not predict the experimentally proven phenomenon of clogging with small particles.

3.3.2 Transient Models

Several transient simulations were solved to isolate the effects of helium mass flow rate pulsations in the feeder tube due to the rotating metering wheel. First, the

injection with $v_{p,0} = 0$ m/s and $\alpha_{p,0} = 0°$ was used with the three different values of $\omega_{mw,rpm}$ (2, 4, and 8 RPM), the results of which are provided in Figure 35.

The collisions presented in Figure 35 all occur in the converging section and below the bonding criteria (CVR = 1), which indicates that the transient model with $v_{p,0}$ = 0 m/s and $\alpha_{p,0} = 0°$ does not capture all the physics responsible for particle dispersion and bonding in experiments. It is unclear why seemingly few medium-sized particles collide in the case with $\omega_{mw,rpm} = 4$ RPM compared to the other two angular velocities.

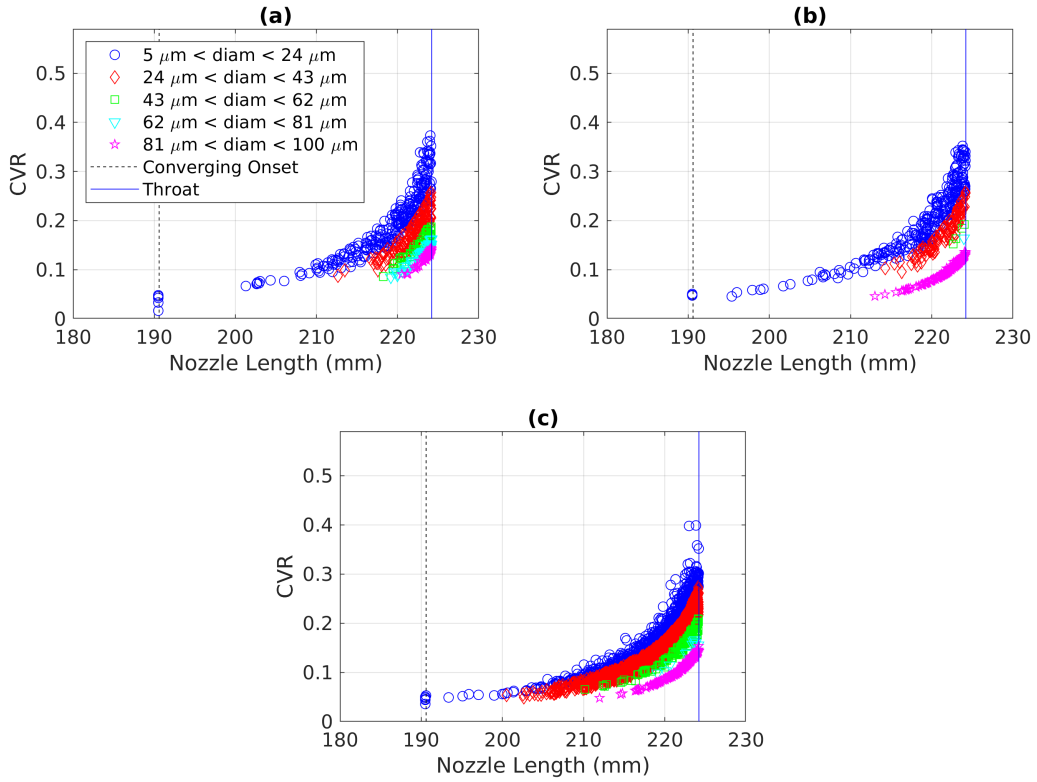

Figure 35: CVR vs Nozzle Length
$v_{p,0} = 0$ m/s, $\alpha_{p,0} = 0°$
(a) $\omega_{mw,rpm} = 2$ RPM
(b) $\omega_{mw,rpm} = 4$ RPM
(c) $\omega_{mw,rpm} = 8$ RPM

The next set of simulations conducted in this chapter incorporated the injection with $v_{p,0} = 25$ m/s and $\alpha_{p,0} = 0°$ at the same three values of $\omega_{mw,rpm}$. The ensuing

results are presented in Figure 36 and are similar to those displayed in Figure 35, which indicates that the physics responsible for dispersion and clogging are not fully accounted for in the oscillatory model with $v_{p,0} = 25$ m/s and $\alpha_{p,0}$, either.

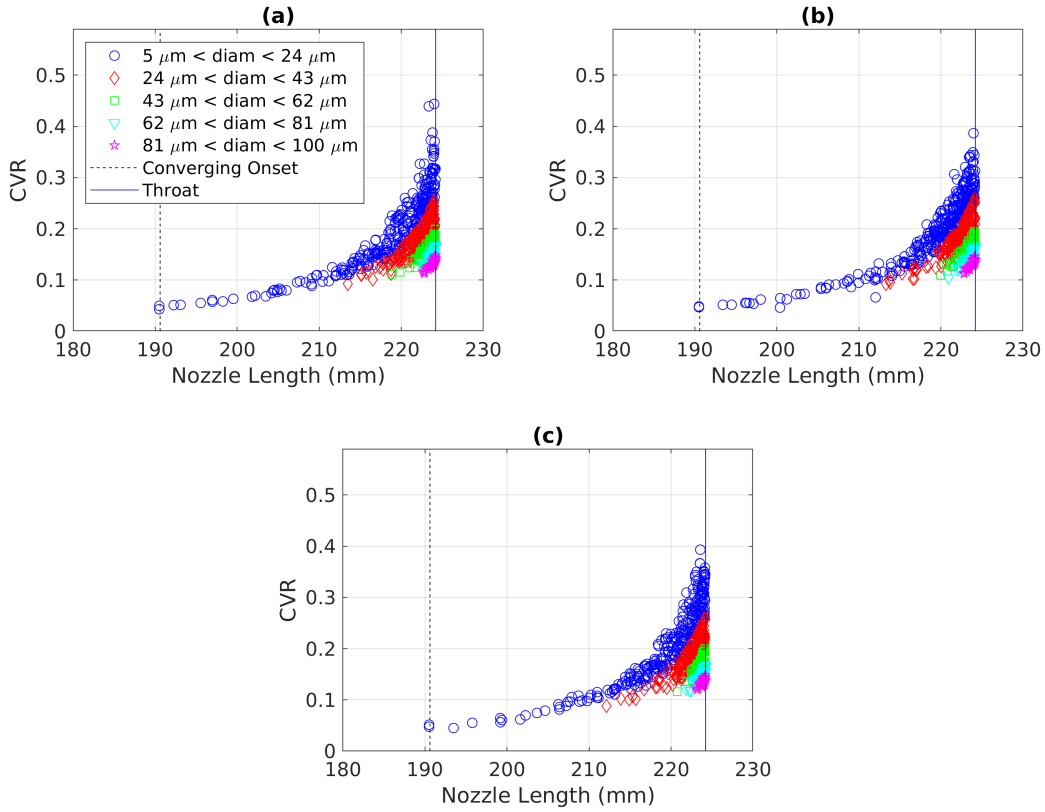

Figure 36: CVR vs Nozzle Length
$v_{p,0} = 25$ m/s, $\alpha_{p,0} = 0°$
(a) $\omega_{mw,rpm} = 2$ RPM
(b) $\omega_{mw,rpm} = 4$ RPM
(c) $\omega_{mw,rpm} = 8$ RPM

It seems most realistic to model particles with an initial velocity close to the feeder tube flow velocity, as was done in Lupoi and O'Neill's dispersion study [72], rather than injecting them at rest. Similar results ensue with both injection methods though, which shows that the present models are not sensitive to particle initial velocity.

The results of the injection employing $v_{p,0} = 25$ m/s and $\alpha_{p,0} = 0$-$10°$ with all three metering wheel rotational velocities are presented in Figure 37. The collisions are similar to those observed in Figure 34c, which shows the steady-state collisions

with $v_{p,0}$ = 25 m/s and $\alpha_{p,0}$ = 0-10°. All three metering wheel velocities produce similar collisions with $v_{p,0}$ = 25 m/s and $\alpha_{p,0}$ = 0-10°.

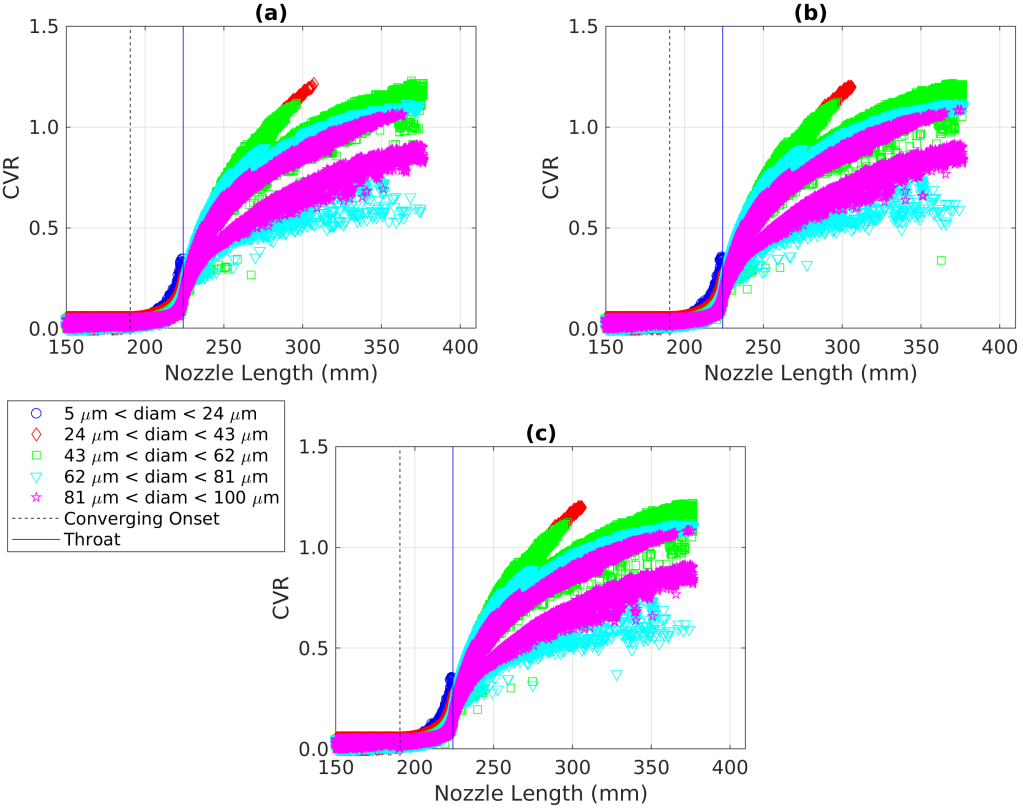

Figure 37: CVR vs Nozzle Length
$v_{p,0}$ = 25 m/s, $\alpha_{p,0}$ = 0-10°
(a) $\omega_{mw,rpm}$ = 2 RPM
(b) $\omega_{mw,rpm}$ = 4 RPM
(c) $\omega_{mw,rpm}$ = 8 RPM

The smallest particles are not predicted to bond, which was also the case with the steady-state model using the same injection. Although the transient models exhibited in Figure 37 are an improvement over the steady-state model in that they predict bonding for particles in the 24-43 micron range, they still do not predict bonding for the smallest particles, which are in the 5-24 micron range. Siopis et al.'s experiments [109] found that, in particular, the 5-15 micron particles determined the location of clogging. Like the aforementioned models, even the transient models with $\alpha_{p,0}$ = 0-10° do not predict clogging for small particles, indicating that the clogging found

in Siopis et al.'s experiments is not entirely due to flow pulsations from the metering wheel.

Figures 37 and Figure 34c show that clogging is highly sensitive to the particle initial trajectory angle inside the feeder tube. Even with angles as shallow as 10°, clogging was provoked significantly. Although such a study would be challenging, a valuable future work could investigate the trajectory angles of particles inside the feeder tube as a means to better predict clogging.

For flow pulsations to cause dispersion adequate for clogging, they need to redirect the particle trajectories enough for the particles to collide with the diverging wall, which was not the case in this study with the smallest particles. Even shallow initial particle trajectory angles caused more clogging than the flow oscillations did. There is very little difference between the particle-wall collisions occurring in the steady-state compared to those occurring with the transient effects of the rotating metering wheel, which implies that the metering wheel effects are inconsequential to clogging. Furthermore, there is not a significant difference between the number of collisions transpiring at any of the three metering wheel angular velocities, which agrees with the finding from chapter two that pressure wave frequency does not affect clogging.

Even when the value of $\dot{m}_{open}$ was increased unrealistically to four times its actual value (with the timing t_{cyc} and t_{open} remaining at their realistic values), the models still did not predict clogging for the smallest particles. Other phenomena must be responsible for particle dispersion, which should be investigated in future work. Vibrations or fluid-structure interactions between the feeder tube wall and the powder feed gas may be responsible for particle dispersion and clogging [66], which could be the subject of a valuable future study.

3.4 Conclusion

The present chapter is based on specific nozzle clogging experiments by Siopis et al. [109], and is a continuation of chapter two. It has been hypothesized in a certain cold spray study [114] that pulsations in the particle jet provoke nozzle clogging. In light of chapter two demonstrating that flow oscillations can indeed cause clogging, the present chapter serves to determine whether the flow oscillations produced specifically by the rotating metering wheel are large enough to cause clogging. As the metering wheel rotates, it cyclicly permits and blocks the driving gas from flowing through it, causing pulsations in the driving gas mass flow rate.

Several CFD models were developed to study the effects of these transient mass flow rate pulsations on particle dispersion and clogging. Starting with a steady-state flow solution, three different particle injections were evaluated. The two injections with zero particle initial velocity and axial initial velocities of 25 m/s (equal to feeder tube gas velocity) performed similarly, producing collisions only in the converging section and well below critical velocity. The third injection, which incorporated particle initial velocities of 25 m/s and initial particle trajectory angles between zero and ten degrees (measured from the centerline), resulted in a prediction of clogging. Contrary to the experimental results, however, the smallest particles were not predicted to bond at all. In the experiments, the smallest particles played the greatest role in clogging. The discrepancy between the experimental and modeling results indicates that the physics responsible for particle dispersion and clogging of small particles is not present in the steady-state model.

Nine transient models were subsequently investigated, incorporating the three injections previously mentioned and three metering wheel angular velocities of 2, 4, and 8 RPM. The transient effects of the metering wheel were not found to be significant, as the transient models produced similar results to those solved in the steady-state. Even when unrealistically large mass flow pulsations of four times the

actual value were employed, the smallest particles were still not predicted to clog. It was additionally determined that varying the metering wheel's angular velocity had little effect on particle behavior, which agrees with the finding from chapter two that flow oscillation frequency does not significantly affect clogging.

On the other hand, the particle trajectory angle inside the feeder tube was found to affect clogging tremendously. Angles as low as 10° proved to provoke clogging significantly. In light of clogging being so sensitive to it, a difficult but valuable future study could investigate the trajectory angle of particles inside the feeder tube.

Because the flow fluctuations from the metering wheel are too small to substantially alter particle trajectories, they are found not to be a root cause of clogging in cold spray. The physics responsible for clogging must stem from phenomena other than pulsations due to the rotating metering wheel. Future studies could investigate the effects of vibrations and fluid-structure interactions between the feeder tube wall and the powder feed gas to consider other possible root causes of clogging.

CHAPTER 4

PROPENSITY FOR CLOGGING OF NOVEL NOZZLE GEOMETRIES

4.1 Motive and Background

Although nozzle cooling mitigates clogging in many otherwise clogging-prone scenarios, it cannot prevent clogging in all cases. As was discovered in chapter one, the cooling method is not effective for fine (small) particles. Furthermore, nozzle erosion may still occur with cooling because even though bonding is prevented, particle-wall collisions can still result in erosion of the nozzle wall. The empirical relation for erosion by Moridi et al. does not depend on nozzle wall temperature [80], which would indicate that erosion still occurs at the same rate independent of cooling. As was mentioned previously, however, the empirical relation for critical velocity by Schmidt et al. [104] does not contain a term for substrate temperature despite it being known that substrate temperature affects bonding [29, 99, 134, 148]. It could be that the erosion equation by Moridi et al. similarly neglects to account for substrate temperature. It seems likely that erosion occurs to some extent even amidst cooling, but further study should be dedicated to this topic.

Erosion is preferable to fouling (particle accumulation on the nozzle wall) because at least the particles get deposited on the substrate despite the nozzle being somewhat compromised. Polybenzimidazole (PBI) nozzles are often used with clogging-prone materials to allow the particles to erode the nozzle rather than adhere to it [133]. Erosion is still problematic though because once the nozzle geometry is compromised the flow velocity decreases, which then maligns the particle velocity. When particle velocity decreases, the particles' ability to reach critical velocity is jeopardized.

Several studies have investigated bonding-resistant nozzle materials to avoid clogging [28, 31, 47], but these methods are either unproven or still have significant limitations. Tungsten carbide is typically used as the nozzle material when spraying clogging-prone powders because it is extremely hard and bond-resistant, but clogging still occurs with it.

There are several difficulties associated with modeling the fouling phenomenon. First of all, the wettabilitiy of powder materials on tungsten carbide is currently not well understood, nor are the effects of nozzle wall roughness. Single-particle impact experiments can help ascertain bonding and rebound properties, but these studies are often conducted under perpendicular impact conditions rather than shallow angles [46]. Because bonding occurs at especially shallow angles relative to the nozzle wall during fouling, it is necessary to account for such angles. Besides, there is even debate in the cold spray community regarding perpendicular particle-substrate bonding; whether it depends on the formation of an adiabatic shear instability [7] or not [37]. In light of such debate, it is unsurprising that the phenomena responsible for bonding in more complicated conditions (with steep angles and unknown roughness) are not fully known.

There is also difficulty in ascertaining the phenomena related to collisions which rebound off the wall, specifically regarding the coefficient of restitution. It is known that the coefficient of restitution depends on the particle material strength and density [155] along with its regime of plastic deformation during impact [143]. In particular, aluminum 6061 particles have been measured to have a coefficient of restitution on the order of 0.1 when traveling within the range of 50-1000 m/s, but these measurements are for 90° impacts rather than shallow angles [17, 141]. These measured values are therefore not applicable to the present models, as there are still more complexities that are not understood [74].

Kleis and Hussainova studied the coefficient of restitution for steel spheres at impact angles between 15° and 90° [48], but their spheres were 700 microns in diameter, which are much larger than cold spray particles. Also, the impact speed only went up to 150 m/s, which is far below the impact speed of cold spray particles. Although methods of modeling particle rebound effects on rough surfaces exist [111], an additional challenge is that they require a thorough comprehension of the inner nozzle surface topography, which is lacking to date.

A wide range of coefficient of restitution values have been employed in cold spray and similar studies. In their study on particle-wall interactions in two-phase flow, Nguyen and Fletcher assumed a coefficient of restitution of unity [84]. Faizan-Ur-Rab et al. did likewise in their numerical study on particle behavior inside their cold spray nozzle [25]. Karimi et al. modeled the cold spray process with an angled substrate and their tangential and normal coefficients of restitution were 5/7 and between 0.07 and 0.1, respectively [44]. It should be noted that Karimi et al.'s values were used at the substrate where velocities are close to critical, which explains why their values are relatively small. Ozdemir and Widener found that changing both the normal and tangential coefficients of restitution inside their cold spray nozzle did not change the difference between the average particle velocity of their CFD model and that of their experiments [87].

Although Ozdemir and Widener's results show that average particle exit velocity is fairly unaffected by the coefficient of restitution, particle dispersion is certainly affected. If the normal coefficient of restitution is very small, the particles will be prevented from moving radially after their first collision with the nozzle wall, which necessarily prevents dispersion. Predicting particle dispersion inside a cold spray nozzle is a challenge for many reasons, one being insufficient research to date regarding the normal coefficient of restitution inside the nozzle. In this study, the normal

coefficient of restitution inside the nozzle is varied to observe how it affects particle dispersion.

In their study on nozzle clogging, Wang et al. [132] make an important observation. Their experiments revealed that, while spraying aluminum powder, clogging occurred just downstream of the throat. Their models, however, showed that particles colliding in that region were traveling well below critical velocity. According to the models, the particle velocity magnitude in that region was about 300 m/s, which is roughly half the critical velocity of aluminum for 25 micron particles [104]. It is known that the smaller particles have the greatest influence on clogging and also travel the fastest, but even Wang et al.'s smallest particles of 5 microns did not reach a velocity magnitude of 600 m/s until farther down the diverging section. The particles bonded to the inner nozzle wall at subcritical velocity, which led them to conclude: "there must be additional factors inducing nozzle clogging". Wang et al. make no mention of sieving the powder to a specified size range in their experiments, so it may be that particles smaller than 5 microns, which travel faster, were present in the experiments but were unaccounted for in the models. Regardless, it is certain that if particles do not collide with the diverging wall, they cannot bond. Altering the nozzle internal geometry may achieve the goal of preventing nozzle clogging by causing the particles to altogether avoid contacting the diverging wall.

Nozzle geometry design optimization has been studied in cold spray since 1998 [23]. Most work dedicated to optimizing nozzle geometry has revolved around maximally facilitating bonding at the substrate. Some geometry optimization techniques seek to maximize particle impact temperature to soften the particles [62], but the majority revolve around achieving the greatest possible impact velocity.

Sakaki and Shimizu found that as the converging section length increases, the deposition efficiency and the coating hardness increase while the particle velocity slightly decreases [101]. The increased deposition efficiency and coating hardness

can be attributed to more mixing inside the long converging section and therefore increased particle heating and ultimately a better deposit [119]. Their conclusion about reduced velocity, however, is rather misleading. As the converging section increased in length, Sakaki and Shimizu held their total nozzle length constant, so by however much the converging section length increased, the diverging section length accordingly decreased. Since most of the particle acceleration occurs in the diverging section, it is no surprise that the shorter that section is, the slower the particles will be. Li and Li conducted a separate study in which the convergent length was varied independently of the other nozzle dimensions and found that convergent length has little effect on particle velocity [64].

The diverging section length has a tremendous influence on particle velocity because it is in this section that the flow is supersonic and that the particles accelerate most [6, 149]. The expansion ratio of the nozzle plays a major role as well because it determines how the flow will expand [59, 64]. If the flow is under-expanded or over-expanded, strong shockwaves will be produced and will majorly disperse particles [79, 90]. For this reason, it is necessary to employ an optimal expansion ratio so that the flow is optimally expanded.

In terms of nozzle dimensions, the diverging section length and expansion ratio have the greatest impact on particle velocity. A cold spray dimension unrelated to nozzle geometry that strongly influences both particle velocity and dispersion is the standoff distance [129]. In the present work, however, the diverging length, expansion ratio, and standoff distance are all maintained constant. The present study seeks to alter the prechamber and converging section shapes and lengths to prevent particle-wall collisions in the diverging section. All novel nozzle geometries presented in this chapter employ a conical diverging section rather than a wall with curvature. It could be that a curved diverging wall would better prevent particle-wall collisions, but this study isolates the effects of prechamber and convergent section shape and length.

Plus, it would complicate the simulations since the curved wall in the supersonic region would require certain corrections for boundary layer growth [110, 121]. Perhaps a future study could investigate the possibility of a curved diverging wall for clogging prevention.

It should be noted that although it is desirable in this study to minimize collisions in the diverging section, there is also cold spray work dedicated to enhancing particle dispersion in the nozzle to achieve a uniform deposit on the substrate [118, 142]. These motives conflict because particle dispersion leads to clogging. As is often the case, when one problem is solved, another ensues. Hopefully, the geometries presented in this chapter successfully prevent collisions and meanwhile allow for a uniform particle footprint, but it should be acknowledged that the primary purpose of this study is to prevent particle-wall collisions in the diverging section regardless of how uniform the particle footprint is.

Simulations have been instrumental in optimizing the cold spray process in previous works. In the same way that Li et al. used an optimized nozzle geometry to achieve a dense 316L stainless steel coating with high microhardness using air as an accelerating gas [61], the present study aims to find an optimal nozzle geometry for the purpose of preventing particle-wall collisions in the diverging section to ultimately prevent clogging. If such a geometry can be produced, the limitations of nozzle cooling would be resolved because fine particles would cease to clog and erosion would be completely prevented.

4.2 A Brief Note on Aerodynamic Lenses

Aerodynamic lenses are a technology designed to focus a particle beam in a converging-diverging nozzle. An aerodynamic lens is a thin-plate orifice which particle-laden gas passes through prior to nozzle expansion. The gas contacts the plate, is squeezed through the orifice at the center, and afterward expands back to its original

state. The particles are pulled by the fluid toward the centerline from some radial distance away, but their inertia prevents them from rebounding perfectly to their initial radial positions after passing through the lens. Instead, the particles find themselves closer to the centerline (if certain parameter requirements are met), thus becoming more focused [68]. Moreover, as more lenses are added in series and properly spaced apart, particle beam widths are reduced asymptotically [69]. Figure 38 illustrates the principle of aerodynamic lens focusing.

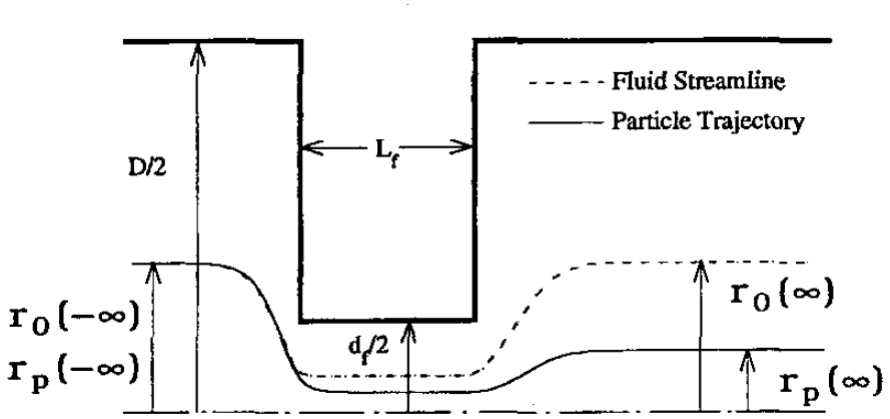

Figure 38: Axisymmetric Schematic of an Aerodynamic Lens [68]

The capability of aerodynamic lenses to focus a beam of nanoparticles has been validated both theoretically and experimentally [68, 69, 153, 154]. Since the process of designing an aerodynamic lens system for a given nozzle geometry and particle size distribution is often frustratingly long and iterative, there has even been made a design tool to help minimize the iterative process [130] that comes with an instruction manual [131]. For a set of given process parameters, this tool quickly provides a reasonably accurate lens design and evaluation.

Several studies have specifically demonstrated the ability of aerodynamic lenses to deposit a focused particle beam onto a nearby substrate [30, 96], which has implications on the viability of aerodynamic lenses in cold spray. In fact, Alhulaifi

successfully focused and deposited copper nanoparticles by implementing three aerodynamic lenses in his novel cold spray nozzle geometry [3].

Despite their ability to minimize dispersion with nanoparticles, there are obstacles to using aerodynamic lenses with typical cold spray particle sizes (5-100 microns). Since typical cold spray particles are much larger, they have more inertia than nanoparticles, which makes them prone to collide and adhere to the lens rather than move around it. Spraying into a vacuum outlet, the largest particles Zhang et al. managed to focus with their aerodynamic lens system were 2.5 microns, and only with a transmission efficiency of 40% (the rest were lost on the lens) [154]. Most aerodynamic lens systems operate with a nozzle outlet in vacuum [38] because there are complications associated with using them with an atmospheric outlet, rendering them difficult to use in the cold spray process [8]. Despite these complications, Lee et al. [56] successfully focused particles of up to 10 microns into an atmospheric pressure environment, which is at least inside the range of typical cold spray particle sizes, but only at Reynolds numbers up to 700, which is insufficient to compare to the higher Reynolds numbers found in the nozzle of this present study. Deng et al. [21] likewise managed to focus particles of up to 10 microns in the atmospheric pressure range at Reynolds numbers of about 1800, but with the same discouraging 40% transmission efficiency as Zeng et al. The Reynolds number inside the prechamber of the present nozzle (which is where the lenses would be employed) is 26,500 - almost 15 times larger than that of Deng et al.

The parameter that describes how closely a particle will adhere to the fluid streamline is the so-called Stokes number. Conceptually, the Stokes number is the ratio between the characteristic reaction times of the particle and fluid [77]:

$$St = \frac{\tau_p}{\tau_f} \tag{33}$$

A Stokes number of zero describes a particle which follows the fluid streamline perfectly, while a larger Stokes number describes a particle whose inertial effects dominate its motion. Specifically, the Stokes number of a particle passing through an aerodynamic lens is [38]:

$$St = \frac{\rho_p d_p^2 u_f}{18 d_f \mu_f} \tag{34}$$

where d_f is the lens orifice diameter, as seen in Figure 38.

The optimum Stokes number for particle focusing with aerodynamic lenses is $St = 1$, because while the particles are affected enough by the fluid to be pushed toward the centerline, they still have enough inertia so that when the fluid expands back to its original state after the lens, the particles do not rebound perfectly with it, thus becoming focused closer to the centerline [56, 68, 153]. A particle with Stokes number greater than one will not be effectively focused and instead will collide with the lens, often resulting in particle loss [68].

Considering the nozzle prechamber in the present study, the particle Stokes numbers range from 1 to 413, the smallest particles (5 microns) having the smallest Stokes numbers and the largest particles (100 microns) having the greatest. These Stokes numbers assume the d_f term in equation 34 is equal to the prechamber inner diameter; if lenses were incorporated in that region, d_f would be even smaller and would drive the Stokes numbers even higher. For the present study, the prechamber is the only relevant nozzle zone to consider when evaluating Stokes number for particle focusing because that is the only region where lenses would be implemented. The Stokes numbers in the present nozzle prechamber are not ideal for particle focusing because they are quite high.

It is challenging to focus larger particles because the Stokes number increases as particle diameter increases (see equation 34), which means that larger particles are less prone to adhere to fluid streamlines and be focused. Granted, all the aforementioned

studies except [3] use a lens (or lenses) with 90° angles from the axis, effectively launching particles into a flat wall. As Fernandez de la Mora et al. point out [42], as the angle between the centerline and the lens decreases, higher Stokes numbers can be tolerated without causing particles to cross the centerline too early (and thus disperse). Even if particles have such high Stokes numbers that they collide with such an angled lens, perhaps they will at least rebound toward the nozzle centerline and not adhere to the lens, like in Alhulaifi's nozzle [3]. Alhulaifi incorporated several angled converging-diverging lenses in his cold spray prechamber to successfully focus copper nanoparticles with it [3]. A similar method is suggested by Hoey et al. to focus an aerosol beam [38]. A schematic of Alhulaifi's innovative nozzle is presented in Figure 39.

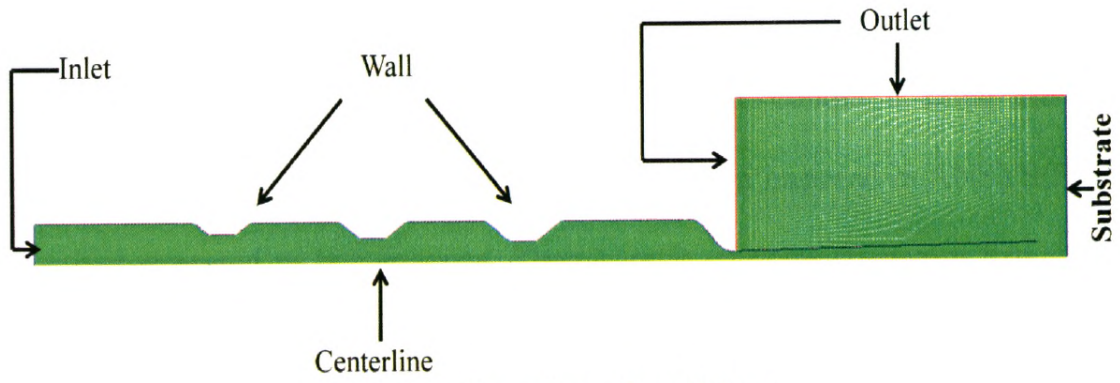

Figure 39: Axisymmetric Schematic of Alhulaifi's Aerodynamic Focusing Nozzle [3]

It is possible to focus wide ranges of particles with aerodynamic lenses by using many lenses, with large lens orifices towards the beginning of the nozzle, and smaller lens orifices towards the end so that large particles can be focused gradually throughout the nozzle [68]. If the large particles approached smaller orifices first, they would simply collide with the lens without being coerced around it. The smaller particles are mostly unaffected by the earliest lenses, but eventually become focused farther downstream by the lenses with small orifices.

The high Stokes numbers of typical cold spray particles make it extremely doubtful that aerodynamic lenses could successfully focus them, but even if they could, there is still another inconvenience to address. With 90° lenses, the jet flow from the first lens requires some distance to adjust back into a fully developed duct flow before reaching the next lens [69]. Although a design like Alhulaifi's with converging-diverging lenses makes for more gradual changes at the wall and therefore less distance required between lenses, particles still need to travel a certain axial distance to be effectively focused. For each additional lens placed in the prechamber, more prechamber length becomes necessary too. If a converging-diverging many-lens system with decreasing lens orifice sizes were created to focus a broad range of particle sizes (diameters 5-100 microns), it would need to be vexingly long. Plus, because there is a total pressure drop across each lens, many lenses would cause a catastrophic total pressure drop in the nozzle.

In short, typical cold spray particles are so large and the driving gas is so fast that the Stokes number is made too large to allow for any meaningful particle focusing inside a cold spray nozzle.

It should be mentioned that Brockmann et al. present results in their patent [11] of achieving a narrow particle beam by using aerodynamic lenses downstream of a cold spray nozzle exit with 15 micron aluminum particles. Since the Stokes numbers of particles at the nozzle exit are generally high due to high particle velocities, the success of this patented device initially appears at odds with the conclusions of the present work, because the present work concludes that aerodynamic lenses are not an effective method of focusing (or minimizing dispersion for) the broad particle sizes relevant to cold spray. Notwithstanding, the apparent disagreement can be harmonized.

The 15 micron particles described in Brockmann et al.'s patent are quite similar in size to the 10 micron particles used in the studies by Deng et al. [21] and Lee et

al. [56] on aerodynamic lenses used under atmospheric outlet conditions. The results in Brockmann et al.'s patent further demonstrate an ability for aerodynamic lenses to focus particles on the order of 10 microns, but do not demonstrate an ability to focus the entire broad range of particle diameters relevant to cold spray, particularly larger particles. Brockmann et al. give no recommendations for gas velocity values to use with their device, but if their device were used with the gas conditions in the present study, their 15 micron aluminum particles would have Stokes numbers ranging from 712 to 1219 depending on which lens was considered, since Brockmann et al.'s invention has three lenses with different orifice diameters. It is clear that Brockmann et al.'s device is not compatible with the gas conditions in the present study, but perhaps the invention is better suited to low-pressure cold spray, which has lower exit velocities [50] and therefore will produce particles with lower Stokes numbers. Even still, Brockmann et al. make no mention of any particle transmission efficiency, and it seems likely that with fairly high Stokes numbers just outside the nozzle exit, some particles would collide with the lens like they did in Deng et al.'s study with high Reynolds numbers and atmospheric outlet conditions [21].

In no way do these comments diminish the accomplishment of Brockmann et al. to focus relatively small (15 microns) particles in cold spray with aerodynamic lenses; the aim of these present comments is simply to point out the impracticality of using aerodynamic lenses to focus a *wide range* of particle diameters (5-100 microns) inside a cold spray nozzle.

Meyer et al. [77] make an observation in line with the conclusions of this section. In their cold spray study, they determine: "Confinement of the particle stream towards the centreline takes place solely due to the interactions with the nozzle wall, thus hardly due to the co-flow fluid entraining the jet and flowing towards the centreline." Fortunately, this chapter presents several nozzle designs which deliberately facilitate collisions in the converging section and prechamber that incline the particles to avoid

the diverging wall downstream. If collisions in the supersonic region can be prevented without aerodynamic lenses, nozzle clogging can be prevented without them as well.

4.3 Modeling Methodology

4.3.1 Boundary Conditions

4.3.1.1 Original Geometry

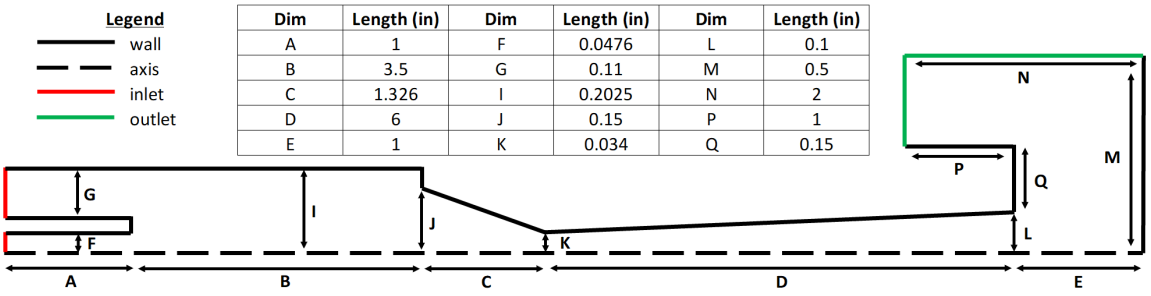

Dim	Length (in)	Dim	Length (in)	Dim	Length (in)
A	1	F	0.0476	L	0.1
B	3.5	G	0.11	M	0.5
C	1.326	I	0.2025	N	2
D	6	J	0.15	P	1
E	1	K	0.034	Q	0.15

Figure 21: Original Nozzle Geometry (Flow Domain)

The first nozzle geometry considered in this chapter is the original nozzle from the three previous chapters which, for convenience, will be referred to as the *original* geometry. The dimensions are provided in Figure 21, which is reproduced from chapter two. The nozzle geometries described hereafter are alterations of the *original*.

4.3.1.2 Long Throat Geometry

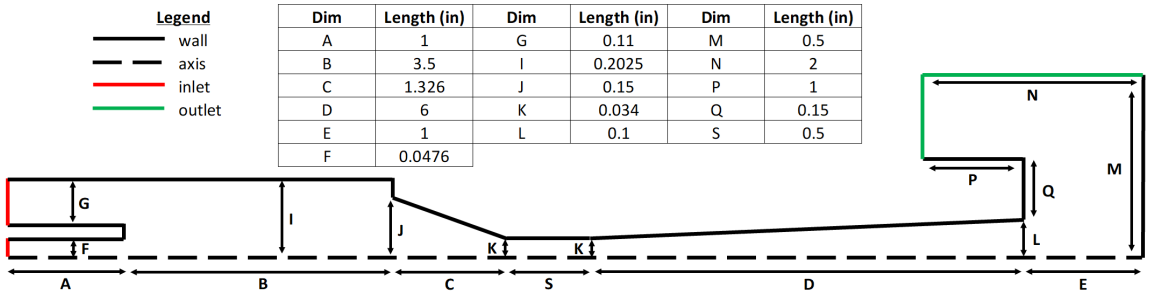

Dim	Length (in)	Dim	Length (in)	Dim	Length (in)
A	1	G	0.11	M	0.5
B	3.5	I	0.2025	N	2
C	1.326	J	0.15	P	1
D	6	K	0.034	Q	0.15
E	1	L	0.1	S	0.5
F	0.0476				

Figure 40: Nozzle Geometry - Long Throat (Flow Domain)

The *long throat* geometry has a throat which is not simply one point on the axis, but rather is a constant-diameter half-inch region. The motivation behind this

geometry is to minimize turbulence near the throat by avoiding a sharp and immediate change at the wall.

4.3.1.3 Flush Geometry

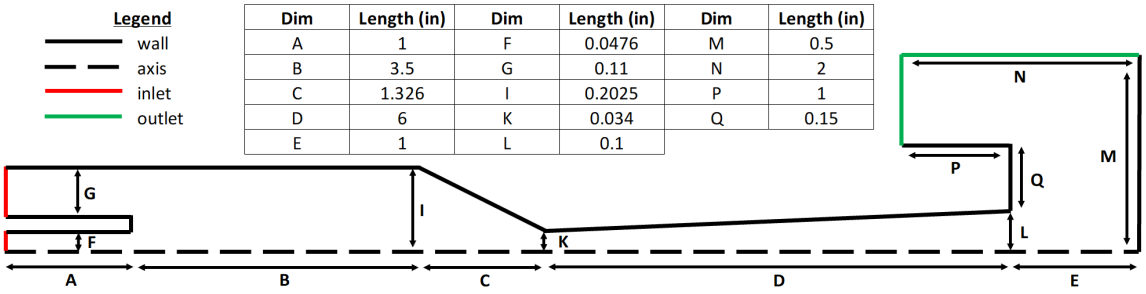

Dim	Length (in)	Dim	Length (in)	Dim	Length (in)
A	1	F	0.0476	M	0.5
B	3.5	G	0.11	N	2
C	1.326	I	0.2025	P	1
D	6	K	0.034	Q	0.15
E	1	L	0.1		

Figure 41: Nozzle Geometry - Flush (Flow Domain)

The *flush* geometry has a converging wall that is flush with the prechamber, in contrast to the *original* geometry which has a vertical "step" wall between the prechamber and converging section. This geometry seeks to prevent particles from rebounding backward upon impact with the "step" wall. Instead, they will be directed downstream and towards the centerline. It should be noted that Huang and Fukanuma used a flush geometry similar to the present one and still required nozzle cooling to avoid clogging [39].

4.3.1.4 Converging Honeycomb Geometry

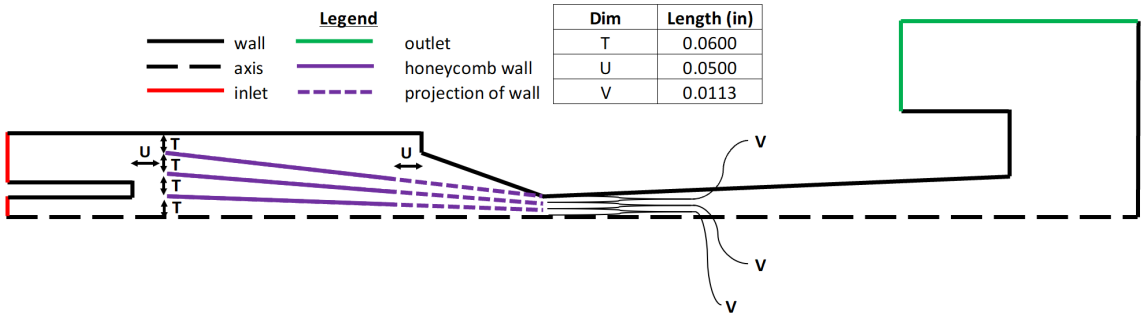

Dim	Length (in)
T	0.0600
U	0.0500
V	0.0113

Figure 42: Nozzle Geometry - Converging Honeycomb (Flow Domain)

The *converging honeycomb* configuration is identical to the *original* geometry, but it has three walls added in the prechamber region. These walls serve to axisymmetrically model the effects of a converging honeycomb particle-focusing device. The design is inspired by a honeycomb flow straightener, a device that has been incorporated in cold spray processes before. When such flow straighteners are used in cold spray studies, however, they are often mentioned only briefly in-text [19, 40] or simply depicted in figures with no in-text description [33, 107]. In one cold spray study, Dupuis does include the dimensions of his honeycomb flow straightener and explains that its purpose is to minimize turbulence [22], but he does not include any analysis on the honeycomb flow straightener's performance.

It should be noted that not all honeycomb flow straighteners are effective at reducing turbulence. In fact, it is possible for honeycomb flow straighteners with non-optimal length-to-diameter ratios to *increase* turbulence rather than reduce it [54]. Because honeycomb flow straighteners are seldom (if ever) evaluated for their effectiveness in cold spray, it is possible that some honeycomb flow straighteners in cold spray are actually promoting dispersion via increased turbulence, rather than preventing it.

Furthermore, honeycomb flow straighteners as described in the aforementioned studies cannot prevent clogging. Assuming they do reduce turbulence, such flow straighteners will indeed produce straight particle tracks, but those tracks will be

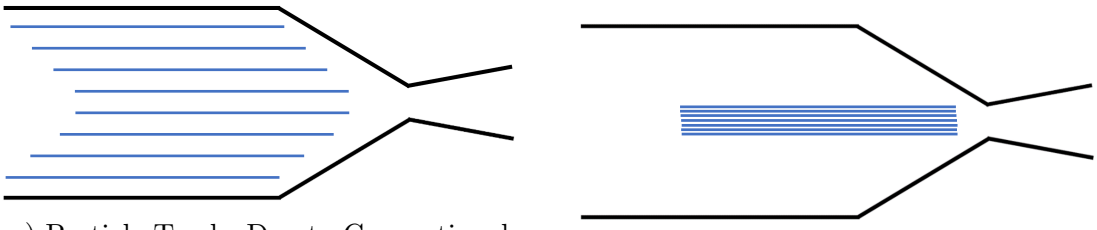

a) Particle Tracks Due to Conventional Honeycomb Flow Straightener

b) Focused Particle Tracks

Figure 43: Comparison of Widely Spread and Focused Particle Tracks

aimed directly at the converging wall, which prepares them to collide with the diverging wall farther downstream. Figure 43 illustrates the difference between particle tracks due to a conventional honeycomb flow straightener and particle tracks that are focused.

The honeycomb device in the *converging honeycomb* geometry employs a converging angle to focus the particle tracks towards the centerline and away from the nozzle wall. The outermost honeycomb wall is aimed at the top of the throat, the next wall is aimed at 2/3 the throat height, and the bottom wall is aimed at 1/3 the throat height. The *converging honeycomb* geometry seeks to produce focused particle tracks as seen in Figure 43b for the sake of avoiding contact with the diverging wall.

4.3.1.5 Long Converging Geometry

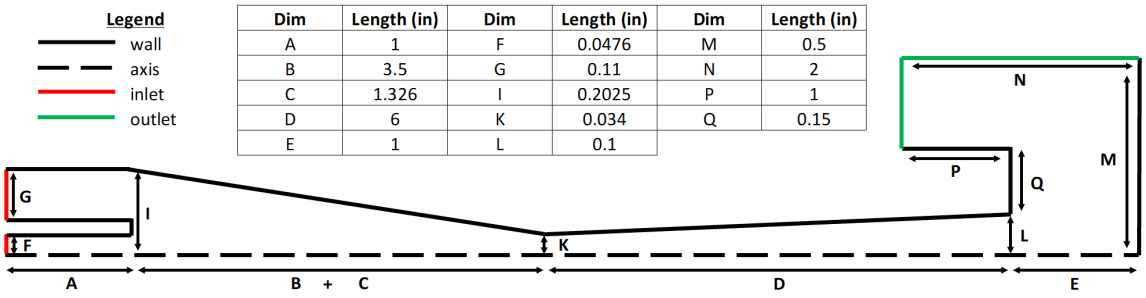

Dim	Length (in)	Dim	Length (in)	Dim	Length (in)
A	1	F	0.0476	M	0.5
B	3.5	G	0.11	N	2
C	1.326	I	0.2025	P	1
D	6	K	0.034	Q	0.15
E	1	L	0.1		

Figure 44: Nozzle Geometry - Long Converging (Flow Domain)

The intention of the *long converging* geometry is to provide a shallow converging angle so that when particles collide with it they rebound with similarly shallow angles. Shallow rebound angles are advantageous because particles are less likely to be directed into the diverging wall, but rather may be able to miss the diverging wall altogether if their trajectory aligns them towards the nozzle exit instead. The convergent length in the *long converging* geometry is equal to the combined length of the prechamber and converging section in the *original* geometry.

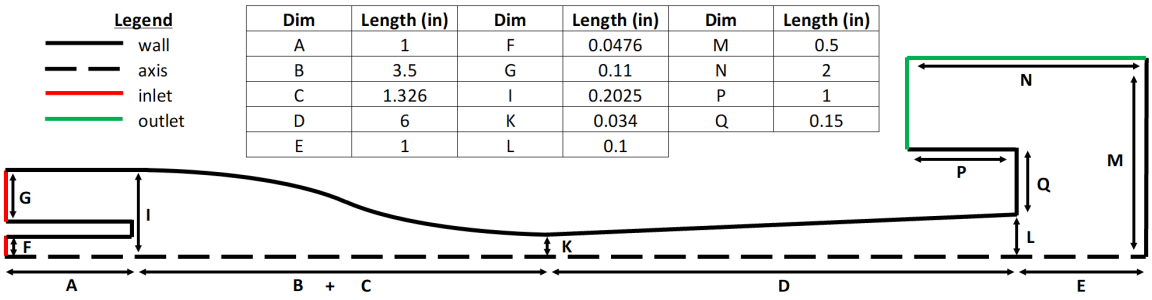

Dim	Length (in)	Dim	Length (in)	Dim	Length (in)
A	1	F	0.0476	M	0.5
B	3.5	G	0.11	N	2
C	1.326	I	0.2025	P	1
D	6	K	0.034	Q	0.15
E	1	L	0.1		

Figure 45: Nozzle Geometry - Smooth (Flow Domain)

4.3.1.6 Smooth Geometry

The *smooth* geometry warrants its name as there are no sharp corners in the prechamber or converging walls - all transitions are "smooth". There are two primary benefits of the *smooth* geometry. First, there will be less turbulence in this nozzle because the smooth transitions facilitate lower levels of flow acceleration in the radial direction. Second, and similar to the *long converging* nozzle, the *smooth* section is as long as the *original* prechamber and converging section combined, which facilitates shallow rebound angles and therefore a lower likelihood of diverging section collisions.

The smooth wall was produced by a cosine curve connecting the annulus and diverging walls. Equation 35 provides the radial cordinate of the wall (r_{wall}) as a function of nozzle length (x):

$$r_{wall}(x) = \frac{I-K}{2} cos(0.65x) + \frac{I+K}{2} \tag{35}$$

where I and K are the nozzle dimensions provided in Figure 45 and 0.65 is a constant that depends on the desired length of the wall curve. In the present study, 68 line segments were connected to 69 points so that each change in wall angle was small and the wall was sufficiently "smooth".

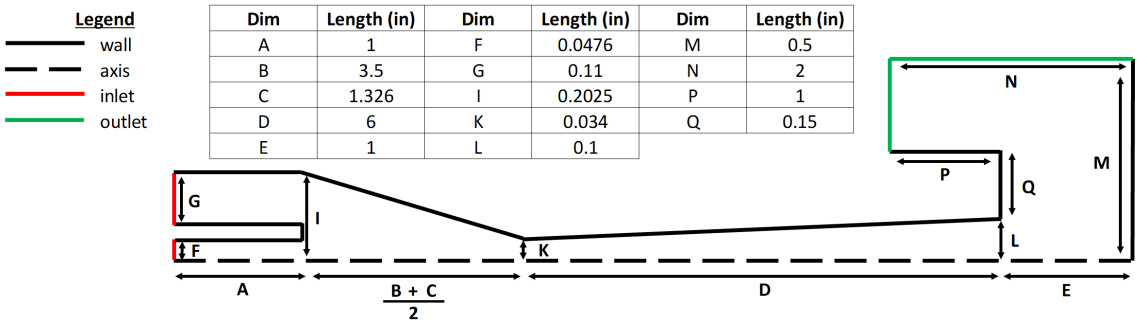

Figure 46: Nozzle Geometry - ½ Long Converging (Flow Domain)

4.3.1.7 ½ Long Converging Geometry

The *½ long converging* geometry is a modification of the *long converging* geometry, with the convergent length being shortened by a factor of two. This geometry was investigated to determine how the converging angle and length influence the amount of particle-wall collisions by comparing the results of the *½ long converging* and *long converging* geometries.

4.3.1.8 ½ Smooth Geometry

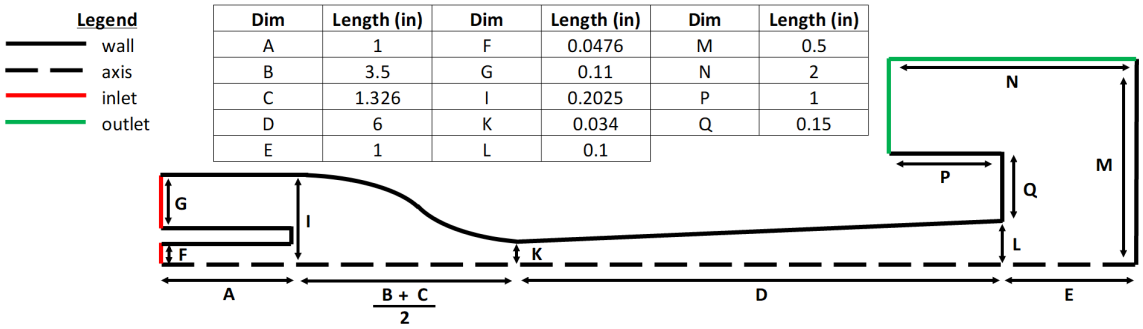

Figure 47: Nozzle Geometry - ½ Smooth (Flow Domain)

The *½ smooth* geometry was modeled to compare the results to the full-length *smooth* geometry. This comparison helps in comprehending how the length and angle of the smooth section affects particle collisions downstream. The radial coordinate of

the smoothly converging wall in the ½ *smooth* geometry was determined according to equation 36:

$$r_{wall}(x) = \frac{I-K}{2} cos(1.3x) + \frac{I+K}{2} \tag{36}$$

where I and K are the dimensions provided in Figure 47 and the constant 1.3 sets the converging section length properly. Shortening the convergent length by a factor of two requires the constant 1.3 to be double that which was used for the *smooth* geometry (0.65) in equation 35.

4.3.1.9 Boundary Conditions for All Geometries

The boundary conditions for all the geometries investigated in this chapter were similar. Both inlets were set to 673 K and 4 MPa, and the outlet was set to zero gauge pressure and 293 K (atmospheric conditions). Particles were modeled to escape the domain upon contacting the substrate wall or the atmospheric outlet.

The internal walls (except those of the feeder tube) in the geometries of this chapter were equipped with the UDF described in chapter two, which records the axial location, particle size, and CVR of each particle-wall collision. The coefficient of restitution was varied from unity to 0.2 to comprehend how the rebound characteristics affect dispersion and the prediction of clogging in each unique geometry.

4.3.2 Mesh Descriptions

Because each geometry is different, the mesh requirements were different for each geometry. All configurations were meshed with a variety of cell sizes in each zone to find how fine of a mesh was required for each zone of each geometry. A mesh-independent solution was achieved with the meshes described in Tables 8 and 9.

Table 8 provides the cell size for each zone of each geometry, while Table 9 provides the total cell count of each mesh along with the relevant yplus values. Three layers of thin cells were applied to the nozzle walls in all geometries to capture boundary

Table 8: Mesh Specifications Based on Zone Name for Each Geometry

	Cell Size (mm) for Each Geometry			
Zone	Original	Long Throat	Flush	Converging Honeycomb
inlets	0.2	0.2	0.2	0.2
prechamber	0.2	0.2	0.2	0.1
converging	0.2	0.2	0.2	0.15
throat	∼	0.07	∼	∼
diverging	0.08	0.07	0.08	0.08
standoff	0.08	0.07	0.08	0.08
atmosphere	0.4	0.4	0.4	0.4
Zone	Long Converging	Smooth	1/2 Long Converging	1/2 Smooth
inlets	0.2	0.2	0.2	0.2
prechamber	∼	∼	∼	∼
converging	0.09	0.09	0.09	0.09
throat	∼	∼	∼	∼
diverging	0.08	0.08	0.06	0.06
standoff	0.08	0.08	0.06	0.06
atmosphere	0.4	0.4	0.4	0.4

Table 9: Mesh Cell Count and Yplus Values for Each Geometry

Geometry	Cells	Yplus Minimum	Yplus Throat
Original	75,404	0.2	4.25
Long Throat	91,757	0.15	4.0
Flush	76,800	0.15	4.25
Converging Honeycomb	109,815	0.05	3.5
Long Converging	108,385	0.075	2.1
Smooth	108,271	0.1	1.9
1/2 Long Converging	119,886	0.125	3.25
1/2 Smooth	120,411	0.06	2.0

layer effects. In all but the *converging honeycomb* configuration, the maximum yplus occurred at the throat. The *converging honeycomb* geometry resulted in a maximum yplus value of 13 at the honeycomb wall boundaries, which were not treated with thin cell layers. It should be noted that the *original* configuration in this chapter was

meshed differently than it was in chapters two and three, specifically in the diverging and standoff regions.

4.3.3 Gas Phase Modeling

The same solver and discretization schemes used in the three previous chapters were employed in this chapter as well. The density-based implicit solver was required to capture the compressible nature of the flow, while the first-order upwind spatial discretization scheme was used to bring the solutions to a sufficient level of convergence. The k-ϵ realizable turbulence model was used to predict turbulent effects, as was the case in the previous chapters.

Helium was used as the driving gas, and its density varied according to the ideal gas law. The thermal conductivity and viscosity of the gaseous helium varied with respect to temperature according to equations 4 and 5.

4.3.4 Discrete Phase Modeling

Similar to the previous chapters, Lagrangian one-way coupling was used to track the particles. The Discrete Random Walk model stochastically amended the particle trajectories due to turbulent fluctuations.

The same copper-nickel alloy particle material from chapters two and three was used for the discrete phase in this chapter, with a density of 8940 kg/m^3 and a specific heat capacity of 380 J/kg-K. Particle diameters were assigned uniformly and randomly between five and 100 microns so that conclusions about particle bonding could be made based on diameter.

Unless otherwise specified, ten injections of 50,000 particles each were employed per simulation, totaling to 500,000 particles being injected per simulation. Some geometries prevented collisions so effectively that they required more particles to obtain collision data. In similar fashion to chapter two, total pressure oscillations at the feeder tube inlet were imposed to promote particle dispersion. The pressure waves

consisted of 50 kPa amplitudes and 50 Hz frequencies, and the injections occurred during the time interval from 0.035 sec to 0.065 sec in accordance with the timing displayed in Figure 27.

To model an injection, particles were generated in the 2-D axisymmetric domain as if they were occupying a 3-D space with uniform position density. This was achieved by generating particles with increased likelihood away from the centerline by a factor of the square root of radial position in the axisymmetric model.

A significant difference between the injections in the present chapter and those described previously is a rather extreme particle initial trajectory angle. When a particle initial velocity of zero was employed in this work, some geometries were predicted by the models to result in zero clogging. Such a prediction is encouraging because it not only shows an improvement over the *original* configuration, which is the same geometry from chapters two and three that predicted clogging, but it also might indicate that clogging is preventable simply with the proper geometry. As a means to determine which geometry performs best at minimizing diverging section collisions, it was necessary to inject particles with large enough initial trajectory angles to force collisions in the diverging section. Thus with the exception of the first set of simulations, which employ particle initial velocities of zero, each injection in this chapter consisted of particles with initial velocity magnitudes of 25 m/s (equal to the feeder tube flow velocity) and initial trajectory angles ranging between zero and 60°.

4.4 Results

4.4.1 Steady-State Models

The steady-state centerline flow velocities of each geometry are compared in Figure 48. Because the diverging length is the same for all geometries, all the nozzles result in similar exit velocities, with the profiles of the ½ *smooth* and ½ *long converging*

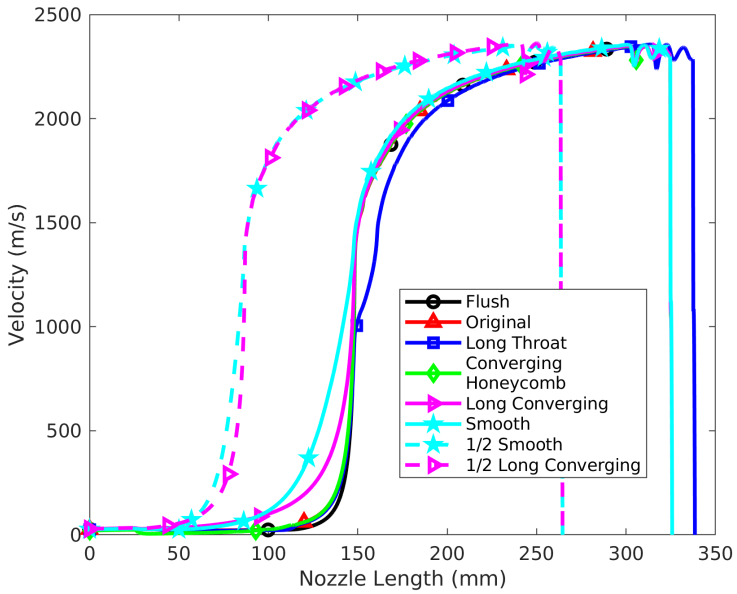

Figure 48: Centerline Flow Velocity vs Nozzle Length of Each Geometry

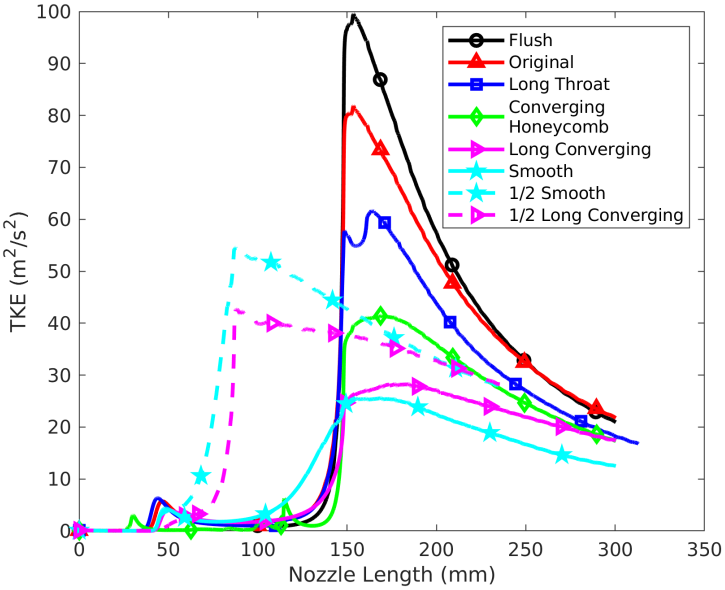

Figure 49: Centerline TKE vs Nozzle Length of Each Geometry

geometries being shorter due to those nozzles being shorter. Because the gas velocities are similar for each geometry, the particle velocities should likewise be similar at the substrate and produce comparable coating characteristics.

The *smooth* and *long converging* geometries produce higher velocities prior to the throat than the others because the cross-sectional area reduces in those geometries prior to the others. The *long throat* geometry fosters a velocity that increases after the others because of the constant-diameter throat which facilitates a later increase in velocity. The Mach diamonds and bow shock occur later in the *long throat* geometry because of the additional length in the throat.

Because turbulence is known to be a significant factor in particle dispersion, Figure 49 compares the axial TKE in each geometry. All configurations produce a maximum TKE value near the throat. The *flush* geometry has the largest peak, while the *long converging* and *smooth* geometries produce the smallest amount of turbulence.

4.4.2 Transient Models

The simulations with injections consisting of zero initial particle velocity ($v_{p,0}$) and normal (e_n) and tangential (e_t) coefficients of restitution of unity resulted in the particle-wall collisions displayed in Figure 50. It is observed that the first four geometries produce major clogging, while the other four produce less.

The *long converging* and *smooth* geometries were initially injected with 500,000 total particles each (which was the case for all other simulations), but because neither configuration predicted clogging with 500,000 particles, another simulation was run with 5,000,000 particles for both geometries. The results from the 5,000,000 particle injection are presented in Figure 50. The *long converging* configuration still did not produce particles that clogged, while the *smooth* geometry produced exactly seven clogging particles out of 5,000,000.

Table 10 ranks the geometries according to how well they prevented particle-wall reflections and bonding, respectively, with the injection employing zero initial particle velocity and a coefficient of restitution of unity. Each geometry is ranked by percent

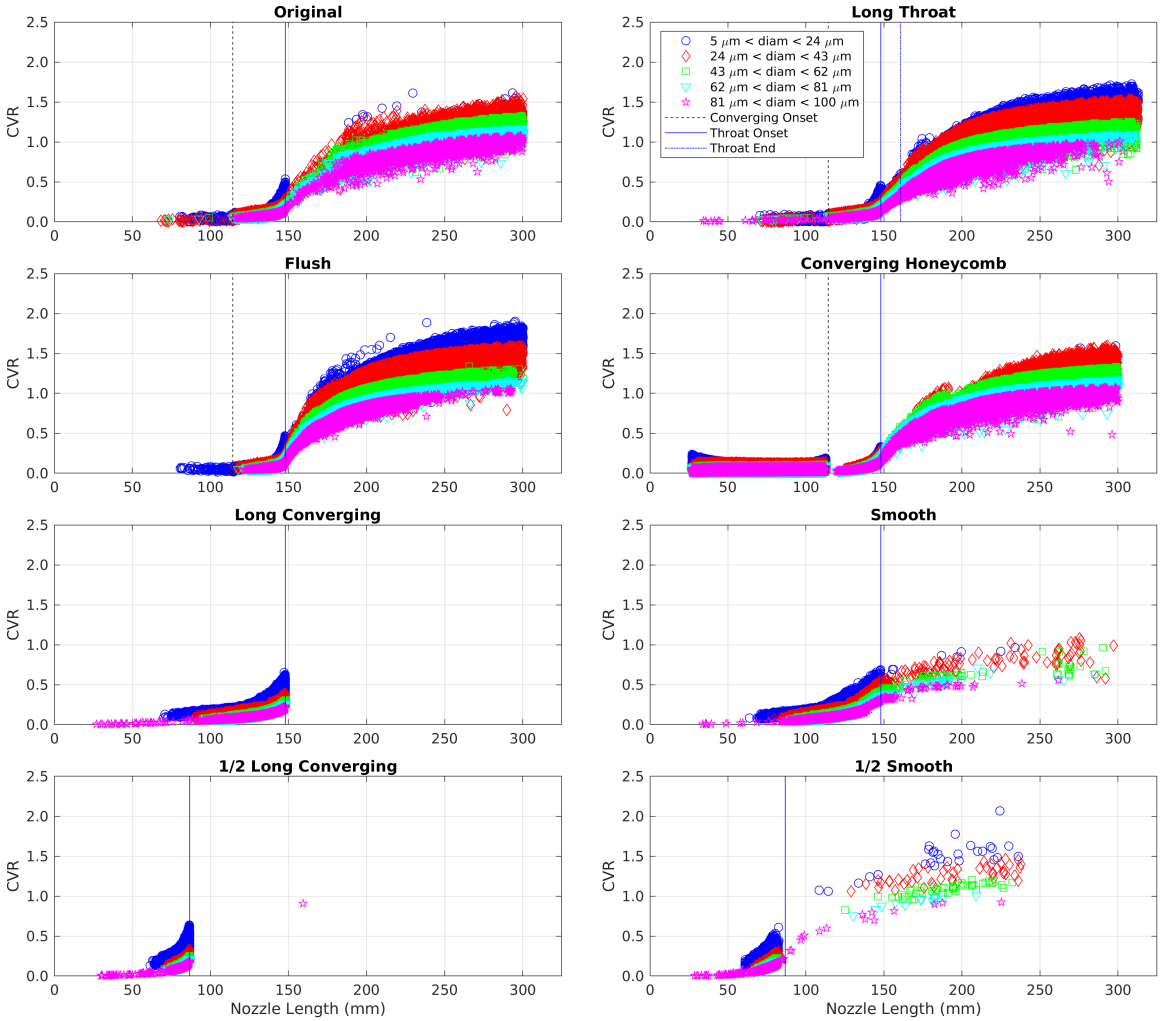

Figure 50: CVR vs Nozzle Length of Each Geometry
$v_{p,0} = 0$, $e_n = 1.0$

because not all geometries were injected with the same number of particles (the *long converging* and *smooth* configurations received more).

The *long converging* geometry outperformed the others both in terms of reflecting and bonding particles. Minimizing the number of reflections is not the primary goal of this work, but the reflection data are provided because it is still valuable to know how much the particles bounce inside the nozzle. The *long converging* and *smooth* geometries, along with their shortened versions, far outperformed the others in terms of preventing bonding inside the nozzle.

Table 10: Ranked Particle-Wall Collisions for Each Geometry
$v_{p,0} = 0$ m/s, $e_n = 1.0$

Rank	Geometry	% Particles Reflecting
(1)	Long Converging	3
(2)	1/2 Smooth	8
(3)	1/2 Long Converging	18
(4)	Smooth	20
(5)	Original	43
(6)	Flush	75
(7)	Long Throat	77
(8)	Converging Honeycomb	243

Rank	Geometry	% Particles Bonding
(1)	Long Converging	0
(2)	1/2 Long Converging	0
(3)	Smooth	0.00014
(4)	1/2 Smooth	0.0224
(5)	Original	3
(6)	Long Throat	9
(7)	Converging Honeycomb	9
(8)	Flush	13

It should be noted from Table 10 that the *converging honeycomb* geometry causes, on average, each particle to reflect off the nozzle wall 2.4 times. The *converging honeycomb* geometry facilitates far more reflecting collisions than the other geometries because that geometry deliberately facilitates many collisions to tightly focus the particles, which could result in rapid wear of the honeycomb component.

Because the models with $v_{p,0} = 0$ did not produce clogging for all geometries and only a small amount for the *smooth* geometry, it was desirable to investigate how each geometry would handle a steeper particle initial trajectory angle with an initial particle velocity. Therefore in the next injection, the initial velocity magnitude of each particle was set to the feeder tube flow velocity (25 m/s) and the particle initial trajectory angles ($\alpha_{p,0}$) were assigned randomly and uniformly between zero and 60°. With each geometry, transient simulations were conducted with e_n ranging from 1.0

to 0.2 while the tangential coefficient of restitution (e_t) was maintained at unity for all simulations. Since the coefficient of restitution inside the cold spray nozzle is not well-known, it is necessary to obtain results for a wide range of e_n so that the present results are relevant for future studies when more progress is made on ascertaining the coefficients of restitution.

The resulting particle-wall collisions for each geometry from the transient models with $v_{p,0} = 25$ m/s, $\alpha_{p,0} = 0$-60°, and $e_n = 1.0$ are provided in Figure 51. It is observed that all configurations produce collisions that result in bonding.

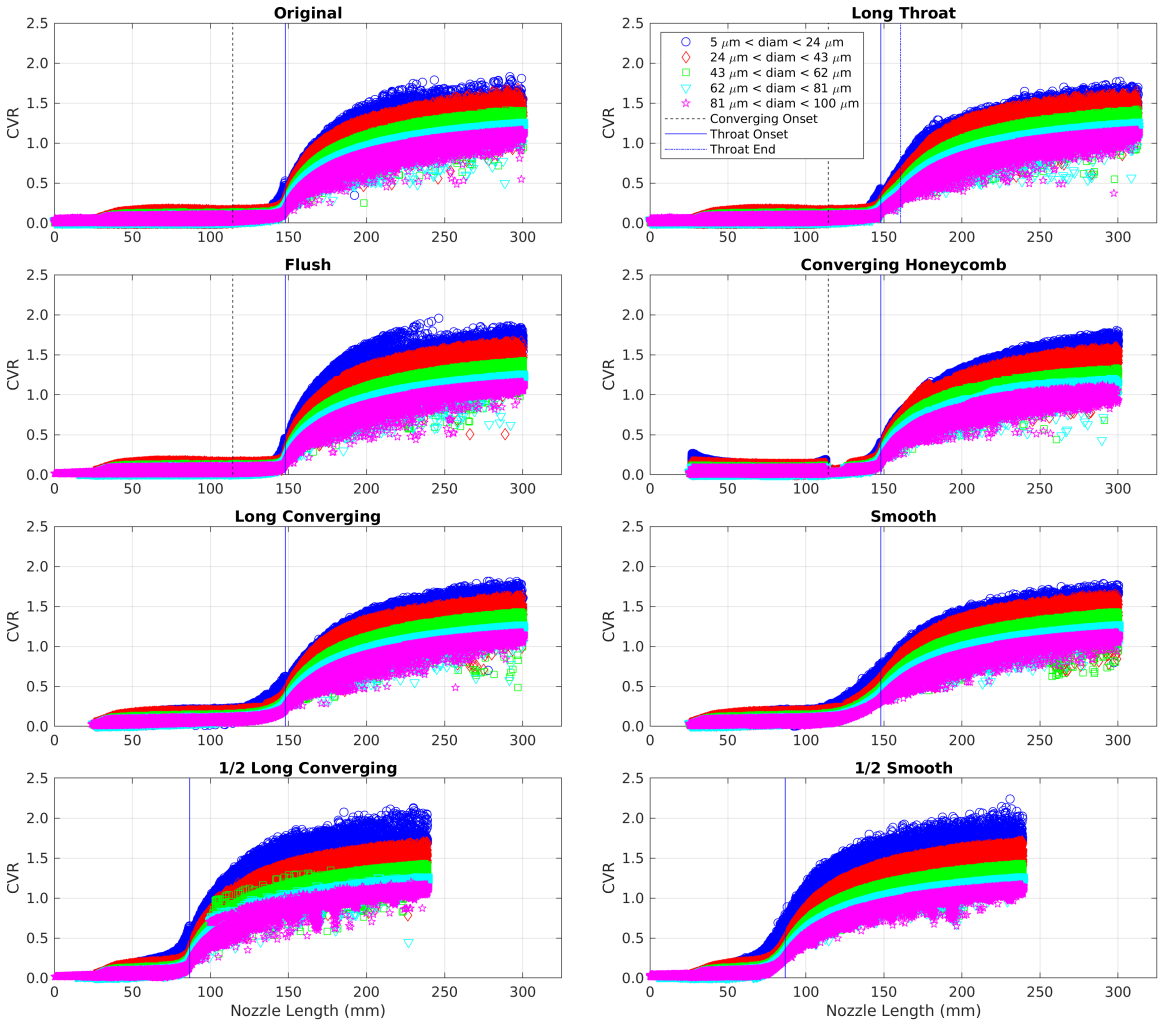

Figure 51: CVR vs Nozzle Length of Each Geometry
$v_{p,0} = 25$ m/s, $\alpha_{p,0} = 0$-60°, $e_n = 1.0$

As e_n decreases, fewer collisions and adhesions occur with each geometry. Tables 11 and 12 summarize the results of all the simulations with $v_{p,0}$ = 25 m/s, $\alpha_{p,0}$ = 0-60°, and various coefficients of restitution. For each value of e_n, each geometry is "scored" according to how effectively it prevented collisions. A score of 1 is earned by successfully preventing collisions better than the other geometries, while a higher score is merited by performing worse than others (allowing more collisions to occur). If the same number of collisions occurred between two geometries for a certain e_n, those geometries earned the same score. The "score sums" are the sum of the scores for all values of e_n for each respective geometry. The "overall rank" compares the "score sums" and ranks them according to which geometries performed best, the best geometries having the lowest score, and the worst geometries having the largest. If geometries received the same "score sum", they both received the same "overall rank". The geometries with the lowest "overall rank" performed best across all values of e_n at preventing collisions. The "total" collisions column was not used to compute the overall rank.

As Table 11 shows, the two nozzles that facilitated the least particle-wall reflections were the ½ *long converging* and ½ *smooth* geometries, but this is likely because they are shorter and therefore the particles have less nozzle length to bounce off. The *converging honeycomb* geometry facilitated the most collisions because the honeycomb section captures nearly all the particles and directs them via reflecting collisions.

Table 12 presents the number of bonding particles in each geometry at each coefficient of restitution. The *long converging* and *original* geometries tied for best overall rank at preventing bonding inside the nozzle. It is surprising that the *original* geometry performed so well with $v_{p,0}$ = 25 m/s and $\alpha_{p,0}$ = 0-60° because it performed comparably poorly with $v_{p,0}$ = 0 m/s (receiving a rank of five in Table 10). The second-best overall rank for preventing bonding was earned by the *converging honeycomb* and *smooth* configurations.

Table 11: Reflecting Particle-Wall Collisions and Score for Each Geometry
$v_{p,0}$ = 25, $\alpha_{p,0}$ = 0-60°
Low score represents good performance, high score represents poor performance

	e_n=1.0	e_n=0.8	e_n=0.6	e_n=0.4	e_n=0.2		
Geometry	Reflecting Collisions					Total	
Original.	2.95M	1.64M	1.2M	.96M	.81M	7.56M	
Long Throat.	3.3M	1.75M	1.29M	1.01M	.83M	8.17M	
Flush.	3.58M	1.61M	1.17M	.9M	.75M	8.01M	
Converging Honeycomb.	6.28M	4.08M	2.3M	1.52M	1.09M	15.28M	
Long Converging.	4.M	1.83M	1.18M	.85M	.64M	8.5M	
Smooth.	4.4M	1.9M	1.25M	.86M	.57M	8.98M	
1/2 Long Converging.	3.41M	1.57M	1.11M	.75M	.56M	7.4M	
1/2 Smooth.	3.82M	1.68M	1.17M	.83M	.55M	8.05M	
Geometry	Scores					Score Sums	Overall Rank
Original.	1	3	5	6	6	21	4
Long Throat.	2	5	7	7	7	28	7
Flush.	4	2	3	5	5	19	3
Converging Honeycomb.	8	8	8	8	8	40	8
Long Converging.	6	6	4	3	4	23	5
Smooth.	7	7	6	4	3	27	6
1/2 Long Converging.	3	1	1	1	2	8	1
1/2 Smooth.	5	4	2	2	1	14	2

The results in Tables 11 and 12 should be qualified because they are relevant to particle initial trajectory angles up to 60°, which is unrealistically high. The bonding data in Table 12 still demonstrate how the coefficient of restitution affects clogging and how each geometry performs when particles are highly dispersed. The scores vary fairly significantly between the different values of e_n, which indicates that the

Table 12: Bonding Particle-Wall Collisions and Score for Each Geometry
$v_{p,0}$ = 25 m/s, $\alpha_{p,0}$ = 0-60°
Low score represents good performance, high score represents poor performance

	e_n=1.0	e_n=0.8	e_n=0.6	e_n=0.4	e_n=0.2		
Geometry	Bonding Collisions					Total	
Original.	79,285	22,087	15,872	876	0	118,120	
Long Throat.	84,997	28,420	16,046	7,661	129	137,253	
Flush.	136,782	51,351	40,557	29,863	2,786	261,339	
Converging Honeycomb.	47,745	60,371	1,281	0	0	109,397	
Long Converging.	121,723	32,549	850	0	0	155,122	
Smooth.	130,049	27,955	3,479	5	0	161,488	
1/2 Long Converging.	148,902	34,445	40,861	4,512	7	228,727	
1/2 Smooth.	156,812	42,415	31,426	16,104	4,400	251,157	
Geometry	Scores					Score Sums	Overall Rank
Original.	2	1	4	3	1	11	1
Long Throat.	3	3	5	5	3	19	3
Flush.	6	7	7	7	4	31	5
Converging Honeycomb.	1	8	2	1	1	13	2
Long Converging.	4	4	1	1	1	11	1
Smooth.	5	2	3	2	1	13	2
1/2 Long Converging.	7	5	8	4	2	26	4
1/2 Smooth.	8	6	6	6	5	31	5

amount of clogging in each geometry depends strongly on the value of e_n (whatever it is).

When comparing the results of Table 10 with those of Table 12, it is also evident that the degree of clogging in each geometry is highly dependent on the particle initial trajectory angle, especially in the *original* geometry, which performed best (tied with *long converging*) with a steep angle and fifth with no angle.

With neither the particle initial trajectory angle nor the internal coefficient of restitution being thoroughly studied topics in cold spray, it is challenging to make a confident claim that one geometry performs better than another for all cold spray scenarios. The results in the present work, however, indicate compellingly that the *long converging* geometry is most effective at preventing clogging in most (if not all) cold spray scenarios. The *long converging* geometry was most successful at preventing bonding with both injection methods with zero initial velocity (Table 10) and a nonzero velocity with a steep trajectory angle (Table 12). The *smooth* geometry performed well for the various injection methods and values of e_n too, but still slightly worse than the *long converging* configuration did.

Conveniently, the *long converging* geometry is also one of the easiest to manufacture of the geometries considered because it incorporates a flat wall in all the nozzle zones. Although at low coefficients of restitution the *converging honeycomb* geometry performs extremely well, it is by far the hardest to manufacture of those considered in this study. Plus, since it facilitates an extremely high number of collisions, the honeycomb component could get worn out over time, making it potentially impractical for use in an experiment.

Although clogging was predicted to occur in the *long converging* geometry for some values of e_n with a steep particle initial trajectory angle, it should be pointed out that a 60° angle is unrealistically high and that the actual trajectories are probably mostly axial. The initial trajectory angle only describes the particle's initial trajectory *inside the feeder tube*. Once the particle leaves the feeder tube and enters the nozzle domain, the trajectory changes due to a myriad of factors, but the particle initial trajectory angle only refers to its initial trajectory inside the feeder tube. When an axial initial particle trajectory was employed, which is likely a more realistic conjecture, absolutely no clogging was predicted in the *long converging* geometry (see Table 10).

It may be that, in experiments, the *long converging* geometry would completely prevent clogging, even with fines. In light its promising ability to prevent bonding inside the nozzle, the *long converging* geometry is recommended for preventing nozzle clogging in cold spray. Experiments should be conducted to evaluate this recommendation since it is based entirely on computational models. The experiments should not shorten the converging section length, because the *½ long converging* geometry performed significantly worse than the full-length *long converging* geometry.

4.5 Conclusion

Because nozzle cooling cannot entirely mitigate clogging with small particles, alternative methods are necessary. An altered internal nozzle geometry can intentionally facilitate collisions upstream of the throat which direct the particles away from the diverging wall as a means to prevent collisions where clogging typically occurs. If no collisions occur in the diverging section, clogging cannot transpire either.

In this study, several novel nozzle geometries were considered and evaluated for their effectiveness at preventing bonding inside the nozzle. The geometry with a long conical converging section (termed the *long converging* geometry) was deemed most effective at preventing bonding for all considered particle initial trajectory angles and across all considered values of the normal coefficient of restitution. The *original* geometry, which the *long converging* geometry is an alteration of, was found to produce clogging in experiments [109] and in the models of the present study. In contrast to the *original* geometry, when particles were injected with perfectly axial trajectories inside the feeder tube, the *long converging* geometry was predicted to produce absolutely zero clogging.

The particular process parameters will determine the particle initial trajectory angles in the feeder tube, which will (in part) determine how much the particles will disperse and therefore potentially clog. Although the particles probably do not travel

perfectly axially in the feeder tube, they likely have shallow trajectory angles because the straight feeder tube does not facilitate much radial motion. Because it is hard to predict the particle trajectory angle inside the feeder tube, it is difficult to make a precise and confident claim regarding the effectiveness of the *long converging* nozzle geometry based on modeling alone. Experiments are necessary to determine whether the *long converging* geometry fully prevents clogging, but the modeling results from this study show promise for its success. When these experiments are conducted, it is important that the converging length is not shortened, because another similar geometry with half the convergent length was also modeled and performed considerably worse at preventing clogging than the full-length *long converging* geometry.

CHAPTER 5

OVERARCHING CONCLUSIONS

5.1 Conclusions

The present work consists of four individual computational studies, separated by chapter, which cumulatively aim to mitigate and analyze the problem of nozzle clogging in cold spray. The first study investigated supercritical CO_2 as a means to cool the nozzle. Nozzle cooling with water is common practice in the field of cold spray because it prevents clogging in many otherwise clogging-prone scenarios. There are, however, certain combinations of materials and process parameters that still clog with water cooling. Using supercritical CO_2 instead of water may provide the additional cooling required to spray highly clogging-prone materials without bonding to the nozzle wall.

The primary thrust of the first chapter was to determine whether the particles are maligned by cooling. Although the bulk gas flow velocity and temperature were found to decrease, the particles remained almost totally unaffected. Experiments are required to confirm this model prediction, but the CFD shows promise for the ability to maintain high particle velocity and temperature while cooling the nozzle considerably with CO_2.

The experiments in this study demonstrate that small particles (fines) cannot be reliably prevented from clogging even with CO_2 cooling. When stainless steel powder was not sieved to remove fines, clogging occurred while cooling, but when the powder was sieved, the clogging ceased. Because nozzle cooling cannot prevent clogging with fines, other methods of clogging prevention must be employed to prevent clogging for

all process parameters. Nonetheless, CO_2 provides a greater cooling capacity than water, which makes it a worthwhile method of clogging prevention.

The second chapter was dedicated to determining how pressure oscillations in the feeder tube, if present, would affect clogging. This numerical study was motivated by an inability to otherwise predict the clogging observed in experiments. The amplitude of these pressure oscillations greatly influences the degree of clogging - the larger the pressure wave amplitude, the greater the degree of clogging. The frequency of these pressure waves has seemingly little effect on clogging.

Because pressure oscillations were found to have such a significant effect on clogging, it was hypothesized in chapter three that the mass flow pulsations from the rotating metering wheel cyclically blocking and releasing the driving gas might cause enough particle dispersion to produce clogging. This hypothesis was negatively proven, as it was found that the flow is not sufficiently disturbed so as to disperse particles significantly.

On the other hand, particles with as small as a 10° initial trajectory angle in the feeder tube resulted in substantial clogging downstream. This study highlights how sensitive clogging is to the particle initial trajectory angle; when particles travel perfectly axially, absolutely zero clogging is predicted, but when an angle of only 10° is employed, major clogging is predicted.

Since the cooling method cannot prevent clogging with fines, it is desirable to explore methods that might be able to. In chapter four, several novel nozzle internal geometries were investigated for their effectiveness at preventing particle-wall collisions with the diverging wall. Nozzle clogging only occurs in the diverging section, so if collisions can be entirely prevented there, clogging will not occur.

Of the geometries considered, the nozzle with a long conical converging section was deemed most effective at preventing clogging. This *long converging* geometry performed best with both shallow and steep particle initial trajectory angles, and

across all considered values of coefficient of restitution. The *long converging* geometry might completely prevent clogging. Based exclusively on CFD models, however, it is challenging to make a confident claim as to whether the *long converging* geometry will entirely prevent clogging. As the results of chapter three demonstrate, clogging is acutely exacerbated by the particle initial trajectory angle, which is probably dependent on both the process configuration and the process parameters.

5.2 Future Work

Experiments should be conducted to determine what new process parameters can be reached with clogging-prone powder materials using CO_2 cooling rather than water cooling. It would be valuable to learn the maximum allowable applicator temperature for each clogging-prone powder, along with the minimum particle diameter that can be successfully prevented from clogging with CO_2 cooling. Experiments would also be valuable in determining whether CO_2 cooling allows for the switch from helium to nitrogen driving gas for certain process parameters and powder materials. The coatings produced while using CO_2 cooling should be evaluated to ensure the deposit is not compromised. In future design iterations, the cooling collar should cover the entire span of the diverging section rather than leaving an inch uncooled. The uncooled region becomes relatively warm due to viscous heating which may facilitate bonding in that region. Additionally, the next collar design should exhaust the gaseous and solid CO_2 radially rather than axially to avoid affecting the substrate either by cooling it or bombarding it with dry ice, and to avoid cooling the nozzle near the inlets and thus lowering the gas velocity unnecessarily.

Although this would be a challenging experiment to conduct, if measurements of feeder tube motion during the spray process could be taken, it would illuminate whether feeder tube oscillations are present, which would be valuable because it was found in chapter two that, if present, such oscillations can cause clogging. Feeder tube

oscillations could be caused by vibrations in the cold spray system or fluid-structure interactions.

To predict clogging more accurately, future models should account for the nozzle wall temperature in their bonding criteria. The wettability of powder materials on the inside of a tungsten carbide nozzle should be further studied so that clogging predictions can be developed. Relatedly, the coefficient of restitution (and impact phenomena in general) between a cold spray particle and the inner nozzle wall should be investigated.

Another challenging but valuable study would be an experimental measurement of particle trajectory angles inside the feeder tube. Because clogging was found to be so sensitive to this angle in chapter three, such a study would help to comprehend the reasons for nozzle clogging.

It is of chief importance that experiments be conducted with the *long converging* geometry described in chapter four because that nozzle geometry might completely prevent clogging. It is crucial that the converging length is not shortened during these experiments because a shorter version of the *long converging* geometry was also modeled and was found to be comparably ineffective at preventing clogging.

BIBLIOGRAPHY

[1] Al-Hamdani, K.S., Murray, J.W., Hussain, T., Kennedy, A., and Clare, A.T. Cold sprayed metal-ceramic coatings using satellited powders. *Materials Letters 198* (2017), 184 – 187.

[2] AL-Mangour, Bandar, Vo, Phuong, Mongrain, Rosaire, Irissou, Eric, and Yue, Stephen. Effect of heat treatment on the microstructure and mechanical properties of stainless steel 316L coatings produced by cold spray for biomedical applications. *Journal of Thermal Spray Technology 23*, 4 (Apr 2014), 641–652.

[3] Alhulaifi, Abdulaziz. *Numerical and Experimental Characterization of the Cold Spray Process for Spraying Nano Particle Powders*. PhD thesis, South Dakota School of Mines and Technology, Rapid City, South Dakota, 2011.

[4] Alkhimov, A. P., Kosarev, V. F., and Klinkov, S. V. The features of cold spray nozzle design. *Journal of Thermal Spray Technology 10*, 2 (Jun 2001), 375–381.

[5] Anderson, John D. *Modern Compressible Flow: With Historical Perspective*, 3 ed. McGraw Hill Education (India), 2003.

[6] Assadi, H., Schmidt, T., Richter, H., Kliemann, J.-O., Binder, K., Gärtner, F., Klassen, T., and Kreye, H. On parameter selection in cold spraying. *Journal of Thermal Spray Technology 20*, 6 (Dec 2011), 1161–1176.

[7] Assadi, Hamid, Gärtner, Frank, Stoltenhoff, Thorsten, and Kreye, Heinrich. Bonding mechanism in cold gas spraying. *Acta Materialia 51*, 15 (2003), 4379 – 4394.

[8] Bhattacharya, Sourin. *Fluid Mechanics of Micro Cold Spray Direct Write Process*. PhD thesis, North Dakota State University, Fargo, North Dakota, 10 2012.

[9] Bhattacharya, Sourin, Lutfurakhmanov, Artur, Hoey, Justin M., Swenson, Orven F., Mahmud, Zakaria, and Akhatov, Iskander S. Aerosol flow through a converging-diverging micro-nozzle. *Nonlinear Engineering 2*, 3-4 (2013), 103 – 112.

[10] Binder, K., Gottschalk, J., Kollenda, M., Gärtner, F., and Klassen, T. Influence of impact angle and gas temperature on mechanical properties of titanium cold spray deposits. *Journal of Thermal Spray Technology 20*, 1 (Jan 2011), 234–242.

[11] Brockmann, John E., Torczynski, John R., Dykhuizen, Ronald C., Neiser, Richard A., and Smith, Mark F. Aerodynamic beam generator for large particles, 2002. Research Org.: SANDIA CORP.

[12] Brown, S., Martynov, S., and Mahgerefteh, H. Modelling heat transfer in flashing CO_2 fluid upon rapid decompression in pipelines. *WIT Transactions on Engineering Sciences 89* (7 2015), 45–56. Proceedings of 8th International Conference on Computational and Experimental Methods in Multiphase and Complex Flow.

[13] Cecchinato, Luca, and Corradi, Marco. Transcritical carbon dioxide small commercial cooling applications analysis. *International Journal of Refrigeration 34*, 1 (2011), 50 – 62.

[14] Champagne, Victor, Kaplowitz, Dan, Champagne III, Victor Kenneth, Howe, Chris, West, Michael K., McNally, Baillie, and Rokni, Michael. Dissimilar metal joining and structural repair of ZE41A-T5 cast magnesium by the cold spray (cs) process. *Materials & Manufacturing Processes 33*, 2 (2018), 130 – 139.

[15] Champagne, V.K. *The cold spray materials deposition process: Fundamentals and applications*. Woodhead Publishing Limited, Abington Hall, Abington, 2007.

[16] Champagne, V.K., Helfritch, D.J., Dinavahi, S.P.G., and Leyman, P.F. Theoretical and experimental particle velocity in cold spray. *Journal of Thermal Spray Technology 20*, 3, 425 – 431,.

[17] Chen, Qiyong, Alizadeh, Arash, Xie, Wanting, Wang, Xuemei, Champagne, Victor, Gouldstone, Andrew, Lee, Jae-Hwang, and Müftü, Sinan. High-strain-rate material behavior and adiabatic material instability in impact of micron-scale Al-6061 particles. *Journal of Thermal Spray Technology 27*, 4 (Apr 2018), 641–653.

[18] Clift, Roland, Grace, John R., Weber, Martin E., and Weber, Martin F. *Bubbles, drops, and particles*. Academic Press, 1978.

[19] Cormier, Yannick, Dupuis, Philippe, Jodoin, Bertrand, and Corbeil, Antoine. Pyramidal fin arrays performance using streamwise anisotropic materials by cold spray additive manufacturing. *Journal of Thermal Spray Technology 25*, 1 (Jan 2016), 170–182.

[20] Dahneke, B.E., and Cheng, Y.S. Properties of continuum source particle beams. I. calculation methods and results. *Journal of Aerosol Science 10*, 3 (1979), 257 – 274.

[21] Deng, Rensheng, Zhang, Xuefeng, Smith, Kenneth A., Wormhoudt, Joda, Lewis, David K., and Freedman, Andrew. Focusing particles with diameters of 1 to 10 microns into beams at atmospheric pressure. *Aerosol Science and Technology 42*, 11 (2008), 899–915.

[22] Dupuis, Philippe. *Flow Structure Characterization and Performance Evaluation of Pin Fins Produced Using Cold Spray.* PhD thesis, University of Ottawa, Ottawa, Ontario, Canada, 11 2016.

[23] Dykhuizen, R. C., and Smith, M. F. Gas dynamic principles of cold spray. *Journal of Thermal Spray Technology 7*, 2 (1998), 205–212.

[24] ES3, Inc. Cold spray dimensional restoration via robotic and handheld cold spray systems. `https://www.es3inc.com/cold-spray/`. accessed 4/22/2020.

[25] Faizan-Ur-Rab, M., Zahiri, S.H., Masood, S.H., Phan, T.D., Jahedi, M., and Nagarajah, R. Application of a holistic 3D model to estimate state of cold spray titanium particles. *Materials & Design 89* (2016), 1227 – 1241.

[26] Fluent, ANSYS. Fluent theory guide. 17.2.

[27] Foelsche, Robert Oliver. *Ignition and Combustion of Boron Particles in Hydrogen/oxygen Combustion Products at 30 to 150 Atmospheres.* PhD thesis, University of Illinois at Urbana-Champaign, 1998.

[28] Fukanuma, Hirotaka. Cold spray gun, 11 2011. Appl. No.: 13/270,450; Pub. No.: US 2013/0087633 A1.

[29] Fukumoto, M., Wada, H., Tanabe, K., Yamada, M., Yamaguchi, E., Niwa, A., Sugimoto, M., and Izawa, M. Effect of substrate temperature on deposition behavior of copper particles on substrate surfaces in the cold spray process. *Journal of Thermal Spray Technology 16*, 5 (2007), 643–650.

[30] Girshick, Steven L. Aerosol processing for nanomanufacturing. *Journal of Nanoparticle Research 10*, 6 (Aug 2008), 935–945.

[31] Gärtner, Frank, Heinrich, Peter, Kreye, Heinrich, Richter, Peter, and Schmidt, Tobias. Device for cold gas spraying, 22 2010. Pub. No.: US 2010/0181391 A1.

[32] Grujicic, M, Zhao, C.L, Tong, C, DeRosset, W.S, and Helfritch, D. Analysis of the impact velocity of powder particles in the cold-gas dynamic-spray process. *Materials Science and Engineering: A 368*, 1 (2004), 222 – 230.

[33] Grujicic, M, Zhao, C.L, Tong, C, DeRosset, W.S, and Helfritch, D. Analysis of the impact velocity of powder particles in the cold-gas dynamic-spray process. *Materials Science and Engineering: A 368*, 1 (2004), 222 – 230.

[34] H. Fukanuma, R. Huang. Simulation of cold spray nozzle accompanying a water-cooling adjustment. Plasma Giken Co., Saitama, Japan.

[35] Han, T., Gillispie, B. A., and Zhao, Z. B. An investigation on powder injection in the high-pressure cold spray process. *Journal of Thermal Spray Technology 18*, 3 (Sep 2009), 320–330.

[36] Hardalupas, Y., Taylor, A. M. K. P., Whitelaw, James Hunter, and Weinberg, Felix Jiri. Velocity and particle-flux characteristics of turbulent particle-laden jets. *Proceedings of the Royal Society of London. A. Mathematical and Physical Sciences 426*, 1870 (1989), 31–78.

[37] Hassani-Gangaraj, Mostafa, Veysset, David, Champagne, Victor K., Nelson, Keith A., and Schuh, Christopher A. Adiabatic shear instability is not necessary for adhesion in cold spray. *Acta Materialia 158* (2018), 430 – 439.

[38] Hoey, Justin M., Lutfurakhmanov, Artur, Schulz, Douglas L., and Akhatov, Iskander S. A review on aerosol-based direct-write and its applications for microelectronics. *Journal of Nanotechnology 2012* (Sep 2012), 324–380.

[39] Huang, R., and Fukanuma, H. Study of the influence of particle velocity on adhesive strength of cold spray deposits. *Journal of Thermal Spray Technology 21*, 3 (Jun 2012), 541–549.

[40] Hussain, Tanvir. *A study of bonding mechanisms and corrosion behaviour of cold sprayed coatings*. PhD thesis, University of Nottingham, July 2011.

[41] Innovations, Impact. Advanced high pressure cold spray equipment, coatings and selected applications. `https://www.asminternational.org/documents/10192/26746001/6+-+Richter.pdf/f9e17670-8adc-4579-8acd-decef9236cbc`, 11 2016. presented at North American Cold Spray Conference; Edmonton, Alberta, Canada.

[42] J. Fernandez de la Mora, J. Rosell-Llompart, P. Riesco-Chueca. Aerodynamic focusing of particles and molecules in seeded supersonic jets. *Rarefied Gas Dynamics: Physical Phenomena* (1989), 247–277. American Institute of Aeronautics and Astronautics.

[43] Jen, Tien-Chien, Li, Longjian, Cui, Wenzhi, Chen, Qinghua, and Zhang, Xinming. Numerical investigations on cold gas dynamic spray process with nano- and microsize particles. *International Journal of Heat and Mass Transfer 48*, 21 (2005), 4384 – 4396.

[44] Karimi, M., Fartaj, A., Rankin, G., Vanderzwet, D., Birtch, W., and Villafuerte, J. Numerical simulation of the cold gas dynamic spray process. *Journal of Thermal Spray Technology 15*, 4 (Dec 2006), 518–523.

[45] Khalkhali, Zahra. *Cold Spray Deposition of Polymers – Characterization and Optimization*. PhD thesis, University of Massachusetts Amherst, 9 2019.

[46] Khalkhali, Zahra, Xie, Wanting, Champagne, Victor K., Lee, Jae-Hwang, and Rothstein, Jonathan P. A comparison of cold spray technique to single particle micro-ballistic impacts for the deposition of polymer particles on polymer substrates. *Surface and Coatings Technology 351* (2018), 99 – 107.

[47] Kim, G.E., Champagne, V.K., Trexler, M., and Sohn, Y. 20 - Processing nanostructured metal and metal-matrix coatings by thermal and cold spraying. In *Nanostructured Metals and Alloys*, Sung H. Whang, Ed., Woodhead Publishing Series in Metals and Surface Engineering. Woodhead Publishing, 2011, pp. 615 – 662.

[48] Kleis, I, and Hussainova, I. Investigation of particle-wall impact process. *Wear 233-235* (1999), 168 – 173.

[49] Klinkov, S.V., Kosarev, V.F., Sova, A.A., and Smurov, I. Deposition of multicomponent coatings by cold spray. *Surface and Coatings Technology 202*, 24 (2008), 5858 – 5862.

[50] Koivuluoto, Heli, Coleman, Andrew, Murray, Keith, Kearns, Martin, and Vuoristo, Petri. High pressure cold sprayed (HPCS) and low pressure cold sprayed (LPCS) coatings prepared from OFHC Cu feedstock: Overview from powder characteristics to coating properties. *Journal of Thermal Spray Technology 21*, 5 (Sep 2012), 1065–1075.

[51] Koivuluoto, Heli, and Vuoristo, Petri. Effect of ceramic particles on properties of cold-sprayed Ni-20Cr+Al2O3 coatings. *Journal of Thermal Spray Technology 18*, 4 (Jun 2009), 555.

[52] Kosarev, V. F., Klinkov, S. V., Alkhimov, A. P., and Papyrin, A. N. On some aspects of gas dynamics of the cold spray process. *Journal of Thermal Spray Technology 12*, 2 (2003), 265–281.

[53] Kreith, Frank, and Manglik, Raj M. *Principles of Heat Transfer*, 8th ed. Cengage Learning, Boston, MA, 2016.

[54] Kulkarni, Vinayak, Sahoo, Niranjan, and Chavan, Sandip D. Simulation of honeycomb–screen combinations for turbulence management in a subsonic wind tunnel. *Journal of Wind Engineering and Industrial Aerodynamics 99*, 1 (2011), 37 – 45.

[55] Lee, J.C., Kang, H.J., Chu, W.S., and Ahn, S.H. Repair of damaged mold surface by cold-spray method. *CIRP Annals 56*, 1 (2007), 577 – 580.

[56] Lee, Jin-Won, Yi, Min-Young, and Lee, Sang-Min. Inertial focusing of particles with an aerodynamic lens in the atmospheric pressure range. *Journal of Aerosol Science 34*, 2 (2003), 211 – 224.

[57] Lehtonen, Joonas, Koivuluoto, Heli, Ge, Yanling, Juselius, Aapo, and Hannula, Simo-Pekka. Cold gas spraying of a high-entropy CrFeNiMn equiatomic alloy. *Coatings 10*, 1 (1 2020), 53.

[58] Li, Shuo, Muddle, Barry, Jahedi, Mahnaz, and Soria, Julio, Eds. *Numerical investigation of the cold spray process* (Melbourne, Australia, 12 2009), Seventh International Conference on CFD in the Minerals and Process Industries, CSIRO.

[59] Li, Wen-Ya, and Li, Chang-Jiu. Optimal design of a novel cold spray gun nozzle at a limited space. *Journal of Thermal Spray Technology 14*, 3 (Sep 2005), 391–396.

[60] Li, Wen-Ya, Li, Chang-Jiu, Wang, Hong-Tao, Li, Cheng-Xin, and Bang, Hee-Seon. Measurement and numerical simulation of particle velocity in cold spraying. *Journal of Thermal Spray Technology 15*, 4 (Dec 2006), 559–562.

[61] Li, Wen-Ya, Liao, Hanlin, Douchy, G., and Coddet, C. Optimal design of a cold spray nozzle by numerical analysis of particle velocity and experimental validation with 316L stainless steel powder. *Materials & Design 28*, 7 (2007), 2129 – 2137.

[62] Li, Wen-Ya, Liao, Hanlin, Wang, Hong-Tao, Li, Chang-Jiu, Zhang, Ga, and Coddet, C. Optimal design of a convergent-barrel cold spray nozzle by numerical method. *Applied Surface Science 253*, 2 (2006), 708 – 713.

[63] Li, Wen-Ya, Yin, Shuo, Guo, Xueping, Liao, Hanlin, Wang, Xiao-Fang, and Coddet, Christian. An investigation on temperature distribution within the substrate and nozzle wall in cold spraying by numerical and experimental methods. *Journal of Thermal Spray Technology 21*, 1 (Jan 2012), 41–48.

[64] Li, Wenya, and Li, Chang-Jiu. Optimization of spray conditions in cold spraying based on numerical analysis of particle velocity. *Transactions of Nonferrous Metals Society of China (English Edition) 14* (10 2004), 43–48.

[65] Liao, Yixiang, and Lucas, Dirk. Evaluation of interfacial heat transfer models for flashing flow with two-fluid CFD. *Fluids 3*, 2 (June 2018).

[66] Liebersbach, Piotr, Foelsche, Alden, Champagne, Victor K., Siopis, Matt, Nardi, Aaron, and Schmidt, David P. CFD simulations of feeder tube pressure oscillations and prediction of clogging in cold spray nozzles. *Journal of Thermal Spray Technology 29*, 3 (Feb 2020), 400–412.

[67] Lima, R.S., Agarwal, A., Hyland, M.M., Lau, Y.-C., Li, C.-J., McDonald, A., and Toma, F.-L., Eds. *Cold Spray Forming Inconel 718* (Houston, Texas, USA, 5 2012), Industrial Materials Institute, National Research Council Canada, Boucherville, Quebec, Canada; Department of Mining and Materials Engineering, McGill University, Montreal, Quebec, Canada; Plasma Giken Co., LTD., Tokyo, Japan, ASM International. Proceedings from the International Thermal Spray Conference and Exposition.

[68] Liu, Peng, Ziemann, Paul J., Kittelson, David B., and McMurry, Peter H. Generating particle beams of controlled dimensions and divergence: I. theory of particle motion in aerodynamic lenses and nozzle expansions. *Aerosol Science and Technology 22*, 3 (1995), 293–313.

[69] Liu, Peng, Ziemann, Paul J., Kittelson, David B., and McMurry, Peter H. Generating particle beams of controlled dimensions and divergence: II. experimental evaluation of particle motion in aerodynamic lenses and nozzle expansions. *Aerosol Science and Technology 22*, 3 (1995), 314–324.

[70] Luo, Xiao-Tao, Li, Yu-Juan, Li, Cheng-Xin, Yang, Guan-Jun, and Li, Chang-Jiu. Effect of spray conditions on deposition behavior and microstructure of cold sprayed Ni coatings sprayed with a porous electrolytic ni powder. *Surface and Coatings Technology 289* (2016), 85 – 93.

[71] Lupoi, R. Current design and performance of cold spray nozzles: experimental and numerical observations on deposition efficiency and particle velocity. *Surface Engineering 30*, 5 (2014), 316 – 322.

[72] Lupoi, R., and O'Neill, W. Powder stream characteristics in cold spray nozzles. *Surface and Coatings Technology 206*, 6 (2011), 1069 – 1076.

[73] Ma, Yitai, Liu, Zhongyan, and Tian, Hua. A review of transcritical carbon dioxide heat pump and refrigeration cycles. *Energy 55* (2013), 156 – 172.

[74] MacDonald, D., Leblanc-Robert, S., Fernández, R., Farjam, A., and Jodoin, B. Effect of nozzle material on downstream lateral injection cold spray performance. *Journal of Thermal Spray Technology 25*, 6 (2016), 1149–1157.

[75] MatWeb. Matweb material property data AK steel 17-4 PH precipitation hardening stainless steel, condition H 900k. `http://www.matweb.com/search/DataSheet.aspx?MatGUID=ef0844b850954281a438dc76c1e0b49e`. accessed 4/22/2020.

[76] Mauer, G., Singh, R., Rauwald, K.-H., Schrüfer, S., Wilson, S., and Vaßen, R. Diagnostics of cold-sprayed particle velocities approaching critical deposition conditions. *Journal of Thermal Spray Technology 26*, 7 (Oct 2017), 1423–1433.

[77] Meyer, M., Caruso, F., and Lupoi, R. Particle velocity and dispersion of high stokes number particles by PTV measurements inside a transparent supersonic cold spray nozzle. *International Journal of Multiphase Flow 106* (2018), 296 – 310.

[78] Meyer, M., and Lupoi, R. An analysis of the particulate flow in cold spray nozzles. *Mechanical Sciences 6*, 2 (2015), 127–136.

[79] Meyer, M., Yin, S., and Lupoi, R. Particle in-flight velocity and dispersion measurements at increasing particle feed rates in cold spray. *Journal of Thermal Spray Technology 26*, 1 (Jan 2017), 60–70.

[80] Moridi, A., Hassani-Gangaraj, S.M., and Guagliano, M. A hybrid approach to determine critical and erosion velocities in the cold spray process. *Applied Surface Science 273* (2013), 617 – 624.

[81] Morère, J., Schmidt, D.P., Liebersbach, P., and Watkins, J.J. Suppression of clogging in cold spray nozzles. Presented at CSAT Conference; University of Massachusetts Amherst, 6 2018. removed from online - available upon request.

[82] Nardi, A., Wang, X., Sharon, J., Mordasky, M., and Espinal, A. Cold spray materials and process development at UTRC. `https://55922c16-bbf4-4650-aa4d-6d5bfb8c7a14.filesusr.com/ugd/0ebd9c_7be65901f9a24e83adc78db59270f9b7.pdf`, 6 2015. United Technologies Research Center, Presented at CSAT meeting.

[83] Nastic, A., and Jodoin, B. Evaluation of heat transfer transport coefficient for cold spray through computational fluid dynamics and particle in-flight temperature measurement using a high-speed IR camera. *Journal of Thermal Spray Technology 27*, 8 (Dec 2018), 1491–1517.

[84] Nguyen, A.V., and Fletcher, C.A.J. Particle interaction with the wall surface in two-phase gas-solid particle flow. *International Journal of Multiphase Flow 25*, 1 (1999), 139 – 154.

[85] Ning, Xian-Jin, Wang, Quan-Sheng, Ma, Zhuang, and Kim, Hyung-Jun. Numerical study of in-flight particle parameters in low-pressure cold spray process. *Journal of Thermal Spray Technology 19*, 6 (Dec 2010), 1211–1217.

[86] Ozdemir, Ozan C., and Widener, Christian A. Gas dynamics of cold spray & control of deposition. South Dakota School of Mines & Technology, 01/31/2017.

[87] Ozdemir, Ozan C., and Widener, Christian A. Influence of powder injection parameters in high-pressure cold spray. *Journal of Thermal Spray Technology 26*, 7 (Oct 2017), 1411–1422.

[88] Ozdemir, Ozan C., Widener, Christian A., Helfritch, Dennis, and Delfanian, Fereidoon. Estimating the effect of helium and nitrogen mixing on deposition efficiency in cold spray. *Journal of Thermal Spray Technology 25*, 4 (Apr 2016), 660–671.

[89] Papyrin, Anatolii, Kosarev, Vladimir, Klinkov, Sergey, Alkhimov, Anatolii, and Fomin, Vasily M. *Cold Spray Technology*. Elsevier Ltd, 10 2006.

[90] Park, Jung-Jae, Lee, Min-Wook, Yoon, Sam S., Kim, Ho-Young, James, Scott C., Heister, Stephen D., Chandra, Sanjeev, Yoon, Woon-Ha, Park, Dong-Soo, and Ryu, Jungho. Supersonic nozzle flow simulations for particle coating applications: Effects of shockwaves, nozzle geometry, ambient pressure, and substrate location upon flow characteristics. *Journal of Thermal Spray Technology 20*, 3 (Mar 2011), 514–522.

[91] Petersen, Helge. The properties of helium: Density, specific heats, viscosity, and thermal conductivity at pressures from 1 to 100 bar and from room temperature to about 1800 K. *Danish Atomic Energy Commission, Research Establishment Riso*, 224 (8 1970).

[92] Plasma Giken Co., Ltd. The next generation in cold spray technology; introducing cold spray PCS-1000 and PCS-800. `http://www.plasma.co.jp/en/products/pcs1000.pdf`. online brochure, accessed 4/20/2020.

[93] Plasma Giken Co., Ltd. Plasma cold spray equipment. `http://www.plasma.co.jp/en/products/coldspray.html`. accessed 4/20/2020.

[94] Poirier, Dominique, Legoux, Jean-Gabriel, Vo, Phuong, Blais, Bruno, Giallonardo, Jason D., and Keech, Peter G. Powder development and qualification for high-performance cold spray copper coatings on steel substrates. *Journal of Thermal Spray Technology 28*, 3 (Feb 2019), 444–459.

[95] POLYCONTROLS. Ultrafine powder feeding in thermal/cold spray application. `https://www.polycontrols.com/wp-content/uploads/2017/09/Polycontrols-Powerfeeder.pdf`, 11 2016. Alberta Innovates – Technology Futures, North American Cold Spray Conference, Edmonton, Alberta, Canada.

[96] Qi, Lejun, McMurry, Peter H., Norris, David J., and Girshick, Steven L. Micropattern deposition of colloidal semiconductor nanocrystals by aerodynamic focusing. *Aerosol Science and Technology 44*, 1 (2010), 55–60.

[97] Ranz, W.E., and W.R. Marshall, Jr. Evaporation from drops, part I. *Chemical Engineering Progress 48*, 3 (3 1952), 141–146.

[98] Ranz, W.E., and W.R. Marshall, Jr. Evaporation from drops, part II. *Chemical Engineering Progress 48*, 4 (4 1952), 173–180.

[99] Raoelison, R.N., Xie, Y., Sapanathan, T., Planche, M.P., Kromer, R., Costil, S., and Langlade, C. Cold gas dynamic spray technology: A comprehensive review of processing conditions for various technological developments till to date. *Additive Manufacturing 19* (2018), 134 – 159.

[100] Sabard, Alexandre, McNutt, Philip, Begg, Henry, and Hussain, Tanvir. Cold spray deposition of solution heat treated, artificially aged and naturally aged Al 7075 powder. *Surface and Coatings Technology 385* (2020), 125367.

[101] Sakaki, K., and Shimizu, Y. Effect of the increase in the entrance convergent section length of the gun nozzle on the high-velocity oxygen fuel and cold spray process. *Journal of Thermal Spray Technology 10*, 3 (Sep 2001), 487–496.

[102] Samareh, B., and Dolatabadi, A. A three-dimensional analysis of the cold spray process: The effects of substrate location and shape. *Journal of Thermal Spray Technology 16*, 5 (Dec 2007), 634–642.

[103] Samareh, B., Stier, O., Lüthen, V., and Dolatabadi, A. Assessment of CFD modeling via flow visualization in cold spray process. *Journal of Thermal Spray Technology 18*, 5 (Aug 2009), 934.

[104] Schmidt, T., Gärtner, F., Assadi, H., and Kreye, H. Development of a generalized parameter window for cold spray deposition. *Acta Materialia 54*, 729 – 742,.

[105] Schmidt, T., Gärtner, F., and Kreye, H. New developments in cold spray based on higher gas and particle temperatures. *Journal of Thermal Spray Technology 15*, 4 (2006), 488–494.

[106] Schmidt, Tobias, Assadi, Hamid, Gärtner, Frank, Richter, Horst, Stoltenhoff, Thorsten, Kreye, Heinrich, and Klassen, Thomas. From particle acceleration to impact and bonding in cold spraying. *Journal of Thermal Spray Technology 18*, 5 (2009), 794.

[107] Singh, Harminder, Sidhu, T. S., Kalsi, S. B. S., and Karthikeyan, J. Development of cold spray from innovation to emerging future coating technology. *Journal of the Brazilian Society of Mechanical Sciences and Engineering 35*, 3 (Oct 2013), 231–245.

[108] Singh, R., Rauwald, K.-H., Wessel, E., Mauer, G., Schruefer, S., Barth, A., Wilson, S., and Vassen, R. Effects of substrate roughness and spray-angle on deposition behavior of cold-sprayed inconel 718. *Surface and Coatings Technology 319* (2017), 249 – 259.

[109] Siopis, M., Nardi, A., Espinal, A., Binek, L., and Landry, T. Study of nozzle clogging during cold spray. `https://w.mawebcenters.com/static/website/165/165729/files/Siopis_Study%20of%20Nozzle%20Clogging%20During%20Cold%20Spray.pdf`. [United Technologies Research Center, accessed 4/15/2020].

[110] Sivells, James C. Aerodynamic design of axisymmetric hypersonic wind-tunnel nozzles. *Journal of Spacecraft and Rockets 7*, 11 (1970), 1292–1299.

[111] Sommerfeld, M, and Huber, N. Experimental analysis and modelling of particle-wall collisions. *International Journal of Multiphase Flow 25*, 6 (1999), 1457 – 1489.

[112] Sova, A., Grigoriev, S., Kochetkova, A., and Smurov, I. Influence of powder injection point position on efficiency of powder preheating in cold spray: Numerical study. *Surface and Coatings Technology 242* (2014), 226 – 231.

[113] Sova, A., Grigoriev, S., Okunkova, A., and Smurov, I. Cold spray deposition of 316L stainless steel coatings on aluminium surface with following laser post-treatment. *Surface and Coatings Technology 235* (2013), 283 – 289.

[114] Sova, Aleksey, Okunkova, Anna, Grigoriev, Sergei, and Smurov, Igor. Velocity of the particles accelerated by a cold spray micronozzle: Experimental measurements and numerical simulation. *Journal of Thermal Spray Technology 22*, 1 (Feb 2013), 75–80.

[115] Stoltenhoff, T., Kreye, H., and Richter, H. J. An analysis of the cold spray process and its coatings. *Journal of Thermal Spray Technology 11*, 4 (2002), 542–550.

[116] Suhonen, T., Varis, T., Dosta, S., Torrell, M., and Guilemany, J.M. Residual stress development in cold sprayed Al, Cu and Ti coatings. *Acta Materialia 61*, 17 (2013), 6329 – 6337.

[117] Sutherland, William. LII. the viscosity of gases and molecular force. *The London, Edinburgh, and Dublin Philosophical Magazine and Journal of Science 36*, 223 (1893), 507–531.

[118] Tabbara, H., Gu, S., McCartney, D. G., Price, T. S., and Shipway, P. H. Study on process optimization of cold gas spraying. *Journal of Thermal Spray Technology 20*, 3 (Mar 2011), 608–620.

[119] Tang, Wenyong, Liu, Juanfang, Chen, Qinghua, Zhang, Xueqing, and Chen, Ziyun. The effects of two gas flow streams with initial temperature and pressure differences in cold spraying nozzle. *Surface and Coatings Technology 240* (2014), 86 – 95.

[120] Taylor, K., Jodoin, B., and Karov, J. Particle loading effect in cold spray. *Journal of Thermal Spray Technology 15*, 2 (2006), 273–279.

[121] Tucker, Maurice. Approximate turbulent boundary-layer development in plane compressible flow along thermally insulated surfaces with application to supersonic-tunnel contour correction. Tech. rep., National Advisory Committee for Aeronautics, Lewis Flight Propulsion Laboratory Cleveland, Ohio, 3 1950. NACA Technical Note 2045.

[122] Vargaftik, and Yakush. Temperature dependence of thermal conductivity of helium. *Journal of Engineering Physics and Thermophysics 32*, 5, 530–532.

[123] Venkatesh, L., Chavan, Naveen M., and Sundararajan, G. The influence of powder particle velocity and microstructure on the properties of cold sprayed copper coatings. *Journal of Thermal Spray Technology 20*, 5 (2011), 1009–1021.

[124] Victor K. Champagne, Dr. Dennis Helfritch, and Leyman, Phillip F., Eds. *Magnesium Repair by Cold Spray* (Aberdeen Proving Ground, MD, 2007), NASF-SUR/FIN Proceedings. U.S. Army Research Laboratory.

[125] Vo, Phuong, Poirier, Dominique, Legoux, Jean-Gabriel, Keech, Peter G., Doyle, David, Jakupi, Pellumb, and Irissou, Eric. Development of cold spray technology for copper coating of carbon steel used fuel container prototypes for CANDU fuel. Tech. rep., Nuclear Waste Management Organization (NWMO), Toronto, Canada, 11 2015.

[126] Vreman, Bert, Geurts, Bernard J., Deen, N. G., Kuipers, J. A. M., and Kuerten, J. G. M. Two- and four-way coupled euler-lagrangian large-eddy simulation of turbulent particle-laden channel flow. *Flow, Turbulence and Combustion 82*, 1 (2009), 47–71.

[127] Wang, Hong-Ren, Hou, Bao-Rong, Wang, Jun, Wang, Qi, and Li, Wen-Ya. Effect of process conditions on microstructure and corrosion resistance of cold-sprayed Ti coatings. *Journal of Thermal Spray Technology 17*, 5 (2008), 736–741.

[128] Wang, Jintang, Wang, Zhiyuan, and Sun, Baojiang. Improved equation of CO_2 joule-thomson coefficient. *Journal of CO2 Utilization 19* (2017), 296 – 307.

[129] Wang, Xiao-Fang, Yin, Shuo, and Xu, Bao-Peng. Effect of cold spray particle conditions and optimal standoff distance on impact velocity. *Journal of Dalian University of Technology 54*, 4 (7 2011), 498–504.

[130] Wang, Xiaoliang, and McMurry, Peter H. A design tool for aerodynamic lens systems. *Aerosol Science and Technology 40*, 5 (2006), 320–334.

[131] Wang, Xiaoliang, and McMurry, Peter H. Instruction manual for the aerodynamic lens calculator. *Aerosol Science and Technology 40*, 5 (2006), 1–10.

[132] Wang, Xudong, Zhang, Bo, Lv, Jinsheng, and Yin, Shuo. Investigation on the clogging behavior and additional wall cooling for the axial-injection cold spray nozzle. *Journal of Thermal Spray Technology 24*, 4 (2015), 696–701.

[133] Wang, Xuemei, Feng, Feng, Klecka, Michael A., Mordasky, Matthew D., Garofano, Jacquelynn K., El-Wardany, Tahany, Nardi, Aaron, and Champagne, Victor K. Characterization and modeling of the bonding process in cold spray additive manufacturing. *Additive Manufacturing 8* (2015), 149 – 162.

[134] Watanabe, Yuta, Yoshida, Chisato, Atsumi, Keisuke, Yamada, Motohiro, and Fukumoto, Masahiro. Influence of substrate temperature on adhesion strength of cold-sprayed coatings. *Journal of Thermal Spray Technology 24*, 1 (2015), 86–91.

[135] White, Frank M. *Viscous Fluid Flow*, 3 ed. McGraw Hill Education (India), 2006.

[136] Widener, Christian A., Ozdemir, Ozan C., and Carter, Michael. Structural repair using cold spray technology for enhanced sustainability of high value assets. *Procedia Manufacturing 21* (2018), 361 – 368. 15th Global Conference on Sustainable Manufacturing.

[137] Wilcox, David C. *Basic Fluid Mechanics*, 2 ed. DCW Industries, 8 2000. Chapter 4.

[138] Wong, W., Irissou, E., Vo, P., Sone, M., Bernier, F., Legoux, J.-G., Fukanuma, H., and Yue, S. Cold spray forming of inconel 718. *Journal of Thermal Spray Technology 22*, 2 (Mar 2013), 413–421.

[139] Wong, W., Vo, P., Irissou, E., Ryabinin, A. N., Legoux, J.-G., and Yue, S. Effect of particle morphology and size distribution on cold-sprayed pure titanium coatings. *Journal of Thermal Spray Technology 22*, 7 (Oct 2013), 1140–1153.

[140] Wong, Wilson, Irissou, Eric, Ryabinin, Anatoly N., Legoux, Jean-Gabriel, and Yue, Stephen. Influence of helium and nitrogen gases on the properties of cold gas dynamic sprayed pure titanium coatings. *Journal of Thermal Spray Technology 20*, 1 (Jan 2011), 213–226.

[141] Xie, Wanting, Alizadeh-Dehkharghani, Arash, Chen, Qiyong, Champagne, Victor K., Wang, Xuemei, Nardi, Aaron T., Kooi, Steven, Müftü, Sinan, and Lee, Jae-Hwang. Dynamics and extreme plasticity of metallic microparticles in supersonic collisions. *Scientific Reports 7*, 1 (Jul 2017), 5073.

[142] Xue, L. Chapter 16 - laser consolidation - a rapid manufacturing process for making net-shape functional components. In *Advances in Laser Materials Processing (Second Edition)*, Jonathan Lawrence, Ed., second edition ed., Woodhead Publishing Series in Welding and Other Joining Technologies. Woodhead Publishing, 2018, pp. 461 – 505.

[143] Yildirim, Baran, Yang, Hankang, Gouldstone, Andrew, and Müftü, Sinan. Rebound mechanics of micrometre-scale, spherical particles in high-velocity impacts. *Proceedings A, Royal Society 473*, 20160936 (August 2017).

[144] Yin, S., Suo, X., Liao, H., Guo, Z., and Wang, X. Significant influence of carrier gas temperature during the cold spray process. *Surface Engineering 30*, 6 (2014), 443–450.

[145] Yin, Shuo, Cavaliere, Pasquale, Aldwell, Barry, Jenkins, Richard, Liao, Hanlin, Li, Wenya, and Lupoi, Rocco. Cold spray additive manufacturing and repair: Fundamentals and applications. *Additive Manufacturing 21* (2018), 628 – 650.

[146] Yin, Shuo, Liu, Qi, Liao, Hanlin, and Wang, Xiaofang. Effect of injection pressure on particle acceleration, dispersion and deposition in cold spray. *Computational Materials Science 90* (2014), 7 – 15.

[147] Yin, Shuo, Meyer, Morten, Li, Wenya, Liao, Hanlin, and Lupoi, Rocco. Gas flow, particle acceleration, and heat transfer in cold spray: A review. *Journal of Thermal Spray Technology 25*, 5 (Jun 2016), 874–896.

[148] Yin, Shuo, Suo, Xinkun, Xie, Yingchun, Li, Wenya, Lupoi, Rocco, and Liao, Hanlin. Effect of substrate temperature on interfacial bonding for cold spray of Ni onto Cu. *Journal of Materials Science 50*, 22 (2015), 7448–7457.

[149] Yin, Shuo, Zhang, Meng, Guo, Zhiwei, Liao, Hanlin, and Wang, Xiaofang. Numerical investigations on the effect of total pressure and nozzle divergent length on the flow character and particle impact velocity in cold spraying. *Surface and Coatings Technology 232* (2013), 290 – 297.

[150] Yu, Min, and Li, Wenya. *Metal Matrix Composite Coatings by Cold Spray*. Springer International Publishing, Cham, 2018, pp. 297–318.

[151] Zahiri, S. H., Phan, T. D., Masood, S. H., and Jahedi, M. Development of holistic three-dimensional models for cold spray supersonic jet. *Journal of Thermal Spray Technology 23*, 6 (Aug 2014), 919–933.

[152] Zhalehrajabi, Ehsan, Rahmanian, Nejat, and Hasan, Nurul. Effects of mesh grid and turbulence models on heat transfer coefficient in a convergent-divergent nozzle. *Asia-Pacific Journal of Chemical Engineering 9* (2013), 265 – 271.

[153] Zhang, Xuefeng, Smith, Kenneth A., Worsnop, Douglas R., Jimenez, Jose, Jayne, John T., and Kolb, Charles E. A numerical characterization of particle beam collimation by an aerodynamic lens-nozzle system: Part I. an individual lens or nozzle. *Aerosol Science and Technology 36*, 5 (2002), 617–631.

[154] Zhang, Xuefeng, Smith, Kenneth A., Worsnop, Douglas R., Jimenez, Jose L., Jayne, John T., Kolb, Charles E., Morris, James, and Davidovits, Paul. Numerical characterization of particle beam collimation: Part II integrated aerodynamic-lens–nozzle system. *Aerosol Science and Technology 38*, 6 (2004), 619–638.

[155] Zhou, Xianglin, Wu, Xiangkun, Wang, Jianguo, and Zhang, Jishan. Numerical investigation of the rebounding and the deposition behavior of particles during cold spraying. *Acta Metallurgica Sinica (English Letters) 24*, 1 (2011), 43–53.